Fabrication and mechanical properties of carbon fiber reinforced aluminum matrix composites by squeeze casting

Zhiqiang Tu

Thesis submitted to the University of Ottawa
in partial Fulfillment of the requirements for the

MASTER OF APPLIED SCIENCE

in Advanced Materials and Manufacturing
Faculty of engineering
University of Ottawa

ABSTRACT

Rapid modern technological changes and improvements bring great motivations in advanced material designs and fabrications. In this context, metal matrix composites, as an emerging material category, have undergone great developments over the past 50 years. Their primary applications, such as automotive, aerospace and military industries, require materials with increasingly strict specifications, especially high stiffness, lightweight and superior strength. For these advanced applications, carbon fiber reinforced aluminum matrix composites have proven their enormous potential where outstanding machinability, engineering reliability and economy efficiency are vital priorities.

To contribute in the understanding and development of carbon fiber reinforced aluminum matrix composites, this study focuses on composite fabrication, mechanical testing and physical property modelling. The composites are fabricated by squeeze casting. Plain weave carbon fiber (AS4 Hexcel) is used as reinforcement, while aluminum alloy 6061 is used as matrix. The improvement of the squeeze casting fabrication process is focused on reducing leakage while combining thermal expansion pressure with post-processing pressing. Three different fiber volume fractions are investigated to achieve optimum mechanical properties. Piston-on-ring (POR) bend tests are used to measure the biaxial flexural stiffness and fracture strength on disc samples. The stress-strain curves and fracture surfaces reveal the effect of fiber-matrix interface bonding on composite bend behaviour. The composites achieved up to 11.6%, 248.3% and 90.1% increase in flexural modulus, strain hardening modulus and yield strength as compared with the unreinforced aluminum alloy control group, respectively. Analytical modelling and finite element modelling are used to comparatively characterise and verify the composite effective flexural modulus and strength. Specifically, they allowed evaluating how far the experimental results deviate from idealized assumptions of the models, which provides an insight into the composite sample quality, particularly at fiber-matrix interfaces. Overall, the models agree well with experimental results in identifying an improvement in flexural modulus up to a carbon fiber volume fraction of 4.81vol%. However, beyond a fiber content of 3.74vol%, there is risk of deterioration of mechanical properties, particularly the strength. This is because higher carbon fiber volume fractions restrict the infiltration and wetting of carbon fibre by the liquid, potentially leading to poor fiber-matrix interface bonding. It is shown that higher thermal expansion pressures and subsequent post-processing pressing can overcome this challenge at higher carbon fiber volume contents by reducing fiber-aluminum contact angle, improving infiltration, reducing defects such as porosity, and overall improving fiber-matrix bonding.

TABLE OF CONTENTS

LIST OF FIGURES

LIST OF TABLES

LIST OF SYMBOLS

Symbol	Definition
α	Thermal expansion
γ	Engineering shear strains
γ_{lv}	Surface tension of the liquid
ε	Strain
θ	Rotation angle
κ	Yarn packing fraction
ρ	Central axis
σ_{por}	Piston-on-ring (POR) maximum bending stress
σ_{ror}	Ring-on-ring (ROR) maximum bending stress
τ	Transverse shear stress
φ	Central angle
ω	Plate deflection
a	Effective square side length
A	Cross-sectional area
D	Bending rigidity
E	Elastic modulus
f	Correction factor
F	Load
G	Shear modulus
h	Layer location
i	Layer number
I	Moment of inertia
l	Length
M_{por}	POR bending moment
P	Testing load
P_c	Critical capillary pressure
r	Radius
S	Specific area
t	Thickness
$\mathrm{T}(\theta)$	Rotation matrix
u_{ror}	Ring-on-ring (ROR) mid-span deflection
V	Carbon fiber volume fraction
W_f	Effective square side length
y	Position of thickness
[C]	Stiffness tensor
[S]	Compliance tensor

1 BACKGROUND AND INTRODUCTION

1.1 Background

The development of novel materials as enablers of modern technologies is constantly driven by the demand for increasingly superior mechanical properties to satisfy ever increasing technology challenges and more and more complex environments. In this context, composite materials have been undergoing dramatic developments in the past several decades due to their various advantages and potentials [1]. Composite materials are fabricated using two or more different components in order to achieve superior properties [2]. Mostly, the strengthening components give material stiffness and strength, while the matrix components provide ductility and protection [2]. Under these circumstances, the composite material designs directly target application specifications such as high strength, thermal resistance and physical characteristics [3]. Meanwhile, with the development of fabrication techniques, composite materials are increasingly gaining broad application fields thanks to improved stability and cost-effectiveness [1].

Composites are often classified based on the nature of their matrix material into Polymer Matrix Composite (PMCs), Ceramic Matrix Composites (CMCs), and Metal Matrix Composites (MMCs). Each of the composite classes has unique advantages for their specific set of application industries [4]. Intrinsically, metallic materials combine ductility, toughness and strength while providing high electrical and thermal conductivity, which has made them excellent engineering materials for a large variety of industry applications. The addition of strengthening phases and reinforcements further increases the wide variety of structures, properties and performance achievable with metal-based composites. For example, MMCs have been successfully used in automotive and other transportation applications primarily due to their high strength-to-weight ratios [5]. With significant superiority in elastic modulus and creep resistance, MMCs also exhibit high competitiveness in the aerospace industry [6]. Other characteristics of metal-based composites such as wear resistance, electric resistance, thermal conductivity and corrosion resistance can be further optimised by different constituents' combinations.

Carbon fiber is a top candidate for composite reinforcement for new generations of materials and is playing a key role in the composite sector, primarily because of its excellent elastic modulus [7]. Also, continuous fiber reinforced MMCs have been successfully used for the Hubble space telescope as waveguide booms due to their lightweight and superior electrical conductivity [8]. In addition, thanks to their high young's modulus and fatigue resistance, carbon fiber reinforced metal matrix composites have been used as blade sleeves for military aircrafts [9]. Particularly aluminum alloys are gaining popularity in engineering structures due to their wide range of exceptional properties. Among others, excellent economic efficiency and workability are driving the application of carbon fiber reinforced aluminum matrix composites in various industries [10].

1.2 Introduction

MMCs have a long-standing history in manufacturing since 1700BC [5]. However, MMCs have witnessed an incredibly rapid adoption in practical industry applications in the last few decades [3][5]. With breakthroughs in material science, new manufacturing processes and advanced technologies, MMCs are achieving various specialised characteristics by different constituent combinations [10][11]. As seen in Figure 1-1, MMCs can also be categorised into either discontinues reinforcement or continues fiber reinforcement composites

[5][11]. Specific characteristics of composites such as high elastic modulus, high temperature tolerance, and low-density rely on the appropriate selection of the strengthening phase.

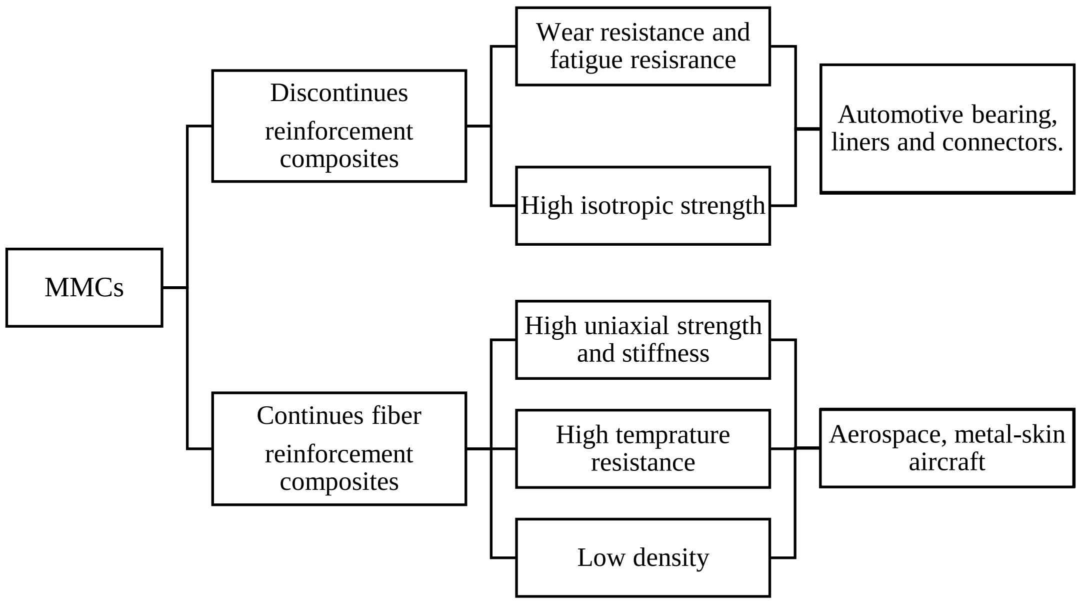

Figure 1-1: Metal matrix composite classifications and applications [5][11]

Various fabrication methods are used to successfully produce metal matrix composite materials such as squeeze casting, stir casting, hot pressing, and powder metallurgy. Among them, squeeze casting has proven to be simple and effective while providing high raw material utilization. Therefore, it is widely used to produce high quality parts [12]. As a liquid phase process, squeeze casting combines the advantages of traditional gravity casting and high-pressure die casting [10]. High infiltration pressure is indispensable for high flow resistance materials and poor interface wettability composites. Especially for MMCs, metal matrices are usually combined with carbon or ceramic reinforcements, which are characterised by contact angles mostly large than 90 degrees. Compared to low pressure casting, rapid cooling rates and low casting temperatures in squeeze casting generally result in lower porosity, reduced casting defects and better internal structures in the final products. Furthermore, squeeze casting features some benefits of forging, including great surface finish and high material strength.

Carbon fiber was initially used in the aerospace industry due to its high stiffness, fracture strength and thermal resistance. However, brittleness and weak shear strength are disadvantages of carbon fiber, which usually requires it to be protected by other materials. As candidate matrix material for carbon fiber, aluminum has low density and excellent mechanical properties. Alloying elements, such as silicon and magnesium, improve the castability and corrosion resistance of aluminum. With their typically low casting shrinkage and low macrosegregation, aluminum alloys are ideal candidate matrix materials for squeeze casting processing.

The interface is a critical design aspect of MMCs which determines the load transfer between the reinforcement and the matrix. For MMCs, the most common interface bonding mechanisms are diffusion and reaction bonding resulting from interfacial reactions. A stable and strong interface is an important prerequisite for the mechanical strength of composites. In contrast, an overly rigid and brittle interface results in poor load transfer between the fiber and the matrix and ultimately in poor mechanical properties. Moreover, weak interfacial bonding due to poor wetting of fibers by the matrix alloys is the most prominent challenge in MMCs fabrication and applications.

Plain weave AS4 Hexcel carbon fiber reinforced aluminum matrix composites were successfully fabricated by laminate squeeze casting in a previous study [12]. Good interface bonding between fiber and aluminum was achieved. The present work investigates improvements in the fabrication technique with the objective of further optimising interface bonding and final mechanical properties. For this purpose, higher casting pressures and additional post-processing pressing are studied. Furthermore, in contrast to the uniaxial bend tests conducted in the previous study, the composites in the present study are mechanically tested using POR bend testing in order to characterise the properties in all direction of the disk sample plane. Moreover, the composite properties are studied using ANA (analytical) and FEA (finite elements analysis) modelling. Experimental and modelling results are compared in order to shed light on the quality of interface bonding and other effects of the used fabrication technique.

2 LITERATURE REVIEW

2.1 Composite materials and their constituents

2.1.1 Carbon fibers classifications and properties

Per definition, carbon fibers (CF) contain at least 90% carbon. They are heat treated at lower temperatures between 1000 and 1500°C, while graphite fibers are generally heat treated at higher temperatures of about 2000°C [1]. Most carbon fibers are in the nongraphite stage and feature a polycrystalline microstructure [2]. The basic structure of carbon fiber, from the graphitic unit to microdomain filaments, is illustrated in Figure 2-1. The planar hexagonal network of the 2D long-range structure is restrained in carbon fiber and determinant for the carbon fiber properties [3]. Thanks to continuous industry demand, research and development, including innovations from carbon fibers to carbon nanotubes, the mechanical properties of advanced carbon fibers currently span an extraordinarily large range [3].

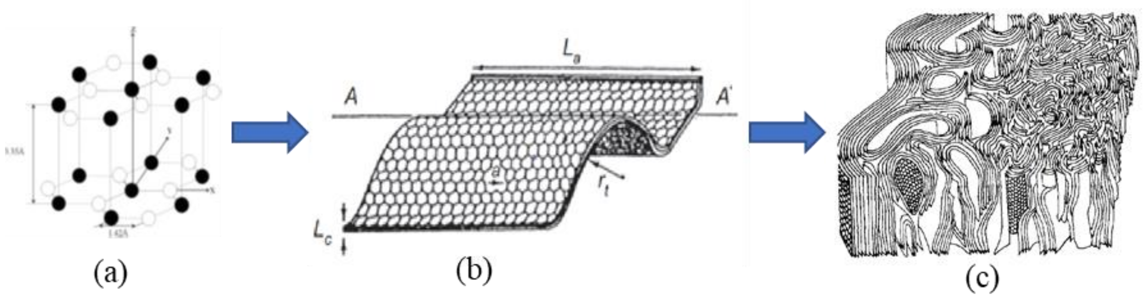

Figure 2-1: Microstructure and composition of carbon fibers: (a) graphitic crystal structure; (b) carbon layers structure; and (c) texture structure of carbon fiber filaments [3][4][5]

Historically, Thomas Edison baked cotton threads at high temperature in 1897 using an electric lamp, and by so doing produced what can be regarded as the first carbon fiber. Half a century later in the 1950s, the Nation Carbon Company produced high stiffness carbon fiber in the United States by carbonizing rayon. At about the same time, polyacrylonitrile (PAN) based carbon fiber was fabricated by Akio Shindo in Japan. In the 1970s, Pitch-based carbon fiber was invented by Leonard Singer [6]. Since then, research and inventions on CF have intensified continuously. Recently, the development of carbon fiber has expanded to more complex geometries such as hollow structures, and later into the nanoscale including carbon nanotubes and nanoparticles [7][8].

2.1.2 Types of carbon fibers

In the modern industries, carbon fibers are fabricated starting from different types of precursors using specific heat and surface treatment regimes. Available precursors include PAN (Polyacrylonitrile), pitch, and rayon. Different precursor selection can dramatically alter carbon fiber properties. Since high-performance PAN-based carbon fiber was invented, PAN has become the main precursor for most technological applications. More than 95% of the global production of carbon fiber is PAN-based [3]. For this reason, PAN-based carbon fiber is selected for this study.

The most important characteristics of carbon fiber precursors are high carbon content [9], high orientation degree [3], high heat stability, and good molecular activity [10]. Cellulosic polymers, such as cotton, flax and silk fibers, are potential ideal precursors for carbon fiber fabrication. However, their high defect concentration deteriorates their mechanical performance. Therefore, the industrial use of the resulting fibers has so far been limited. In contrast, PAN based precursors produce carbon fibers with highly ordered structure and thermal stability thanks to high carbon yield [11]. The basic molecular structure of PAN is $[C_3H_3N]_n$ as shows in Figure 2-2. Due to strong carbon chain bonds, PAN is a high melting point, stable and hard polymer, which is perfectly suitable as carbon fiber precursor [11].

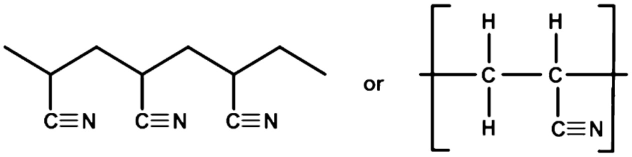

Figure 2-2: Basic chemical structural unit of PAN based carbon fiber [11]

The simplified flow chart for producing PAN precursors is shown in Figure 2-3. The process usually starts with comonomer polymerization. The type of comonomers, such as Vinyl esters and Carboxylic acids, determines the process effectiveness and the mechanical properties of the final precursor. In this aspect, comonomers with high molecular orientation and reactivity have proven the most appropriate [10]. The next sub-process is to make precursor fibers. Traditional spinning processes, such as wet spinning, remain the most prominent processes for PAN precursors. Here, the polymer first goes through a solution and then through a steam cleaning step. Processing at higher temperature can improve the strength of the final precursor [10]. Moreover, post-processing of PAN-based precursors can further improve the mechanical properties by increasing the order of carbon atoms and by reducing impurities [5].

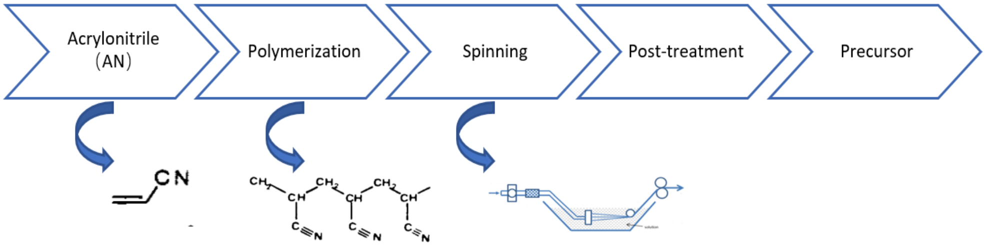

Figure 2-3: Flow chart of PAN based precursor processing [3][9][12]

PAN-based precursors are then generally processed into carbon fibers using the following steps: stabilization and carbonization as seen in Figure 2-4. The stabilization or oxidation process is critical as the first stage to achieve high-performance carbon fibers. PAN-based precursors are often stabilized in air at low temperatures between 200 and 300℃. Stabilization takes place by oxidation and is exothermic, thus precise temperature control is essential for carbon fiber properties by limiting carbon chain melting and displacement. The oxidation process can be time consuming and can take hours. However, the result is a heteroaromatic structure that significantly improves the thermal stability allowing the resulting fibers to sustain high temperatures during subsequent heat treatments. The stabilization process is followed by carbonization, whereby fibers are heated to high temperatures in stabilizing gases such as nitrogen (N_2) and argon (Ar) [12]. The carbonization process takes place in two stages: (1) Dehydrogenation reaction at a low temperature ranging from 400-

600℃; and (2) Denitrogenating reaction at a high temperature ranging from 600-1300℃. Furthermore, graphitization is used after carbonization in the case of graphite fibers.

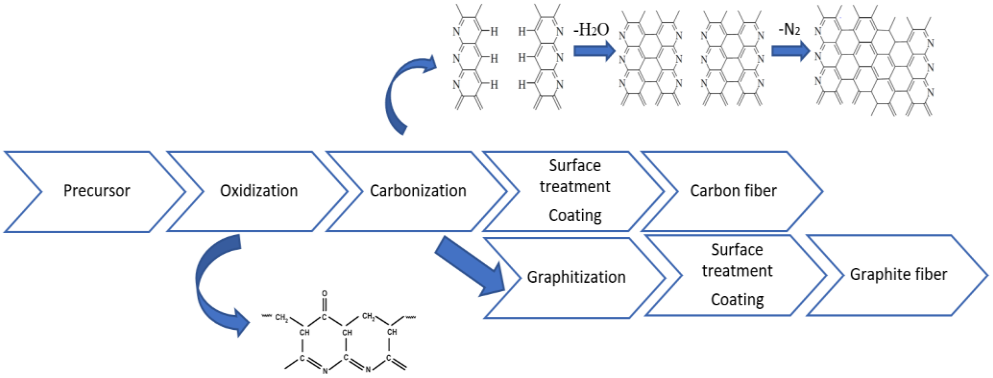

Figure 2-4: Post processing of PAN based precursor to produce carbon or graphite fibers [11][3]

Overall, the amount of cross-link formation between the precursors during the polymerization reaction allows the growth of a sheet structure arranged in the fiber directions. Subsequently, carbonization allows dramatically increasing the purity of the carbon fiber with the elimination of hydrogen, nitrogen and oxygen [12]. The higher temperatures used for the carbonization reaction minimize defects and porosity and increase the flexural strength and young's modulus of the final fibers. However, excessively high temperature beyond 1600℃ can deteriorate the carbon fiber properties due to excessive atomic activity [3]. Graphitization at temperatures between 2000 and 3000℃ for 10s to 5 mins allows a re-arrangement of the crystal structure to produce graphite fibers. In general, higher carbonization or graphitization temperatures tend to produce amorphous carbon structures which behave like fine crystal structures. Closing surface treatments at the end of processing, such as coatings, can be used to protect the fibers and improve the shear strength of the final composites.

2.1.3 Carbon fiber properties

The mechanical performance of carbon fibers is highly related to their microstructure. The main defining parameters are the crystal size, the orientation, the impurity and the porosity, all of which heavily depend on the used precursor. It has been reported that PAN-based carbon fibers with smaller crystal sizes have better performance concerning the tensile strength and compressive strength compared with pitch-based fibers [11]. However, even identical precursors can still produce varying fiber performances depending on the manufacturing process. Figure 2-5 shows the tensile property ranges of fibers made from different precursors.

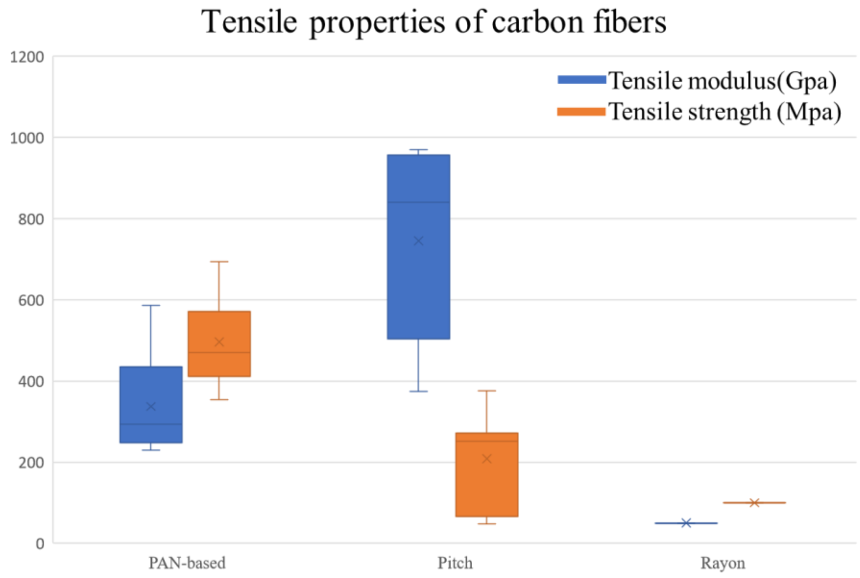

Figure 2-5: Tensile properties of carbon fibers fabricated using different precursors [4][9][13]

Carbon fibers can be divided into three main groups: high modulus, high strength, and isotropic carbon fibers. Their crystal orientation and fiber diameter primarily define properties. Thus, carbon fibers can be tailored to a large range of application requirements. Carbon fiber as a reinforcement material can significantly increase the strength of materials and provide improved specific properties, including low thermal expansion and high wear resistance. For metal matrix composites (MMCs), specifically for carbon fiber reinforced aluminum matrix composites, high young’s modulus combined with a considerable flexural strength are the desired mechanical properties and main requirements for structural application. PAN-based carbon fibers are best positioned to meet these requirements, and are, therefore, selected as reinforcement in the present study.

2.2 Forms of carbon fibers

Carbon fibers can be classified according to their length into continuous and discontinuous carbon fibers. Short fibers, whiskers, particulates, and carbon nanotubes belong to the class of discontinuous carbon fiber. The mechanical properties of composites reinforced with discontinuous carbon fiber can be varied depending on the specific fiber form. The most crucial advantage of discontinuous carbon fiber reinforced composites is highly isotropic properties. As such, they are more suitable for use in wear and high temperature applications.

Continuous fiber reinforced composites are marked by dramatically improved strength and stiffness. It is because the long fibers can more efficiently transfer and carry the load in their length direction. The fatigue performance of continuous fiber composites is strongly enhanced as well because of the lower interface area, which creates fewer sites for potential crack initiation. In this regard, the application of continuous fiber reinforced composites is advantageous in mechanically highly demanding applications with clearly defined loading direction. The mechanical properties of continuous fiber reinforced composites can be varied using different carbon fiber types and arrangements. While unidirectionally oriented fibers provide the highest strength and stiffness performance in the fiber direction, bidirectionally and multi-directionally oriented fibers provide more balanced performance in the different room directions. In this case, particularly woven fiber fabric composites, often called textile composites, are increasingly gaining popularity in the science, research and engineering community [14]. The preference and superiority of woven fiber fabric are also due to their increased practicability and economical efficiency thanks to the ease of fabric transportation and automatic composite fabrication [15].

The mechanical behavior of textile fibers depends on their woven architecture. The fabric behavior and performance are determined by the structure elements, including the wrap, the weft and the weave. The basic woven fabric structures include the two directional interlaced threads with the warp running thought the length, the weft running along the width, and the weave being the pattern by which wrap with weft interlace and hold each other [16]. Figure 2-6 describes some of the basic woven patterns. Furthermore, fabric structures are not limited to 2-dimensional geometries [17]. 3D fabric preforms have also found widespread use in metal matrix composite manufacturing. However, the design difficulty and process complexity of 3D preform result in high manufacturing costs. Similar to continuous fiber, discontinuous fiber preforms are also suitable for composite manufacturing. However, the choice of patterns is limited due to their short length [18]. Plain weave carbon fabric is selected in the present work due to its simple unit cells and good adjustability.

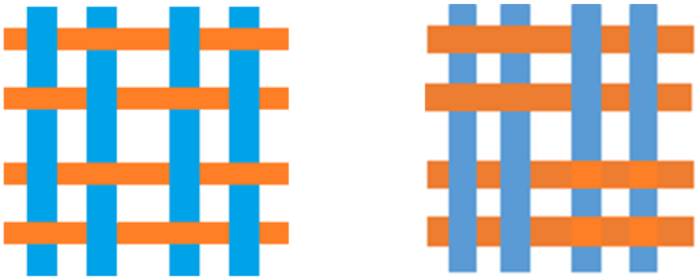

(a) 1/1 Plain weave

(b) 2/2 matt

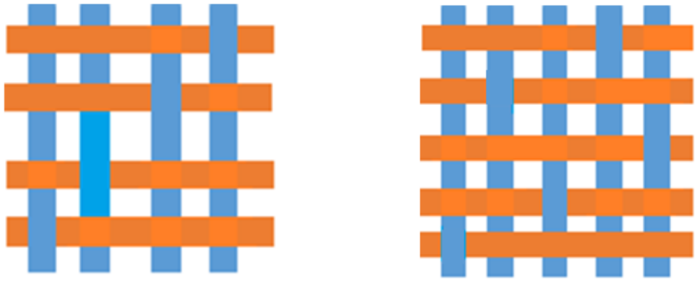

(c) 1/3 twill

(d)1/4 sateen

Figure 2-6: Basic 2D fabric patterns of composite materials [16]

2.3 Aluminum alloys and their properties

Light weight, low price, comprehensive mechanical behavior and excellent machinability make aluminum and its alloys some of the most popular candidates for composite matrix materials [19]. Moreover, aluminum shows good corrosion resistance due to a thin protective alumina film at the surface. By applying different alloying elements and strengthening mechanisms, as well as by incorporating fiber reinforcements, the overall aluminum composite performance can be significantly improved [19]. Aluminum alloys are often classified according to their manufacturing route into wrought and cast aluminum alloys [20]. The properties of cast alloys are primarily optimized by appropriate strengthening effects using heat treatments, while the properties of wrought alloys are primarily optimized by appropriate deformation regimes.

Copper is one of the main alloying elements in aluminum alloys, specifically for the 2xxx series. As a result of copper addition, aluminum alloys can possess improved high temperature performance as well as good electrical conductivity, which has enabled their widespread use as electric wire [20]. Silicon is another prominent alloying element for aluminum. It can improve aluminum alloy strength and hardness. Due to the low solid solubility of silicon in aluminum, the strength increase achieved with Si addition is primarily by precipitation strengthening mechanisms [21]. Moreover, the presence of hard silicon phases in aluminum alloys can significantly enhance their wear resistance. Furthermore, silicon improves the fluidity, which eases preform or fiber penetration by liquid aluminum in fabrication processes such as squeeze casting. Beside Copper and Silicon, Magnesium is an important alloying element for aluminum. It can contribute to strengthening the alloy by solid solution strengthening. Aluminum-magnesium alloys often possess good thermal conductivity. Together with Silicon, Magnesium can form Mg_2Si hard phases to further improve the strength of aluminum alloys. Al-Mg-Si alloys are well known as the 6xxx series [21]. The addition of small quantities of copper and zinc can significantly improve the corrosion resistance and weldability. Today, 6xxx series alloys have become some of the most important high quantity aluminum alloys and are extensively used in the aerospace and transport industries. In this study, sheets of aluminum alloy 6061 are selected to combine with carbon fiber fabric layers to produce laminate composites with improved strength and young’s modulus [21].

2.4 Heat treatments

As mentioned above, cast aluminum alloys, such as Al-Cu, Al-Mg-Si, Al-Zn alloys, are heat treatable and precipitate hard phases during heat treatments to optimize and improve the final properties [22]. A good heat treatment regime designed to form uniformly distributed fine precipitates is one prominent option to achieving the best properties.

The standard specifications for different aluminum heat treatment regimes, as formulated by the USA Aluminum Association, are summarised in Table 2-1 [23]. The most widely used heat treatments for aluminum alloys are T4 and T6. Cast alloys can be heat treated immediately after casting. In contrast, wrought alloys are usually first annealed after casting to improve their formability [23]. Solution heat treatment at high temperature allows the non-equilibrium hard phases to be dissolved, yielding a homogenized single-phase matrix microstructure.

Table 2-1: Classification of heat treatments for aluminum-based alloys [23]

Heat treatment	Description
F	As-casted, without any thermal heat treatment or work hardening
O	Annealing, homogenizing heat treatment
T4	Solution heat treatment, quenching, followed by natural aging
T6 (T5)	Solution heat treatment, quenching, followed by artificial aging
T8 (T7)	Solution heat treatment, quenching, followed by artificial overaging
T10 (T9)	Solution heat treatment, quenching, aged and cold working

Quenching is a rapid cooling process after the solution heat treatment of alloys to achieve a sharp temperature drop. The main methods of quenching are air quenching, water quenching and oil quenching. In some cases, a high degree of undercooling can result in a dispersion of fine precipitates during quenching. The aging process follows quenching and can be classified into natural aging and artificial aging. During aging, the supersaturated solid solution obtained after quenching gradually transforms into a stable two or more phases alloy microstructure. This yields a precipitation strengthening and an increase in alloy strength. However, overaging can produce coarse precipitates leading to a decrease in mechanical strength [24]. Therefore, accurate processing parameters, such as heat treatment temperature and duration, are generally varied to achieve the desired alloy properties depending on the intended application.

2.5 Manufacturing processes

The requirements for metal processing equipment are strict due to the high melting point of metals and to avoid defects such as oxides and pores. For MMC, the mostly used processes are squeeze casting, liquid metal infiltration, stir casting and powder metallurgy. In the current study, aluminum is reinforced by continuous carbon fiber fabric. A critical challenge in casting fiber reinforced composite materials is to keep the fibers or woven fabric layers in their original shape while achieving good bonding with the aluminum matrix. In the final composites, the matrix provides ductility and protection to the fibers while the reinforcement provides strength. However, this can only be achieved when a good fiber-matrix interface bonding is attained. The nature and quality of the interface bonding are defined by fabrication process parameters, particularly the contact duration between fibers and the molten metal, the fabrication temperature and pressure, as well as the solidification rate.

2.5.1 Squeeze casting

Squeeze casting has attracted enormous attention from the scientific and manufacturing community for the fabrication of MMC. Two of the unique advantages of squeeze casting are:

First, it produces composites with substantially lower porosity as it can prevent the formation of gas and hydrogen microporosity while compensating shrinkage [25]. Similar to traditional pressure die casting, squeeze casting uses external pressure for consolidation during solidification. In contrast to traditional pressure die casting however, the squeeze casting set-up does not have any gating system. The gating system in standard pressure die casting can significantly improve the fabrication rate, but more air and gases can enter the molten metal and stay in the material during the process. Furthermore, a substantial amount of pressure is released due to shrinkage during solidification, which reduces the heat transfer and cooling rate resulting in larger grain sizes [26]. In contrast, pressure is maintained at high levels during solidification in squeeze casting, yielding finer grain sizes, better microstructure and higher strength and hardness [26].

Second, poor wettability between molten aluminum and carbon fiber is a major challenge in composite fabrication and can lead to porosity and weak interface bonding, which can dramatically reduce the load transfer capacity across the interface. Squeeze casting can address this challenge as the applied hydrostatic pressure decreases the contact angle, improves molten metal infiltration and enhances wetting. Also, the squeeze pressure accelerates composite cooling during solidification, which reduces contact time and aluminum carbide formation [25].

Squeeze casting process (as show in Figure 2-7) combines the advantages of die pressure casting and forging. Preheating of the squeeze casting die has proven to yield higher composite tensile strength. During squeeze casting, pressure is applied when aluminum is in the molten state to achieve good infiltration. Pressure is maintained during solidification to accelerate cooling and reduce porosity. Moosa et al. tested PAN-based carbon fiber reinforced 1725 DIN aluminum alloy fabricated by squeeze casting and established the relationship between pressure and ultimate tensile strength (UTS) [27]. In the low pressure range, UTS initially increases with pressure. This is due to improved infiltration and wetting of the reinforcement by the matrix liquid leading to more stable interface bonding. They achieved a plateau in UTS between 20 and 40 MPa. Beyond this plateau, the ultimate tensile strength decreased with further increasing pressure primarily due to carbon fibers clustering and breakage.

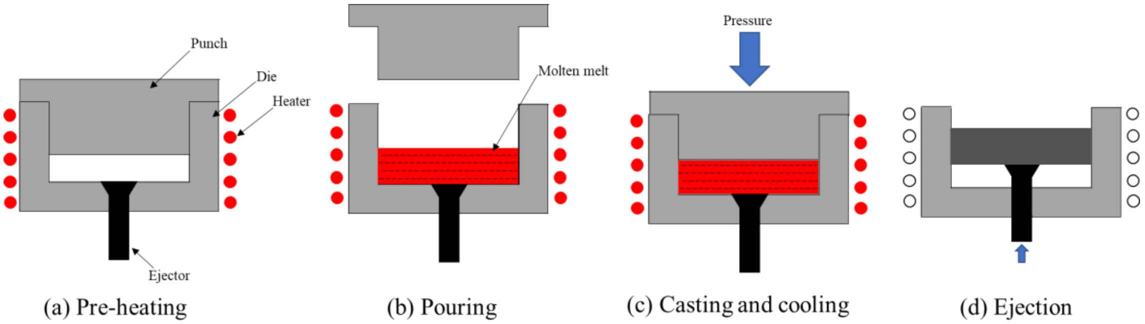

Figure 2-7: Schematic diagram of basic squeeze casting steps

2.5.2 Stir casting

Stir casting has proven efficient in processing composite materials with a desired reinforcement distribution. An important design of the stir casting set-up is the stirrer geometry. The common shapes of stirrers are shown in Figure 2-8 [28] [29]. Further parameters like stirring speed, stirring position and casting temperature affect the final composite properties as well. Stir casting is characterised by high metal flow rate during stirring and is more suitable for short fibers or discontinuous reinforcements. Stir casting has found widespread use in industry for composite fabrication due to the simplicity of required equipment, its large flexibility and its reduced cost [29].

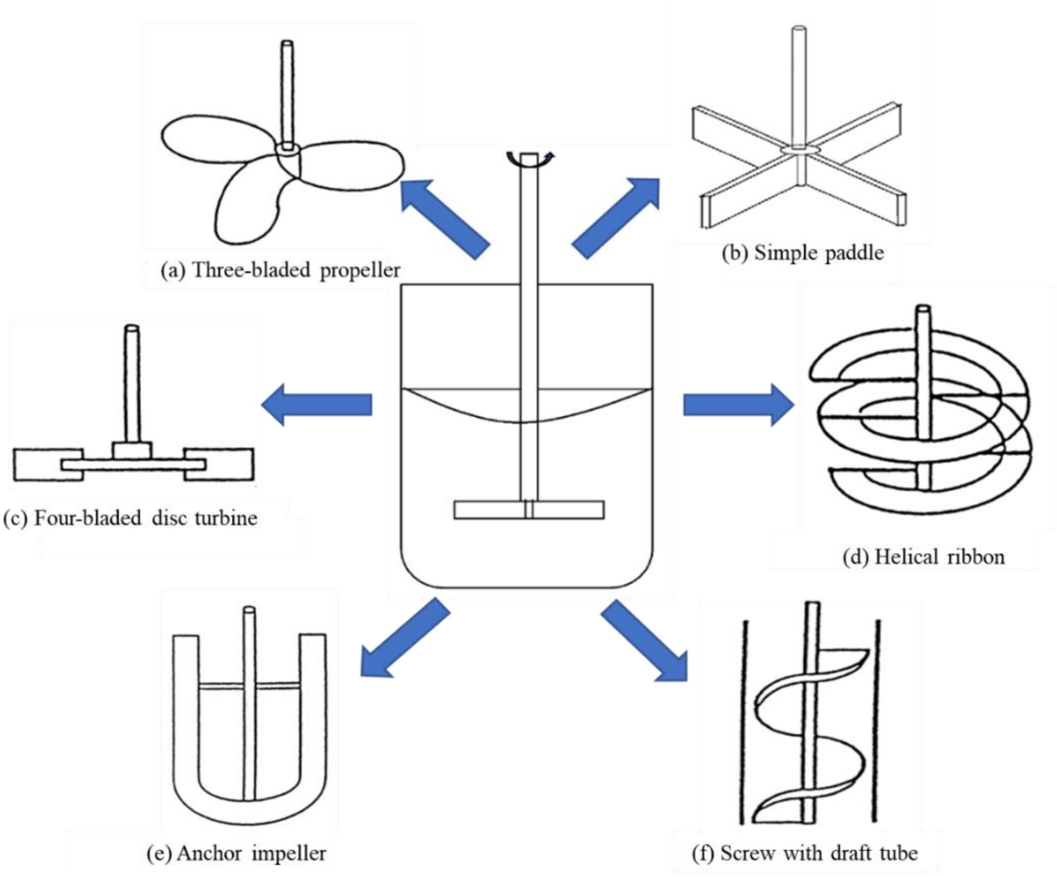

Figure 2-8: Shapes of stirrer for stir casting [28] [29]

However, stir casting has multiple limitations as well. First, it is not suitable for continuous reinforcements such as continuous fiber fabric. Secondly, reinforcement wettability by molten metal, and consequently interface bonding, can be poor due to low pressure. Thirdly, gas mixture during stirring can increase the porosity. Eventually, excessive contact with air can result in increased oxidation in the fabricated composites [28].

2.5.3 Powder metallurgy

Powder metallurgy has been successfully used to fabricate both continuous and discontinuous fiber reinforced composites. The main competitive advantages of powder metallurgy are the precise control on final component shape and the advanced uniformity of reinforcement distribution. Moreover, powder metallurgy has good economic efficiency due to the high product quality and accuracy, which often do not necessitate post-processing. Figure 2-9 provides a simplified illustration of the powder metallurgy process as performed by Alcoa. The reinforcement is mixed with matrix powder during blending and subsequently consolidated and processed into a near-net-shape part [30].

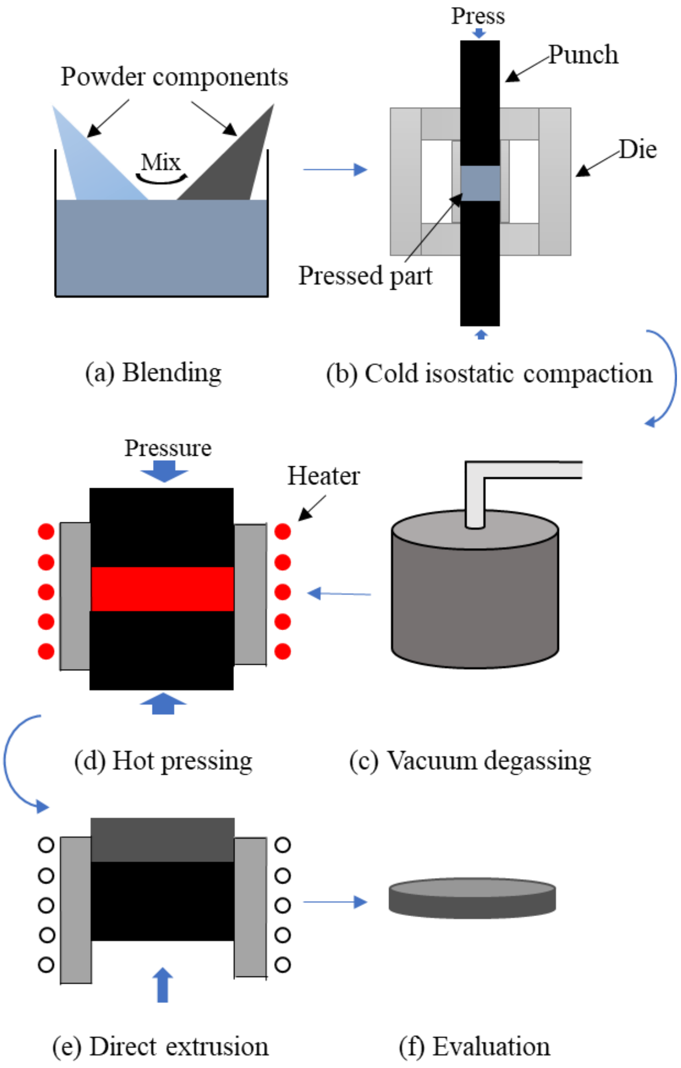

Figure 2-9: Powder metallurgy processing for composite fabrication [30]

Since the temperature is maintained at a low range, solid state diffusion controls interface bonding and high forces during hot pressing result in a good bonding strength between reinforcement and matrix. Moreover, the size of powder strongly influences the final material properties. The main disadvantages of powder metallurgy include relatively high costs compared with casting, potential hazards during processing posed by the relatively small size of the powder particles, and generally lower elongation to fracture compared with liquid phase processed materials [31].

2.6 Properties of aluminum matrix composites

2.6.1 Wettability

For MMCs fabricated by liquid phase processes, the wetting behaviour between metal and reinforcement is crucial for the final mechanical properties. The most common measure of the wetting behavior at the interface is the contact angle. The contact angle is defined by the interfacial energies between solid, liquid and vapour phases as illustrated in Figure 2-10 [32]. If the contact angle is larger than 90º as seen in Figure 2-10 (b), the system is unfavourable to wetting and results in low interface adhesion. As the contact angle decreases, the interaction strength increases, and perfect wetting is achieved when the angle has a value of 0º. In general, aluminum shows poor wettability with most ceramic and carbon reinforcements [33]. This constitutes one of the most crucial challenges for the fabrication of aluminum based composites. Therefore, a great deal of research has focused on the wettability and interface properties that ultimately define the interface bonding strength in aluminum matrix composites [34].

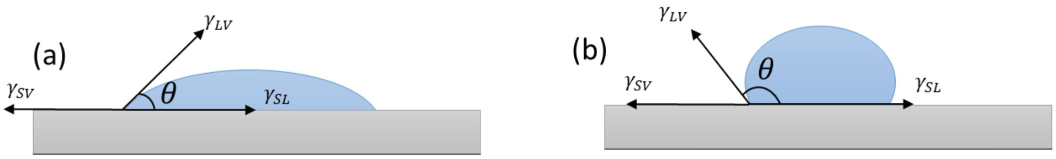

Figure 2-10: Interfacial energies at liquid-solid interface: (a) self-wetting; (b) non-wetting [32]

The influence of wetting in composite fabrication is a complex problem that is still not clearly understood. However, it is well known that the contact angle deceases with the processing temperature. Moreover, the wettability of metals increases when the surface oxide film is dissolved. For interfaces undergoing chemical reactions such as aluminum with carbon materials, the wetting behaviour can also improve when reaction takes place [33]. At high temperature, metals react stronger with the environment while the imperfect surface of reinforcements also reduces their contact area. In order to achieve composites with reliable interface strength, relatively high external pressure is generally used to increase the effective surface area, the surface energy, liquid infiltration and wettability.

2.6.2 Reinforcement-matrix interface bonding

Interface bonding between fibers and matrix can be by mechanical locking, electrostatic attraction, diffusion or chemical bonding. The main types of interface bonding between two phases are shown in Figure 2-11 [2]. The interface is generally coherent in the case of bonding between two phases with similar lattice parameters. This kind of interface is usually observed for precipitates with similar crystal structure as their metal matrix. As the mismatch between the phases increases, the interface bonding type generally changes to semi-coherent and incoherent. Incoherent bonding is obtained for particles with substantially different lattice structures compared to the matrix. Incoherent bonding results in higher bonding energy due to a large degree of atomic disorder, resulting in stronger restricted dislocation motion at composite interfaces during plastic deformation [19]. The bonding of metal with fiber reinforcement is dominated by diffusion due to high temperature processing. Therefore, the initially completely incoherent interface, due to the difference in crystal structure, can transform into a semi-coherent bonding by the formation of a diffusion zone at the interface.

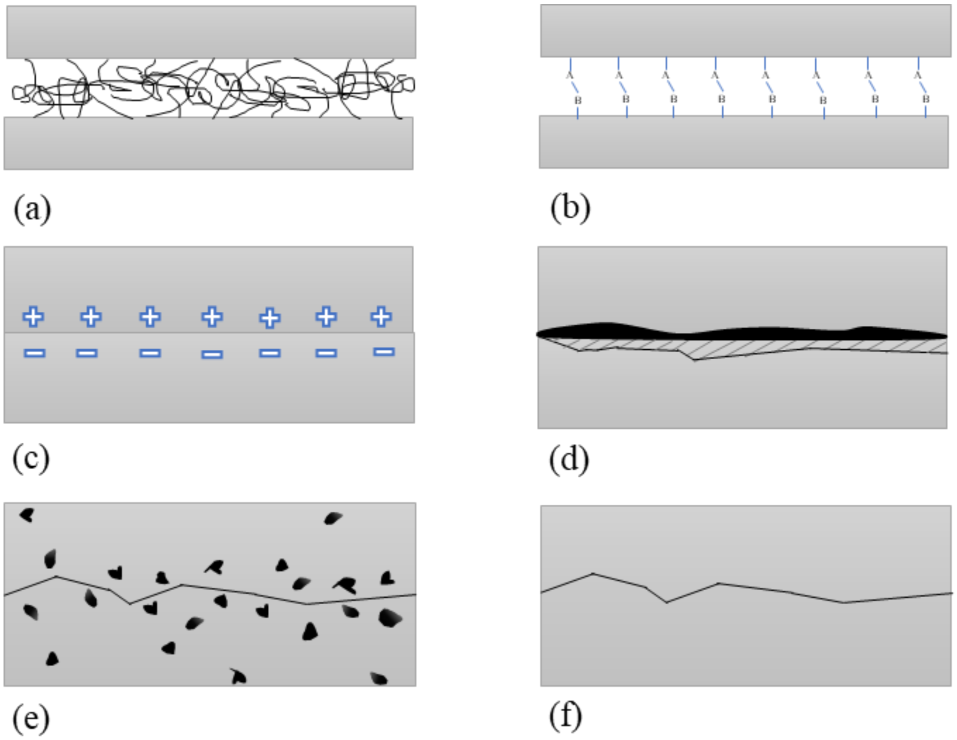

Figure 2-11: Interface bonding mechanisms between two phases: (a) Molecular entanglement; (b) Chemical reaction between groups A and B; (c) Electrostatic attraction; (d) New chemical reaction compounds; (e) Solid-state diffusion bonding; (f) Mechanical interlocking [2] [19]

Overall, MMCs can feature different types of interface bonding, among which, diffusion bonding is primary, while mechanical interlocking and chemical bonding are subordinate. The surface of reinforcements isn’t perfect, resulting in roughness that favours interlocking at the fiber-matrix interface. In this sense, mechanical bonding is practically universal in all fiber-metal composites. Mechanical interface bonding is mainly controlled by friction; thus, its primary effect is along the longitudinal direction, in which the shear stress acts at the interface. The coefficient of friction is defined by the surfaces and the roughness levels of both the matrix and the reinforcement. Although high roughness surfaces can generally increase interlocking effect, they can also cause a poor wetting behavior.

In MMCs, interface diffusion at the fiber-matrix interface often leads to atomic solution and the formation of reaction products. Also, the high manufacturing temperatures of MMCs lead to high energy kinetics, and rapid diffusion processes that can form strong interfaces due to solid solution effects. However, longer contact times can cause a substantial chemical reaction at the interface. The interface reaction products in aluminum based composites with different types of reinforcements are summarised in Table 2-2.

Table 2-2: Aluminum based composites and potential interface reaction products

Matrix	Reinforcement	Possible reaction products	References
$\mathbf{Al}$	C	$\mathrm{Al_4C_3}$	[35]
$\mathbf{Al}$	SiC	$\mathrm{Al_4C_3, C}$	[35]
$\mathbf{Al-Mg-Si}$	SiC	$\mathrm{Al_4C_3, MgAl_2O_4, MgO}$	[36]
$\mathbf{Al-Mg}$	$\mathrm{Al_2O_3}$	$\mathrm{MgAl_2O_4, MgO}, \alpha-\mathrm{Al_2O_3}$	[37]
$\mathbf{Al-Mg-Cu}$	$\mathrm{Al_2O_3}$	$\mathrm{MgAl_2O_4, CuAl_2O_4}, \alpha-\mathrm{Al_2O_3}$	[37]

2.6.3 Interface bonding strength

Aluminum 6061 is used as raw material in this study. As stated earlier, the interface energy between reinforcement and matrix with different crystallographic structures is comprised of a geometrical energy term and a chemical energy term [38]. However, the macroscopic interface bonding strength is also defined by the interface discontinuity and the thermal mismatch. One important factor to identify the fiber-matrix interface strength is interfacial shear strength.

Depending on the contact angle, the defects at the fiber-matrix interface during fabrication can strongly affect the interfacial shear strength. While completely wetted areas may produce good adhesion, the non-wetted areas can leave pores at the interface. Wetting also affects the pore shapes as described in Figure 2-12 [39]. Large contact angles produce a flat pore shape which leads to long defect length and high stress concertation. Moreover, in the case of fiber fabric reinforcement, there is a dense fiber packing in each tow. Therefore, poor interface wetting can cause high capillary forces. As such, providing efficient external pressure can help make sure the metal infiltrates throughout the fiber fabric and tows.

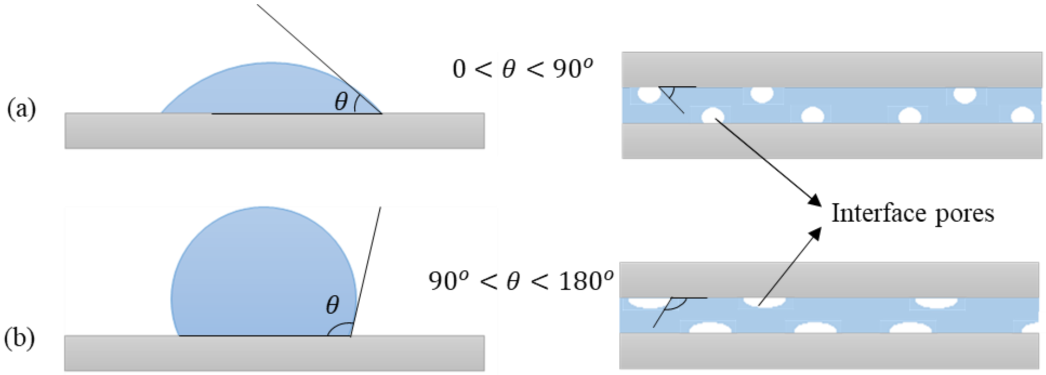

Figure 2-12: Wetting behavior of sessile drop and bonded interface: (a) non-wetting interface with more curvature interfacial pores; (b) self-wetting interface with less curvature interfacial pores [39]

The effect of chemical reaction at the interface can be twofold. On the one hand, a moderate amount of reaction can improve the contact angle, which leads to higher interface strength. On the other hand, excessive brittle phase formation can cause great damage at the interface. For carbon fiber reinforced aluminum matrix composite materials, aluminum carbide often forms. Aluminum carbide is an ionic compound with high hardness. Reaction equations that can take place at interfaces of carbon fiber reinforced aluminum matrix composites are given in Equation (2-1), (2-2) and (2-3) [33]. Aluminum carbide growth mostly follows the carbon fiber basal planes into the molten aluminum in two stages: first, carbon diffuses rapidly and homogeneously into the aluminum matrix driven by concentration differences. Specifically, carbide crystals can form with a needle geometry by diffusion processes controlled by concertation gradients between the formed carbide and the matrix near the surface [40]. Subsequently, the growth of carbide becomes controlled by the interface kinetics. It has been proved by T. Etter that carbide formation is more sensitive to time than to thermodynamics due to exothermic reactions [41]. In addition to being a brittle phase, interface carbides in aluminum matrix composites can further decompose with moisture as seen in Equation (2-4) [41]. One of the most efficient ways to avoid interface carbides is to apply high hydraulic pressure and reduce the contact time between fibers and molten aluminum during composite fabrication [41].

$$4\ Al(l) + Al_2O_3(s) \rightarrow 3Al_2O(g) \tag{2-1}$$

$$4\ Al(l) + 3\ C(s) \rightarrow Al_4C_3(s) \tag{2-2}$$

$$Al_2O(g) + C(s) \rightarrow 3Al(l) + CO(g) \tag{2-3}$$

$$Al_4C_3(s) + 12\ H_2O(s) \rightarrow Al(OH)_3(s) + CH_4\ (g) \tag{2-4}$$

The thermal expansion mismatch between the aluminum matrix and the reinforcement can also reduce the interface strength. The mismatch causes thermal stress built-up during fabrication as the aluminum matrix solidifies and hardens. In general, metals such as aluminum have higher thermal expansion coefficients compared to carbon fiber, which will cause tensile residual stresses at the interface. This can lead to cracking of brittle interface reaction products, such as carbides, during cooling and solidification.

3 METHODOLOGY

3.1 Material selection

3.1.1 Aluminum

The main alloying elements of Aluminum 6061 are magnesium and silicon. The detailed composition is shown in Table 3-1[42]. Good mechanical performance, high corrosion resistance, light weight and low micro-defect concentrations make aluminum 6061 one of the most important sheet metals used in different industries. Equally, it has drawn a lot of attention as a matrix candidate material for MMCs. Some relevant mechanical properties of Aluminum 6061 are shown in Table 3-2. The T6 heat treatment consists of a solution heat treatment followed by artificially aging in contrast to natural aging used for the T4 heat treatment state [43]. Although the young's modulus is often not strongly affected by the applied heat treatment, the ultimate tensile strength (UTS) and the yield strength are both highly dependent on the aging process [44].

Table 3-1: Chemical composition of Aluminum 6061 [42]

Component	Wt. %
Al	95.8-98.6
Mg	0.8-1.2
Si	0.4-0.8
Fe	Max0.70
Cu	0.15-0.4
Mn	Max0.15

Cr	0.04-0.35
Zn	Max0.25
Others (total)	Max0.15

Table 3-2: Mechanical properties of Aluminum 6061 [43][44]

Properties	**Young's modulus (E)**	**Shear modulus (G)**	**Poisson's ratio (v)**	**Yield strength (σ_y)**	**Ultimate tensile strength (UTS)**	**Elongation to fracture (el%)**
Al6061-T6	68.9 GPa	26 GPa	0.33	276 MPa	310 MPa	8–12%
A6061-T4	68.9 GPa	26 GPa	0.33	145 MPa	241 MPa	22–25%

3.1.2 Carbon fiber

For continues reinforcement composite materials, carbon fiber has a distinct superiority to other fiber reinforcements due to high flexural strength, young's modulus, fatigue strength and low density as well as negative thermal expansion coefficient. These properties, combined with metal matrixes such as aluminum and magnesium, give composites many important priorities including high stiffness-to-weight ratio and toughness. Carbon fiber reinforced composites have enormous competitiveness in aerospace, marine and automobile industries. Moreover, the high temperature and chemical stability makes this kind of composites more suitable for different environments.

AS4 Hexcel Carbon fiber is a high-quality PAN based fiber. Sizing is applied to improve the interlaminar shear properties. 3000(3K) filament count tows are selected in this study. Furthermore, the general properties of AS4 Hexcel Carbon fiber are tabulated in Table 3-3 [45]. It is well known that carbon fiber is an anisotropic material with great properties in the longitudinal direction, but weak performance in the transverse direction. However, this inherent anisotropy is important for the mechanical properties of plain weave carbon fiber fabric.

Table 3-3: Mechanical properties of AS4 Hexcel Carbon fiber [45]

Mechanical properties	AS4 Hexcel carbon fiber
Carbon content	94.0%
Density	1.79 $\mathrm{g/cm^3}$
Tensile strength	4,619 MPa
Elongation	1.8%
Longitudinal elastic modulus ($\mathbf{E}_{fx}$)	231 GPa
Transversal elastic modulus ($\mathbf{E}_{fy}$)	40 GPa
In-plane Poisson's ratio (v_{fxy})	0.2
Out-of-plane plane Poisson's ratio (v_{fyz})	0.25
In-plane shear modulus (G_{fxy})	20 GPa
Out-of-plane plane shear modulus (G_{fyz})	16 GPa

In order to manufacture composites with a uniform performance in the flat plane, a plain weaved fabric is chosen in this study. It has the same number of filaments in both weft and warp in a highly repeating pattern. This simple weave pattern can maximise the product stability.

3.2 Manufacturing procedure

Squeeze casting is used to manufacture carbon fiber reinforced aluminum matrix composites. Figure 3-1 illustrates the process flow in this study. The pressure during squeeze casting is partially provided by the thermal expansion differentials between punches and die. The process is optimised using different die designs and post-processing to achieve better interface bonding and improved composite properties. The finial products are composites with an alternating laminate structure.

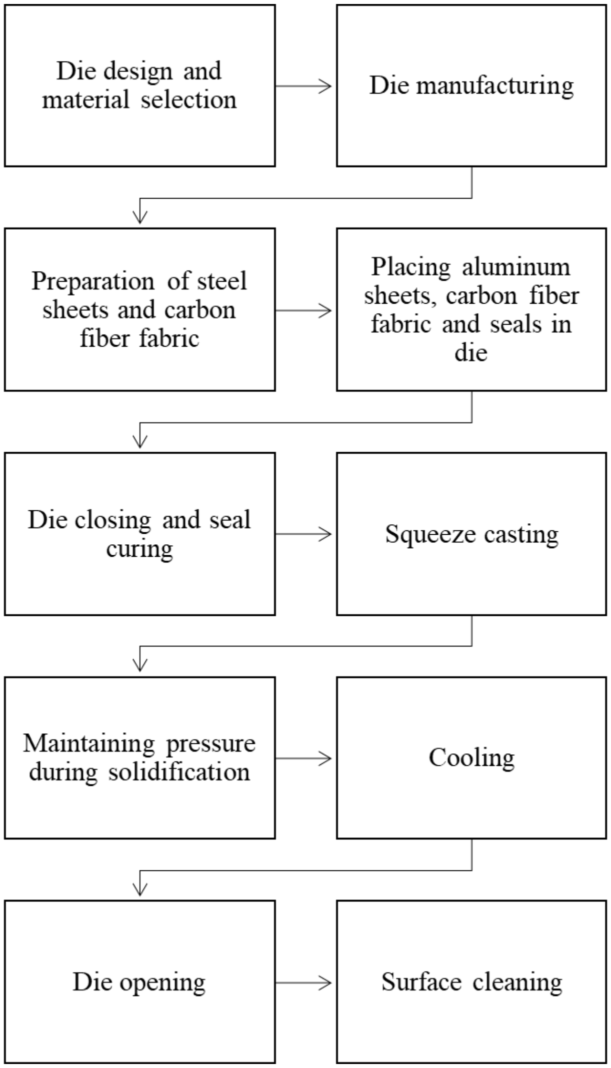

Figure 3-1: Flow chat of the squeeze casting process

3.2.1 Set-up of squeeze casting

3.2.1.1 **Casting mold design and materials**

The initial squeeze casting design at the beginning of the study is shown in Figure 3-2. It consisted of two thermal expansion inserts, two covers, and a die. The thermal expansion inserts play the role of punches and are made of steel 316 similar to the covers. Both have a higher thermal expansion coefficient of 21.55 µm/m-°C at 820°C compared to the die. The higher thermal expansion allows the inserts to apply squeezing pressure on the samples at the high temperature. The thermal expansion inserts are cylindrical with 15.5mm thickness and are designed to slide fit into the die. The die covers have 100mm diameter and 10mm thickness. They are assembled with the die using 6 stainless steel screws. The casting die and screws are made of stainless steel 17-04 with a lower linear thermal expansion coefficient of 11.8 µm/m-°C at 820°C. The casting die has 76.2mm (3 inches) inner diameter and is 38mm tall.

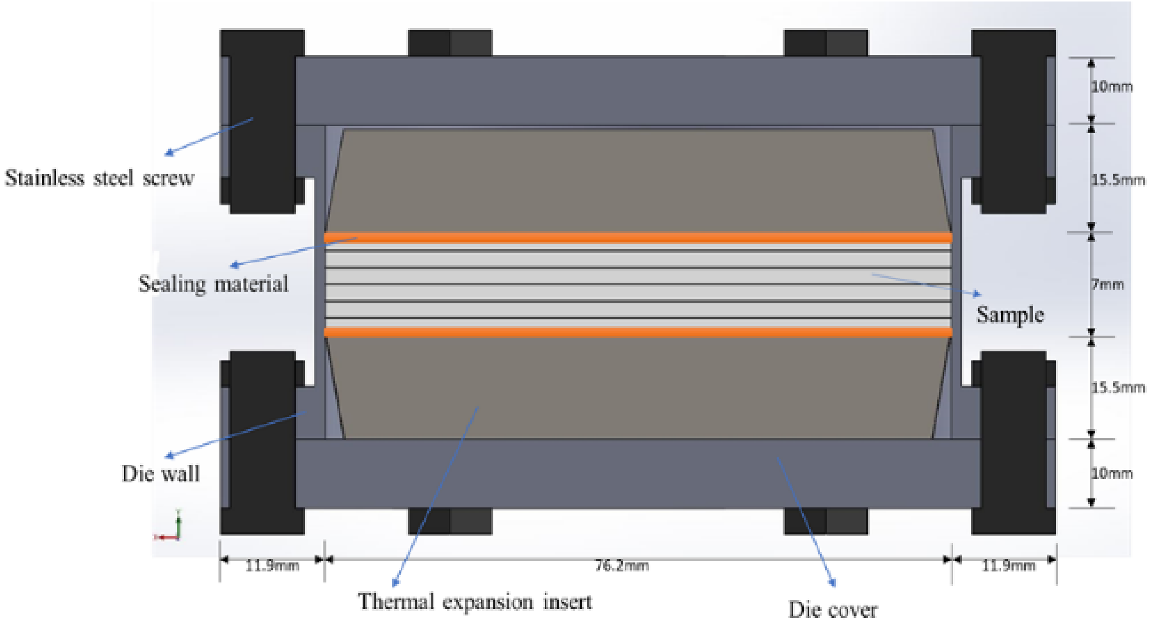

Figure 3-2: Axial section through the initial short casting die

To optimise squeeze pressure, a new long die design was developed with different die and thermal expansion heights as shown in Figure 3-3. The total length of the long die and its thermal expansion inserts are 76.2mm and 35.0m, respectively, compared to the initial short die with a total die length of 58mm and a thermal expansion inserts height of 15.5mm. To reduce weigh and heat capacity, the thermal expansion inserts of the long die are designed with a hollow structure as shown in Figure 3-3. Also, a large section of the insert height was made with a smaller diameter to reduce the contact surface and friction with the inner die wall. Moreover, the inserts and the cover screws were designed slightly longer than needed to close the die, which allowed pre-pressure to be applied on the laminate composite during die assembly. This also allowed additional post-processing pressure to be applied on the composite samples at the squeeze casting temperature using a hydraulic press without the need to open the die. Furthermore, the screw holes in the die covers were elongated radially to compensate for the difference in thermal expansion between the die and the die covers.

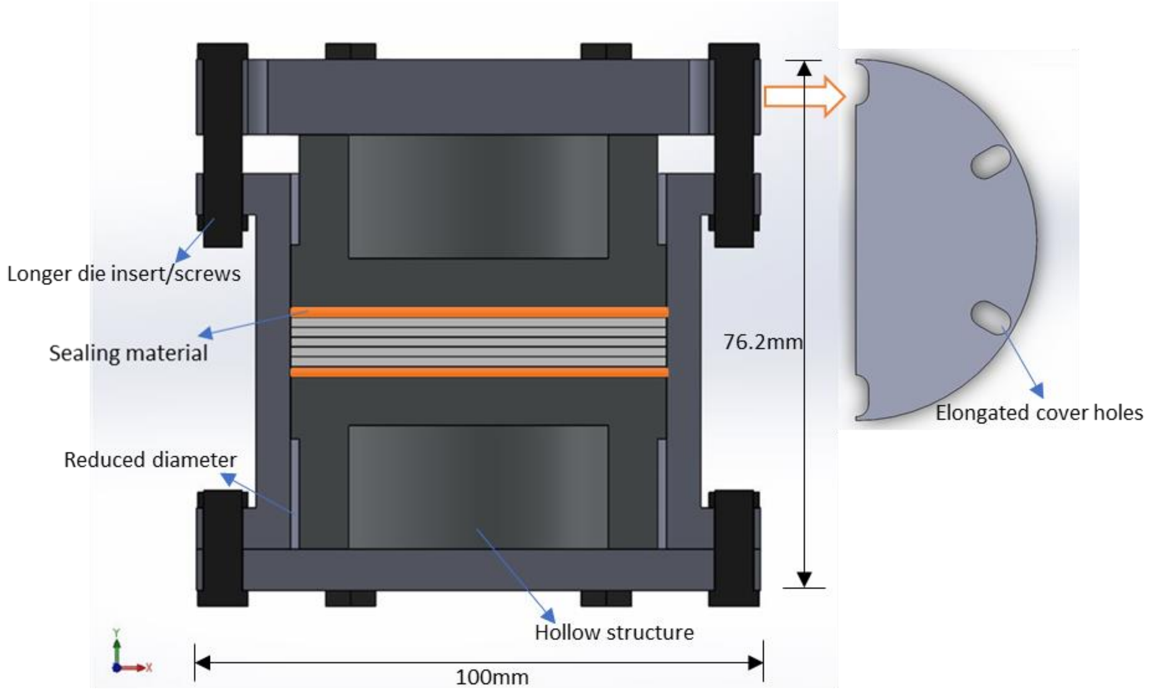

Figure 3-3: Axial section through the long casting die

Important mechanical properties of the main die materials, 316 and 17-04 stainless steels, are shown in Table 3-4.

Table 3-4: Properties of 316 and 17-04 stainless steels

Properties	316 stainless steel	17-04 stainless steel
Tensile strength (MPa)	579	1103
Yield strength (MPa)	290	1000
Modulus of elasticity (GPa)	195 (20°C) 157 (540°C) 143 (700°C) 131 (820°C)	203 (20°C) 169 (540°C) 139 (700°C) 127 (820°C)
Mean coefficient of linear thermal expansion (µm/m-°C)	--- (20°C) 19.80 (540°C) 20.97 (700°C) 21.55 (820°C)	--- (20°C) 11.4 (540°C) 11.6(700°C) 11.8(820°C)

Thermal expansion was found to potentially provide stable and sufficient pressure at high temperature without additional external compression. In addition, it allows keeping the die closed and sealed during the entire casting process, which simplifies the process and reduces oxidation reactions with air and environment. Moreover, the entire die set-up with sample is heated up and cooled together, which reduces thermal shock effects. However, the leakage of molten aluminum from the die can cause a strong pressure drop, making the process similar to pressure-less casting, and potentially leading to the production of porous and low-quality composites. Therefore, it is very important to completely seal the die, prevent liquid leakage and maintain pressure throughout the squeeze casting process. For this purpose, copper, brass and ceramic seals were investigated for preventing leakage at high temperature. Copper and brass have low hardness and good thermal expansion at high temperature. Their sealing function relies on plastic deformation under the squeeze pressure to stop the liquid flow. However, both alloys react with molten aluminum to form brittle aluminides. Therefore, an alternative seal choice was necessary. It is a Cotronics Resbond 907GF ceramic seal with high melting point and chemical stability. However, during casting die assembly, the Cotronics Resbond 907GF ceramic seal is still in a viscous semi-liquid state. As such, a small fraction of the seal was able to flow into the composite laminate under the initial assembly pressure. Moreover, as the seal cures at high temperature, the contained liquid evaporates and can cause porosity in the composite samples. Therefore, stainless-steel sheets are placed between the seal and composite sample, in order to prevent direct contact between seal and molten aluminum, help contain evaporation products, and provide a better surface finish of the fabricated composites. The stainless-steel sheets are cut with close tolerances to slide fit inside die. The thickness of the sealing materials, including stainless-steel sheets and ceramic seal, is controlled above 1.5mm on both sides of the laminate composite samples.

3.2.1.2 Estimation of thermal expansion squeeze pressure

During the casting process, the whole die set-up is kept closed. Hence, the compression pressure acting on the composite during squeeze casting can be calculated by the thermal expansions of the different components along the die axis. For simplification, radial thermal expansion and deformation are ignored. Moreover, each part of the die set-up is considered to deform purely elastically as shown in Figure 3-4.

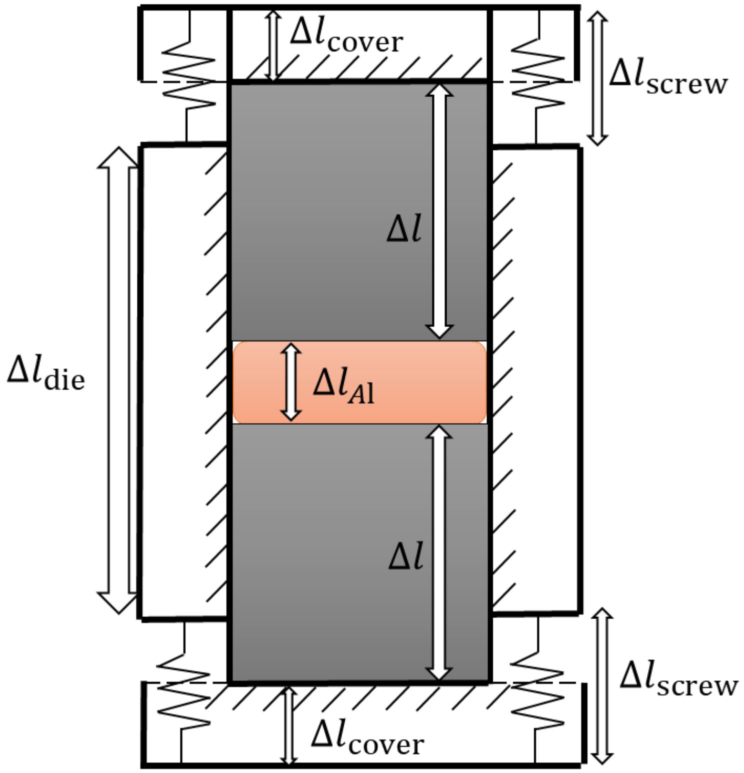

Figure 3-4: Illustration of the thermal expansion pressure during squeeze casting

The calculation of the squeeze pressure is primarily based on 2 variables: the expansion components and the restriction components as seen in Table 3-5. The expansion components include: the thermal expansion of both expansion inserts and die covers, the compression deformation of expansion inserts and die covers, and the volume expansion of the melting aluminum sheets (specified in Equation (3-1), (3-2) and (3-3)). The restriction components include: the thermal expansion and tensile deformation of the die and screws as shown in Equation (3-4) and (3-5). By combining all components, the deformation equilibrium of the whole die structure is expressed in Equation (3-6) and the finial pressure on the sealing material and sample is calculated by Equation (3-7).

Table 3-5: Pressure calculation of thermal expansion die design

Expansion components	$\Delta l = \Delta\alpha_{316} * \Delta T - \frac{F * t_{punch}}{E_{316} * A_{punch}}$	(3-1)
	$\Delta l_{Al} = \nabla \rho * t$	(3-2)
	$\Delta l_{cover} = \Delta\alpha_{316} * \Delta T - \frac{F * t_{cover}}{E_{316} * A_{cover}}$	(3-3)
Restriction components	$\Delta l_{die} = \frac{F * t_{die}}{E_{17-04} * A_{die}} + \Delta\alpha_{17-04} * \Delta T$	(3-4)
	$\Delta l_{screws} = \frac{F * t_{screws}}{E_{17-04} * A_{screws}} + \Delta\alpha_{17-04} * \Delta T$	(3-5)
Squeeze pressure	$\Delta l + \Delta l_{Al} + \Delta l_{cover} = \Delta l_{die} + \Delta l_{screws}$	(3-6)
	$P = \frac{F}{A_{punch}}$	(3-7)

Where Δl, Δl_{Al}, Δl_{cover}, Δl_{die} and Δl_{screws} are the total length changes of punches, melting aluminum sheets, covers, die and screws, respectively; ΔT is the change in temperature; $\nabla \rho$ is the change in density of molten aluminum; F is the internal force; t, t_{punch}, t_{cover} , t_{die} and t_{screws} are the thickness of composite, punch, cover, die and screws, respectively; A is the cross-sectional area of each component; $\Delta\alpha$ and E are the coefficient of linear thermal expansion and elastic modulus of 316 stainless steel and 17-04 stainless steel, respectively; P is the squeeze pressure.

3.2.2 Sample preparation

1mm thick Aluminum sheets are machined to 76.0mm circular disks using a lathe. The disks are cleaned in acetone using a DIGITAL PRO ultrasonic cleaner at room temperature for 20 minutes to remove impurities on the surface, and then heat dried. It is well known that an aluminum oxide layer with high melting temperature can for on the aluminum alloys. Such a thermally stable oxide scale can obstruct the flow of molten aluminum, which can potentially limit direct contact with carbon fiber. To investigate this risk, aluminum disks with smaller 62.0mm and 57.5mm diameters are used for some samples besides samples with 76.0mm diameter disks that slide fit into the dies as illustrated in Figure 3-5. The assumption was that the smaller diameter disks could flow radially during squeezing, thereby stretching, deforming and ultimately breaking the surface oxide scale as shown in Figure 3-5 (b), allowing molten aluminum to break free, wet and infiltrate the carbon fiber fabric. To ensure that the fabricated composite samples have similar thickness and total volume, 4, 6 and 7 aluminum layers are used for the 76.0mm, 62.0mm and 57.5mm diameter disks, respectively.

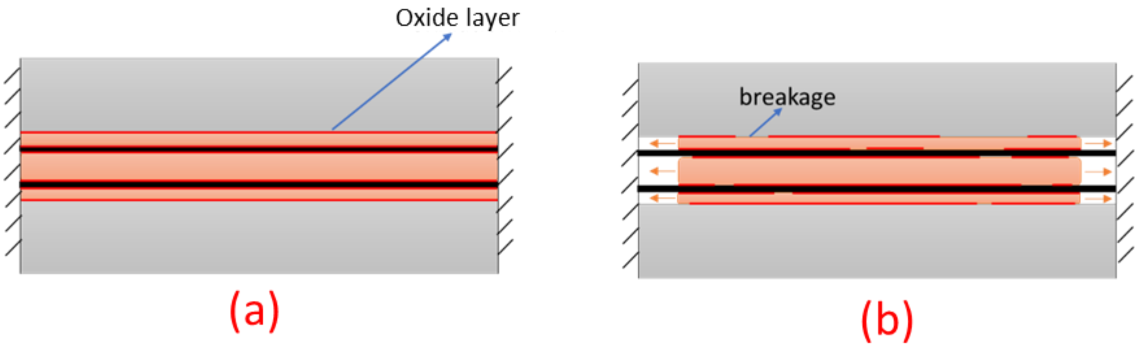

Figure 3-5: Molten aluminum flows under squeeze pressure: (a) full size aluminum disks with diameter slide fitted into the die; (b) small aluminum disks with smaller diameter allowing radial flow

To allow the carbon fibers to be completely enclosed inside the composite samples, the fiber fabric is cut by scissors to 63.5mm diameter disks, which is 0.5 inch smaller than the inner diameter of the die. The fiber fabric disks are then cleaned by hand using acetone and air dry. No ultrasonic cleaning is used as it would break the fabric structure. For different carbon fiber volume fractions, the packing space between yarns is changed by removing some yarns on the sides in the 2 plane directions and then pushing the remaining yarns apart. This allowed keeping the original fabric pattern. The process is illustrated in Figure 3-6.

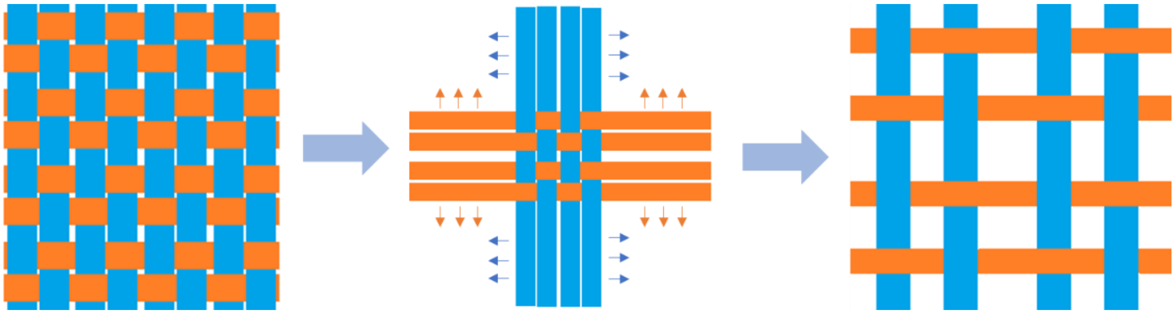

Figure 3-6: Process of changing carbon fiber volume fraction

SLIDE Hi-Temp 1800 mold release and lubricant is selected for the casting tests. It possesses a high melting point, which prevents aluminum from sticking on die set-up parts after cooling. The mold release is sprayed in thin layers to cover all surfaces in contact with molten aluminum, including punches, inside die wall and steel sheets. After release spray, all components are left to dry in air. The process is repeated 3 times to obtain a continuous coating of mold release.

The copper and braze seals are directly assembled into the casting die between the steel foils and the thermal expansion inserts. As alternative, a ceramic seal material, 907GF smooth fine grade putty with 1200℃ maximum allowable temperature, is used. The application of the ceramic seal starts with the bottom side of the die. First, the bottom thermal expansion inserts or bottom punch is placed into the die and the base of the die is closed using the bottom cover and screws. Then, the ceramic seal is applied at a thickness of 5mm on top of the punch and then the bottom steel sheet is placed on the seal layer. The steel sheet is pressed against the seal to eliminate gaps and the excess seal is removed. At this stage, the die set-up undergoes a first curing step in an air furnace at 200℃ for 2 hours to allow the seal at the bottom of the die to release vapours as it cures. The die is then cooled back to room temperature. The inner surface of the die is sprayed with mold release to avoid its direct contact with molten aluminum. This is followed by placing aluminum foils and carbon fiber fabric discs in the die in an alternate configuration as illustrated in Figure 3-7. The laminate configuration is symmetric for all fabricated composite thicknesses with the fiber fabric layers placed closer to top and bottom surfaces, while the area close to the neutral bend axis is practically fiber free. The objective of this laminate configuration is to optimise the efficiency of carbon fiber reinforcement and to improve the bend performance of the composite samples.

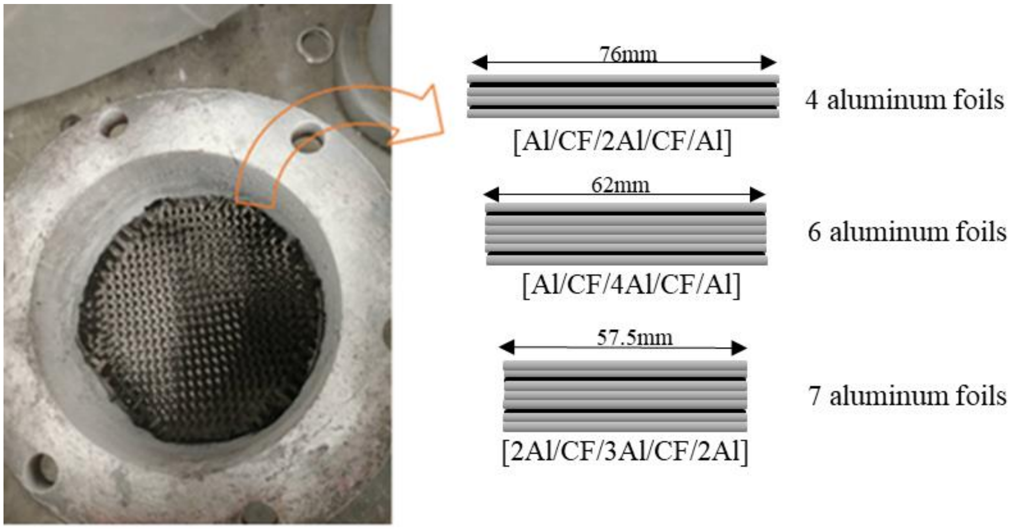

Figure 3-7: Laminate aluminum-carbon fiber configurations for different composite thicknesses

The last step is placing the steel sheet on top of the laminate configuration, applying the seal, placing the top punch, closing the die using the top cover, and performing a second curing step for the top seal of the die set-tp. To avoid squeezing the seal material out or into the composite layers, the screws are only loosely tightened prior to both curing steps followed by stronger tightening of the screws after curing when the seal is solid.

3.2.3 Squeeze casting process

For casting, a LINDBERG air furnace (see Figure 3-8) is preheated to the target temperature at 800°C. The sealed die is placed at the center of the furnace and maintained for durations of up to 40 mins. The variation in holding time allowed to investigate the effect of temperature homogenisation and molten aluminum-carbon fiber contact time. In this step, the squeeze pressure is provided solely by the differential in thermal expansions between the die components. This pressure accelerates the flow of aluminum as it melts and enables rapid fiber infiltration as the viscosity of molten aluminum decreases during heating.

Figure 3-8: LINDBERG furnace used for heating

At the end of the holding time at high temperature, the die is removed from the furnace and placed in a KDS50-RODGERS hydraulic press for external compression. This allowed to maintain the squeeze pressure by compensating for the thermal expansion pressure drop as the die components contract and molten aluminum shrinks during cooling and solidification. Figure 3-9 shows the die set-up in the hydraulic press during cooling. Three levels of hydraulic pressure, 90 MPa, 40 MPa and 20 MPa, were investigated. During cooling and hydraulic pressing, the displacement of the top die cover is controlled to maintain the desired composite thickness.

Figure 3-9: Pressure application on the die set-up using a hydraulic press during cooling

After the die has completely cooled to room temperature, it is opened by removing top and bottom covers, and the composite samples are pressed out using the same hydraulic press. Finally, the oxidation film on the sample surface is removed using sandpapers.

3.3 Mechanical testing

Piston-on-ring (POR) biaxial flexural tests are selected to assess the composite bend performance. The test set-up is according to the ISO 6872 standard [46]. The composite edges are smoothened to make sure the bend loading is uniform and to prevent the composite from moving during the bending test. The sample dimeter-to-thickness ratio ranges from 8.5 to 16 and the effect of overhanging annulus outside the support ring has been considered. The selection of the specimen and base ring radii is based on the Equation (3-8). The given range between 1 and 6 ensures that the set-up dimensions, including the disc sample overhang, yield accurate testing results by limiting stress concentrations at the sample edge where crack and fracture tend to initiate.

$$1 \leq \frac{r_3 - r_2}{\mathrm{t}} \leq 6 \tag{3-8}$$

Where r_2 *and* r_3 are the radii of base ring and specimen, respectively.

Testing is performed using a 4482 Instron universal test frame. The bending load and the sample deflection are measured using a 1000 kN load cell and the crosshead displacement of the frame, respectively. The crosshead speed is 10 mm/min and the deflections are measured up to 10 mm. The dowel pin had a 15.7mm diameter, while the support ring had a thickness of 10cm and an inner diameter of 6.35cm. A PEEE film was placed on both contact surfaces between composite samples and the pin as well as between composite samples and the support ring. The film allows to reduce the effects of frictions. The tests are stopped when the deflection reaches 10mm, or samples fail by either fracture of delamination. The bend test set-up is shown in Figure 3-10. The failed samples were then visually investigated with respect to the mode of failure, the fiber-matrix interface behaviour and potential fiber pull-out.

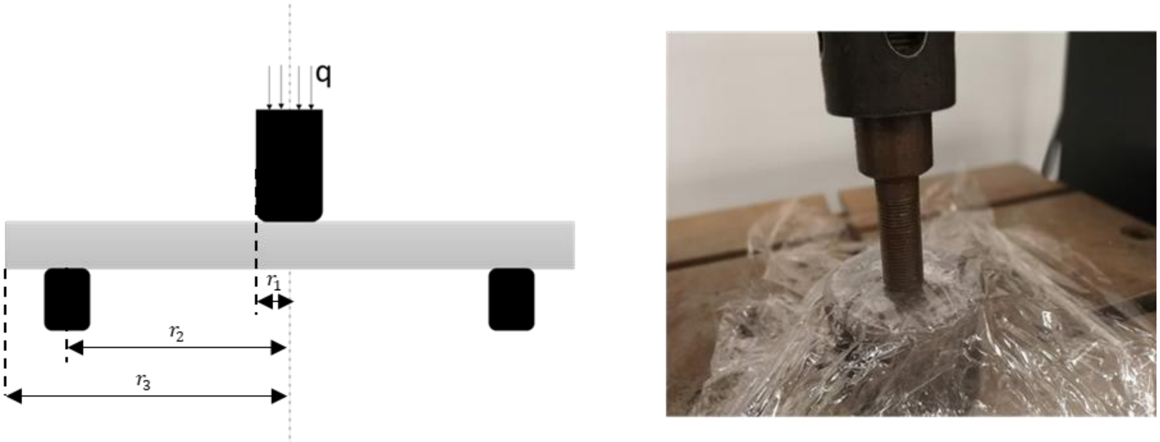

Figure 3-10: Test set-up for piston-on-ring (POR) bending tests

The biaxial bend tests are evaluated as bending of axisymmetric thin plates, which is based on the Kirchhoff assumptions. In this case, the thickness change is neglected and the stress in the thickness direction is assumed to have no effect on in-plane deformations. As shown in the plane body diagram in Figure 3-11, the stress becomes zero at the neutral midplane. For beam bending, the relation between deflection and applied force is described using the following Equation (3-9) and (3-10).

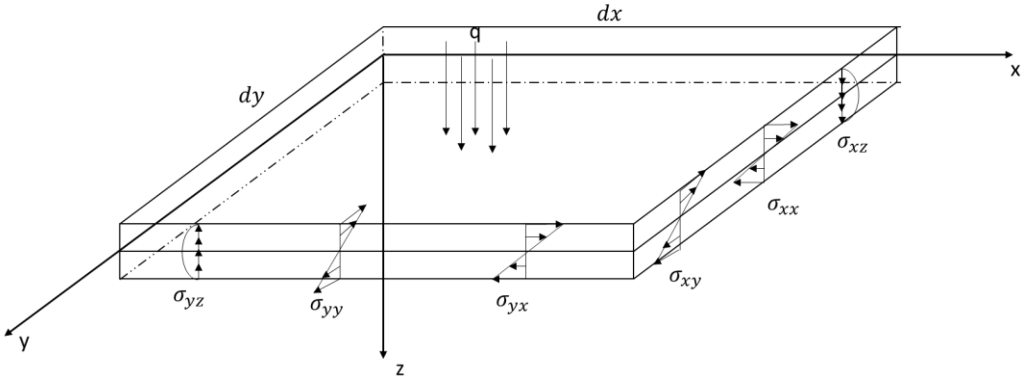

Figure 3-11: Plane body diagram based on Kirchhoff assumptions

$$\mathrm{D}\nabla^4\omega = q \tag{3-9}$$

$$\mathrm{D} = \frac{Et^3}{12(1-v^2)} \tag{3-10}$$

Where D is the bending rigidity of the thin plate; $\nabla^4\omega$ is the Fourth-order differential of plate deflection; q is the transverse load; E is the young's modulus; t is the plane thickness and v is the Poisson's ratio.

For a polar coordinate system, the expression of deflections includes a radial distance from the central axis (ρ) and an angle (φ). If the structure is symmetric along the z axis, the deflection will only depend on the radial distance. By solving the equation, the bending moment and stress at plane elements can be revealed by using Equation (3-11):

$$\mathrm{D}\left(\frac{d^2}{d\rho^2}+\frac{1}{\rho}\frac{d}{d\rho}\right)\left(\frac{d^2\varphi}{d\rho^2}+\frac{1}{\rho}\frac{d\varphi}{d\rho}\right)=q \tag{3-11}$$

The loading at the piston is assumed uniformly distributed at the contact surface with the bend samples. According to the ISO 6872 standard, the biaxial flexural strength is calculated using Equation (3-12) [46].

$$\sigma_{por}=-0.2387P(X-Y)/t^2 \tag{3-12}$$

Where:

$$\mathrm{X}=(1+v)\ln\left(\frac{r_1}{r_3}\right)^2+[(1-v)/2]\left(\frac{r_1}{r_3}\right)^2 \tag{3-13}$$

$$\mathrm{Y}=(1+v)\left[1+\ln\left(\frac{r_2}{r_3}\right)^2\right]+(1-v)\left(\frac{r_2}{r_3}\right)^2 \tag{3-14}$$

σ_{por} is the piston-on-ring (POR) maximum bending stress; P is the testing loading; t is the specimen thickness; v is the Poisson's ratio; $r_1, r_2\ and\ r_3$ are the radii of loading pin, base ring and specimen, respectively. All units are in millimetres.

The moment-load equation of POR is given by

$$\mathrm{M}_{por}=\frac{-P}{8\pi}\left\{(1+v)(1+2\ln(\frac{r_2}{r_1})^2)+(1-v)[1-\frac{{r_1}^2}{2{r_2}^2}]\frac{{r_2}^2}{{r_3}^2}\right\}\ (\text{for r} \le r_2) \tag{3-15}$$

Where M_{por} is the POR bending moment.

3.4 Stress-deflection behavior analysis

No appropriate equations could be found in existing literature for equi-biaxial Piston-On-Ring (POR) testing as used in this study. Therefore, the stress-deflection behavior is initially assumed to obey the linear elastic theory and to be identical to that from Ring-On-Ring (ROR) bend test according to the relationships [47]:

$$\mathrm{u}_{ror} = \frac{3P\left(1-v^2\right)}{2\pi E t^3}(r_2^2 + \frac{r_2^2(1-v)\left(r_2^2-r_1^2\right)}{2(1+v^2)r_3^2} - r_1^2(1 + \ln(\frac{r_2}{r_1}))) \tag{3-16}$$

And

$$\sigma_{ror} = \frac{3P(1+v)}{2\pi t^2}\{\ln\left(\frac{r_2}{r_1}\right) + \frac{(1-v)\left(r_2^2-r_1^2\right)}{2(1+v)r_3^2}\}(\text{for r} \le r_2) \tag{3-17}$$

Where u_{ror} is the mid-span deflection; E is the elastic modulus; and σ_{ror} is the flexural strength of the sample under ROR testing.

Comparing the results from Equations (3-16) and (3-17) to experimental values, a correction factor f is applied to better describe the flexural strength σ_{por} under POR loading:

$$\mathrm{f} = \frac{\sigma_{por}}{\sigma_{ror}} \tag{3-18}$$

In this case:

$$\mathrm{u}_{por} = \mathrm{f} \cdot \mathrm{u}_{ror} \tag{3-19}$$

Table 3-6 shows the test parameters for the POR bend behavior calculations.

Table 3-6: Parameters applied in POR test calculations

r_1(mm)	r_2(mm)	f	v
15.7	31.75	1.4791	0.33

4 EXPERIMENAL RESULTS

4.1 Squeeze casting pressure

The calculated thermal expansion squeeze pressures for the short and long die designs with 4mm thick composite samples at different temperatures are shown in Table 4-1. As can be seen, in addition to the higher achievable squeeze pressure, the long die allows maintaining a higher residual squeeze pressure upon composite sample solidification and cooling down to 540°C, which can be crucial for composite sample integrity, defect density, properties and performance.

Table 4-1: Thermal expansion pressure with different dies and squeeze temperatures

Design	540°C	700°C	820°C
Short die	15.55 MPa	118.4 MPa	124.3 MPa
Long die	40.09 MPa	128.9 MPa	141.1 MPa

The thermal expansion pressure applied on the composite samples can be expected to dramatically drop during cooling as the die set-up components contract and molten aluminum shrinks upon solidification. Therefore, external post-processing pressure is applied using a hydraulic press in the final squeeze casting tests to maintain sufficient squeeze pressure during cooling and solidification.

4.2 Sample configuration

The sample in the as-cast state (a) and after cleaning (b) is shown in Figure 4-1. Cleaning is performed using ultrasonic cleaning and grinding to remove the oxide layer and remnants of the seal material from the sample surface. The total reinforcement volume fraction is calculated using Equation (4-1).

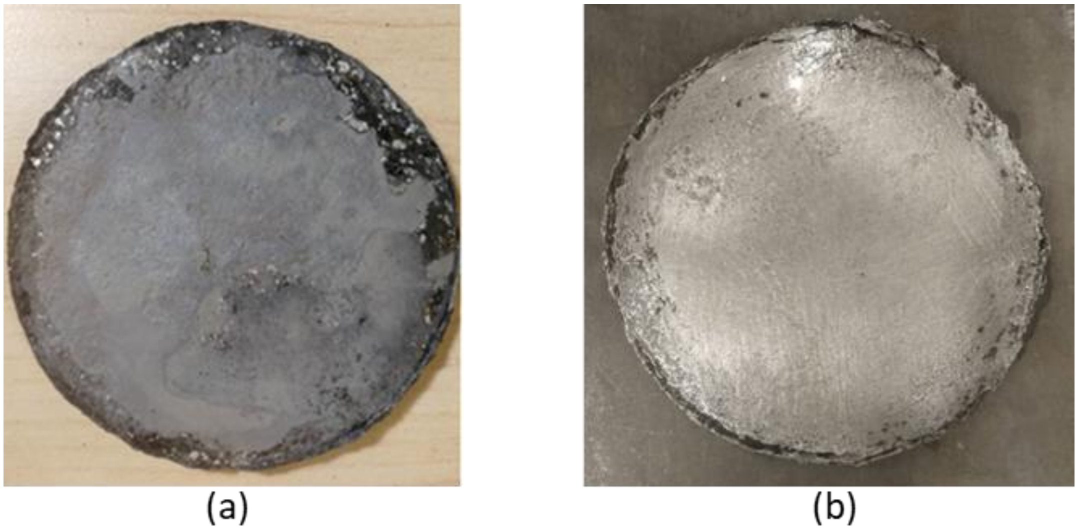
(a) (b)

Figure 4-1: (a) As-cast composite sample and (b) after surface cleaning

$$V_{f(\%)} = \left[\frac{w_f}{\rho_f A_C t}\right] \times 100 \tag{4-1}$$

where V_f is the carbon fiber volume fraction; w_f and ρ_f are the carbon fiber total weight and density, respectively; A_C and t are the specimen area and thickness, respectively.

The first sample group is manufactured using the short casting die as specified in Table 4-2. All samples are fabricated with 4 Aluminum sheet layers. The squeeze cast temperature is 800°C and the temperature holding time prior to pressurising is 40 mins. The samples were cooled in air and no post-processing was performed. Using idealised thermal expansion with no frictions and no compaction, the short casting die was estimated to provide a thermal expansion pressure of 124.3 MPa at the casting temperature. Samples were fabricated with different fiber volume fractions (V_f). The thickness and diameter of the composite samples are measured using a Vernier caliper, and average values are computed from measurements at three different locations.

Table 4-2: Specificities of fabricated samples using the short casting die

Process group	Sample Ref.	Averaged t (mm)	Averaged total V_f (vol%)	Specificities
G1	S1	4.58	2.08	50% of fiber yarns removed, 4 aluminum foils with 76mm ϕ, and 2 carbon fiber fabric layers, ceramic seal used
	S2	4.78	3.08	25% of fiber yarns removed, 4 aluminum foils with 76mm ϕ, and 2 carbon fiber fabric layers, ceramic seal used
	S3	4.54	4.55	Original fabric, 4 aluminum foils with 76mm ϕ, and 2 carbon fiber fabric layers, ceramic seal used

The second and third groups of samples are fabricated using the same processing parameters as for the first group but using a longer casting die. Again, assuming ideal thermal expansion with no frictions and no compaction, a higher thermal expansion squeeze pressure of 141.1 MPa is predicted for this longer die. The specifics of the obtained composite samples are summarised in Table 4-3. In order to improve interface bonding, aluminum sheet layers with varying diameters of 57.5mm, 62.0mm and 76.0mm, respectively are used. The smaller diameter sheets were expected to deform plastically in the radial direction to help break the surface oxide scale to promote the flow of molten aluminum, and improve carbon fiber layer infiltration, wetting and interface bonding.

Table 4-3: Specificities of fabricated samples using the long casting die

Process group	Sample Ref.	Averaged t (mm)	Averaged total V_f (vol%)	Specificities
G2	S4	6.35	2.43	50% of fiber yarns removed, 6 aluminum foils with 62.0mm ϕ, and 2 carbon fiber fabric layers, ceramic seal used
	S5	6.10	3.70	25% of fiber yarns removed, 6 aluminum foils with 62.0mm ϕ, and 2 carbon fiber fabric layers, ceramic seal used
	S6	6.22	2.34	50% of fiber yarns removed, 7 aluminum foils with 57.5mm ϕ, and 2 carbon fiber fabric layers, ceramic seal used
	S7	7.04	2.79	25% of fiber yarns removed, 7 aluminum foils with 57.5mm ϕ, and 2 carbon fiber fabric layers, ceramic seal used
	S8	7.30	3.71	Original fiber fabric, 7 aluminum foils with 57.5mm ϕ, and 2 carbon fiber fabric layers, ceramic seal used

Copper and brass foils are investigated as alternative to the ceramic seal. The resulting samples are shown in Figure 4-2. Both copper and brass proved to strongly react with the aluminum sheets leading to their complete dissolution in the Aluminum layers. The dissolution produces brittle aluminides and the lack of bonding between aluminum and fiber fabric layers.

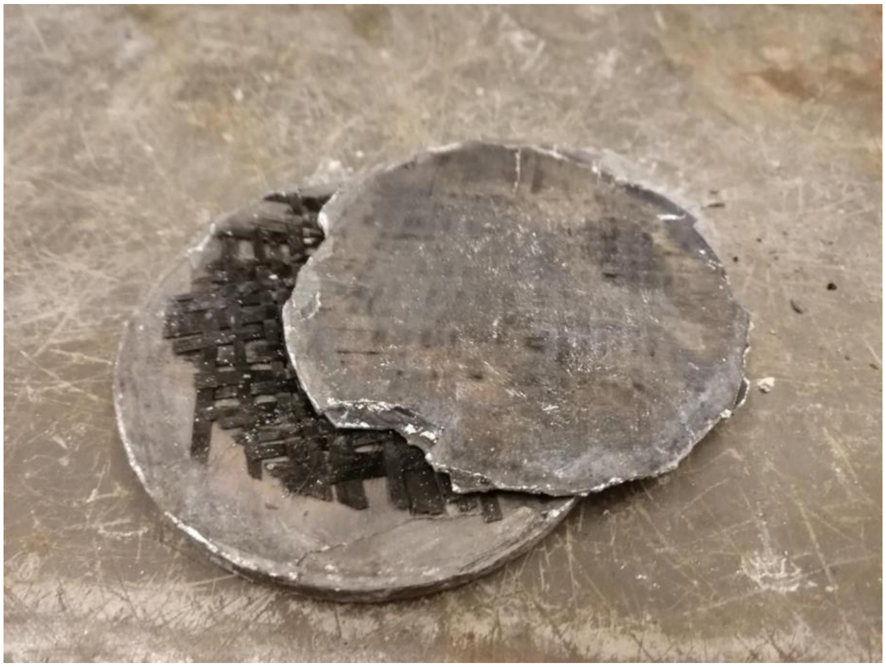

Figure 4-2: Brittleness and lack of aluminum-fiber bonding in samples fabricated using Copper and Brass foils as seal.

The third group of samples are fabricated using a combination of the long casting die and hydraulic post-processing pressure at the peak temperature and during cooling. For this set, the composites are heated to 800℃, maintained for 40 mins and then post-pressurising is applied during cooling to room temperature. Sample S9 fabricated by hydraulic pressure of 90 MPa produced bad quality samples where the carbon fibers decomposed and strongly reacted to form hard graphite or carbide particles as shown in Figure 4-3. A lower post-processing pressure of 40 MPa produced good quality samples that are presented in Table 4-4. Appropriate sealing was found to be crucial for fabrication. Seal failure and leakage of molten aluminum at high temperature and pressure led to bad quality samples featuring incomplete infiltration, porosity, or lack of matrix fiber adhesion. Using a lower post-processing pressure of 20 MPa and the long die also produced good quality samples while significantly reducing the risk of seal failure and leakage of molten aluminum; specificities of the produced group 4 samples are shown in Table 4-5.

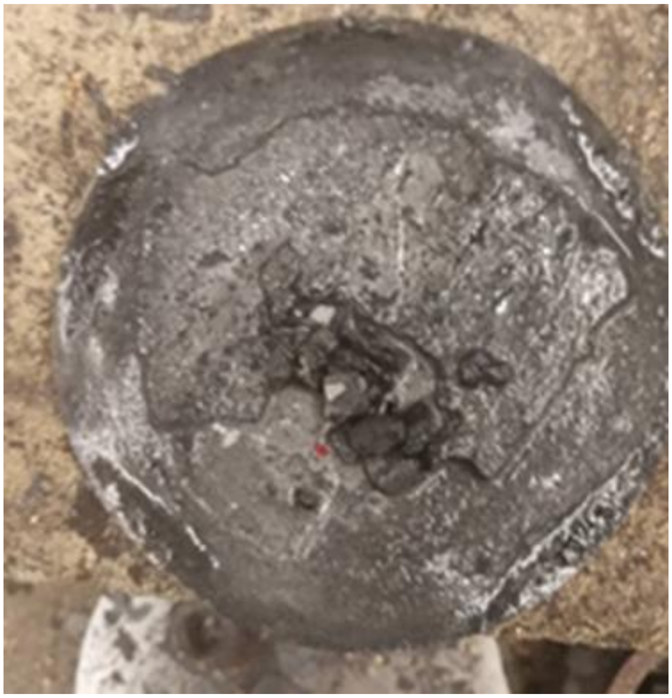

Figure 4-3: High hydraulic pressure of 90 MPa caused the decomposition of carbon fiber and their reaction into graphite or carbide particles.

Table 4-4: Specificities of samples fabricated using the long die and 40 MPa hydraulic pressure at peak temperature and during cooling

Process group	Sample Ref.	Averaged t (mm)	Averaged total V_f (vol%)	Specificities
G3	S10	4.0	1.39	50% of fiber yarns removed, 4 aluminum foils with 76mm ϕ, and 2 carbon fiber fabric layers, ceramic seal used
	S11	4.1	3.55	25% of fiber yarns removed, 4 aluminum foils with 76mm ϕ, and 2 carbon fiber fabric layers, ceramic seal used
	S12	3.8	4.81	Original fiber fabric, 4 aluminum foils with 76mm ϕ, and 2 carbon fiber fabric layers, ceramic seal used

Table 4-5: Specificities of samples fabricated using the long die and 20 MPa hydraulic pressure at peak temperature and during cooling

Process group	Sample Ref.	Averaged t (mm)	Averaged total V_f (vol%)	Specificities
G4	S13	3.8	2.17	50% of fiber yarns removed, 4 aluminum foils with 76mm ϕ, and 2 carbon fiber fabric layers, ceramic seal used
	S14	4.2	3.37	25% of fiber yarns removed, 4 aluminum foils with 76mm ϕ, and 2 carbon fiber fabric layers, ceramic seal used
	S15	4.28	4.42	Original fiber fabric, 4 aluminum foils with 76mm ϕ, and 2 carbon fiber fabric layers, ceramic seal used

As reference, aluminum samples without carbon fiber reinforcement are also fabricated using identical conditions as listed in Table 4-6. The different thicknesses are achieved using different numbers of aluminum sheets for squeeze casting. The Aluminum samples are fabricated using the long casting die at 800℃ with 40 mins holding time. No additional hydraulic pressure is applied, and the samples are cooled in air.

Table 4-6: Specificities of unreinforced Aluminum control group samples

Process group	Sample Ref.	Averaged t (mm)	Averaged total V_f (vol%)	Specificities
C	A1	3.75	0	76mm aluminum sheets
	A2	4.8	0	
	A3	6.8	0	

4.3 Piston-on-ring bend resistance

The bend test results are used to calculate stress-strain curves by substituting load and displacement data into Equations (3-12) and (3-19). The elastic flexural modulus is estimated by taking the linear part from the beginning of the curve. Furthermore, as the yield point is hard to be defined based on the stress-stain curve, the offset yield stress with 0.2% plastic strain is applied to determine the yield strength. The POR flexural modulus and yield strength of S1 are found as 31.34 GPa and 74.70 MPa, respectively. Beyond the yield stress, the sample starts to deform plastically. The linear strain hardening modulus is calculated by the slope between the yield strength and the ultimate strength as illustrated in Figure 4-4 for the S1 sample.

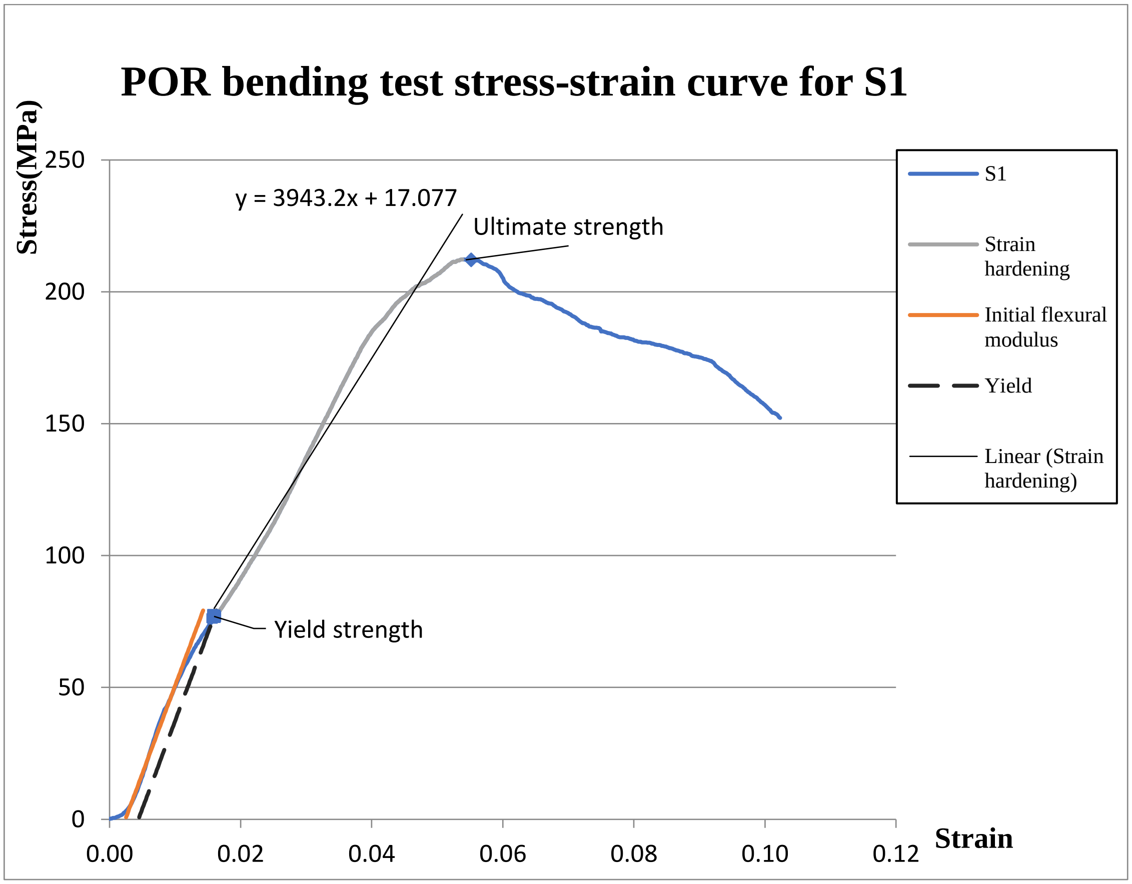

Figure 4-4: POR bending test stress-strain curve for S1

All experimental results are calibrated over the control group (C) with unreinforced standard T4 6061 aluminum properties as shown in Table 4-7. The T4 heat treatment was chosen as the most appropriated reference state because no artificial aging was performed, and the samples were tested a few days after casting. The strain hardening modulus uses the same calibration factor with the flexural modulus. Comparing the different manufacturing process parameters, Process groups G1 and G2 samples fabricated without additional hydraulic pressure yielded poor flexural properties below unreinforced Aluminum. The addition of hydraulic post-processing pressure increases both the flexural modulus and the bend strength compared to unreinforced Aluminum and composite samples without additional pressure. G3 samples made using the long die and the average hydraulic post-processing pressure of 40 MPa exhibit the highest and most repeatable flexural properties. S12 improved flexural modulus, strain hardening modulus and flexural yield strength by 11.6%, 248.3% and 90.1% compared to unreinforced Aluminum, respectively. Meanwhile, S11 has the highest flexural strength improved by 179.7% compared with unreinforced Aluminum. 20 MPa and 40 MPa post-processing pressures produce similar flexural modulus levels. For G3 and G4, the flexural modulus and yield strength continuously increase with increasing carbon fiber volume fraction, while the bend strength tends to increase and then decrease with increasing carbon fiber volume fraction. S15 shows the most desirable properties in G4, which the flexural modulus and yield strength increasing by 13.0% and 55.0%, respectively. However, the strain hardening modulus of S15 decreased 9.37% than control group.

Table 4-7: Flexural modulus and Flexural strength results for all composite samples and unreinforced Aluminum control group

Process group	Sample Ref.	Flexural modulus (GPa)	Flexural yield strength (MPa)	Strain Hardening Modulus (GPa)	Flexural Strength (MPa)
G1	S1	31.34	74.70	18.37	213.5
	S2	63.17	144.5	8.182	240.7
	S3	41.12	106.1	9.564	198.7
G2	S4	41.18	107.3	5.253	158.3
	S5	56.31	151.8	15.34	230.0
	S6	61.29	114.3	3.252	155.5
	S7	60.92	133.3	12.09	221.3
	S8	50.01	132.9	7.543	171.3
G3	S10	70.93	169.6	18.68	495.6
	S11	73.80	178.0	42.27	830.9
	S12	77.04	204.0	51.65	643.1
G4	S13	68.01	87.60	19.64	253.6
	S14	69.09	125.9	24.29	284.2
	S15	78.54	166.8	13.44	205.0
C	A1-A3	69.00	107.3	14.83	248.9

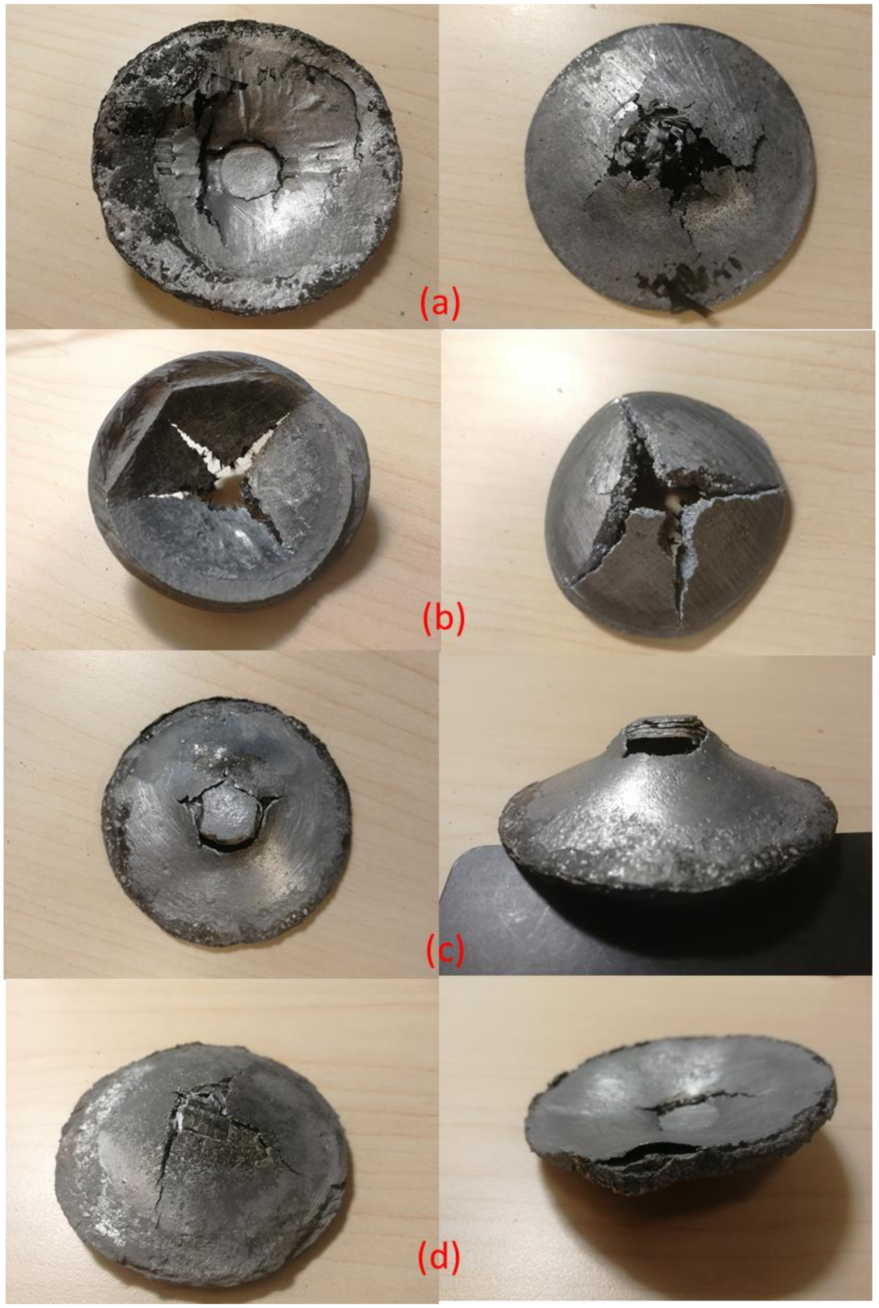

Figure 4-5: Fracture modes of composite samples after piston-on-ring bend tests: (a) S_3; (b) S_6; (c) S_{12}; (d) S_{13}

Figure 4-5 shows failed samples S3, S6, S12 and S13. S3 shows fiber pull-out with visible delamination due to weak interface bonding as shown in Figure 4-5 (a). As can be seen in Figure 4-5 (b), fiber pull-out is much less in S6. However, the arching in sample S6 is stronger as a result of large shear displacements between the carbon fiber and matrix layers during bend testing. Meanwhile, a significant carbon fiber fabric displacement to the top surface during squeeze casting is found in S6. Figure 4-5 (c) shows that S12 exhibits excellent carbon fiber-aluminum matrix interface bonding without any fiber pull-out at the fracture surface. Similar failure interfaces are found in S10 and S11 samples. Moreover, in contrast to all other composite groups and unreinforced aluminum control group, the crack propagation in G3 (includes S10, S11 and S12) is only circumferential following the transversal shear stress at the external contour of the loading piston. No damage is seen at the center and no radial cracks are observed. As seen in Figure 4-5 (d), S13 shows composite fracture without any visible pull-out, but radial cracks are found at the top and bottom surfaces.

The stress-strain curves of G3 and control group (C) are shown in Figure 4-6. As expected, a good fiber-matrix interface bond drastically improves the strength of the composites while increase the strain hardening modulus as compared to unreinforced aluminum. Hence, carbon fiber primarily controls the composite performance after the aluminum matrix starts to plastically deform.

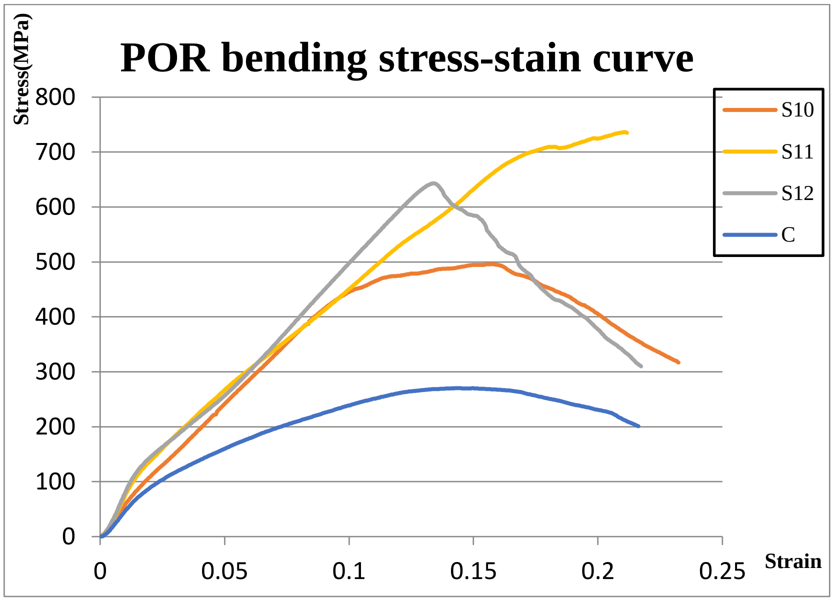

Figure 4-6: Stress-stain curves for S10-S12 and unreinforced Al samples

5 MODELLING

5.1 Composite structure model

The fabric pattern unit formed by interlacing warp and weft yarns with 1:1 ratio is well-known as plain weave as seen in Figure 5-1 (a). The cross-sectional shape of yarns is defined by the intersection of two identical circles as shown in Figure 5-1 (b). The input parameters are directly measured from carbon fiber fabric and adjusted to satisfy the geometry model. In this modelling, the geometric parameters are given in Table 5-1.

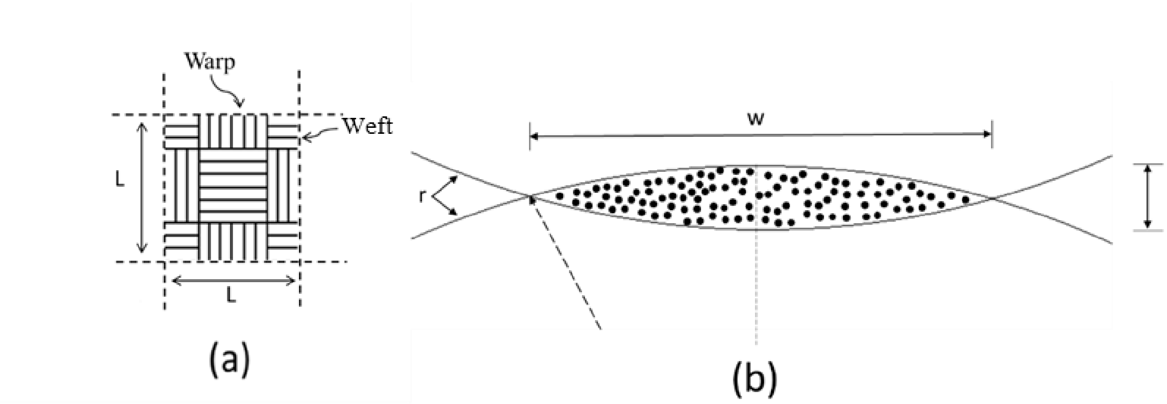

Figure 5-1: The geometrical modelling of plain weave fabric: (a) fabric planar structure; (b) yarn cross section

Table 5-1: Carbon fiber yarn geometric parameters

Unit lenth (L)	Yarn thickness (t)	Yarn width (w)	Radius (r)
6.2mm	0.17mm	3.10mm	14.17mm

The modelling geometry changes with the fabric yarn density. The original plain-weave carbon fiber fabric is show in Figure 5-2 (a). Different carbon fiber volume fractions are achieved by removing warp and weft yarns at the edges of the fabric, and then spreading the remaining yarns to create interspacing of ½ and 1 yarn width between the yarns to reduce the carbon fiber density by 25% and 50%, respectively. As such, three fiber concentrations are modelled in this research: (1) the original plain weave carbon fiber fabric; (2) the plain weave fabric after 25% reduction in fiber density; and (3) the plain weave fabric after 50% reduction in fiber density. The fabric geometry models after spreading of the yarns to reduce the fiber density is exemplarily illustrated in Figure 5-2 (b).

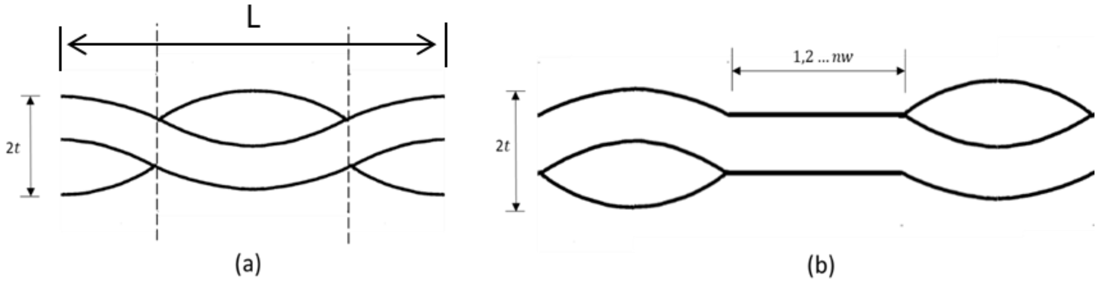

Figure 5-2: Fabric yarn geometry modelling: (a) original fabric; (b) after removal and spreading of yarns

Within the plain weave carbon fiber reinforced layers (CF), there is a relatively high carbon fiber volume fraction in the yarn bundles. Thus, we assume the mechanical properties of each yarn in the composite are equal to those of pure carbon fiber. In this case, the effective fiber volume fraction (V_{rl}) in the reinforced layers is approximate by the sum of the volume of the carbon fiber tows in pattern unit divided by the total unit volume as written in Equation (5-1).

$$\boldsymbol{V_{rl}} = \frac{\boldsymbol{Yarn\,Volume}}{\boldsymbol{Unit\,Volume}} \tag{5-1}$$

The samples are assumed to have a 4mm total thickness (t_s) and Figure 5-3 shows the material constitutions along the composite disk axis. The sample includes pure aluminum layers and carbon fiber reinforced layers. The thickness of the carbon fiber reinforced layers is 0.36mm and the position of each layer is followed in the experiment configuration as illustrated in Figure 5-3.

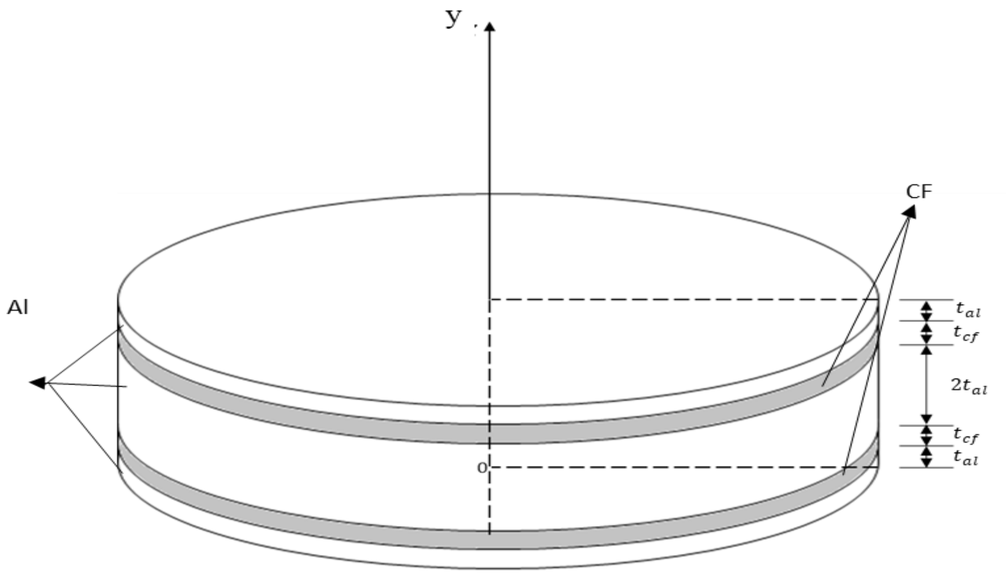

Figure 5-3: Material arrangement along the composite disk axis

The yarn packing fraction(κ) is introduced to predict the overall carbon fiber volume fraction. As seen in Figure 5-1 (a) and Figure 5-3, the carbon fiber volume fraction of composites can be calculated by Equation (5-2):

$$V_f = \frac{2t_{cf}}{t_s} V_{rl} \kappa \tag{5-2}$$

Where V_f is the overall carbon fiber volume fraction in the composite; t_{cf} and t_s are the carbon fiber reinforced layer and total sample thickness, respectively; V_{rl} is the effective carbon fiber volume fraction in the carbon fiber reinforced layer; κ is the yarn packing fraction.

The value of the yarn packing fraction (κ) is related to the space between each fiber and the applied force in the composite [48]. In this study, the yarn packing fraction (κ) is considered as 0.43 which is the ratio of experimental/predicted original plain weave carbon fiber fabric volume. The calculated carbon fiber volume fractions with different fabric density are summarised in Table 5-2. The overall carbon fiber volume fraction is applicable for both the analytical model (ANA) and the FEA models.

Table 5-2: Carbon fiber volume fraction for different fabric densities

Plain woven fabric density	Yarn-to-yarn distance (mm)	V_{rl} [vol%]	V_f [vol%]
Original	0	63.13	4.89
25 percent removed	1.55	42.06	3.26
50 percent removed	3.1	31.53	2.44

5.2 Analytical model (ANA)

5.2.1 Effective elastic stiffness

In the present analytical model (ANA), carbon fibers are assumed uniformly distributed in a layer with a specific thickness as illustrated in Figure 5-4 (b), without considering the pattern described above in Figure 5-2 and Figure 5-4 (a). The composite structure is then considered as a sandwich material composed of these carbon fiber reinforced layers (CF) and unreinforced aluminum layers in an alternating configuration as illustrated in Figure 5-3. Moreover, an equal number of fibers are assumed in the two orthogonal directions (y and z).

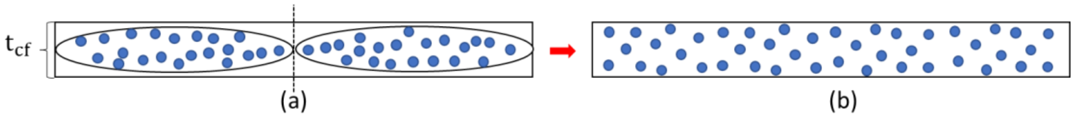

Figure 5-4: Uniform distribution assumption for ANA modelling

Considering the sample bottom surface is at the origin of the y axis (y = 0) as seen in Figure 5-3, the location of each layer along the y-axis is given as in Equation (5-3):

$$h_i = \sum_1^i t_i \; (0 \leq i \leq 5) \tag{5-3}$$

Where i is the layer number (total of 5 layers in this study); h_i is the location of the ith layer, with $\mathrm{h}_0 = 0$ and $\mathrm{h}_5 = 4mm$; $\mathrm{t_i}$ is the thickness of each individual layer ($\mathrm{t}_1 = \mathrm{t_{al}}$; $\mathrm{t}_2 = \mathrm{t_{cf}}$ and $\mathrm{t}_3 = 2\mathrm{t}_{al}$); $\mathrm{t_{al}} = 0.82mm$ and $\mathrm{t_{cf}} = 0.36mm$ are the thicknesses of unreinforced aluminum layer and carbon fiber reinforced layer, respectively.

The unidirectional fiber composite is further assumed as transversely isotropic, which means the properties are uniform in the y-z plane as illustrated in Figure 5-5. In this case, the Hooke's Law stiffness is characterized by five independent constants, where the stress-strain relation can be expressed as in Equation (5-4) and Equation (5-5).

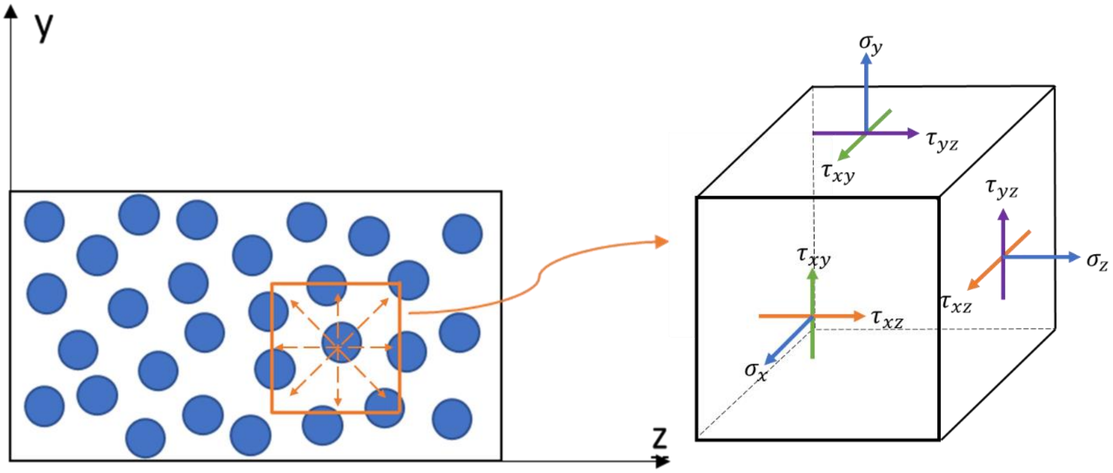

Figure 5-5: Transversely isotropic fiber composite

$$[\sigma] = [\mathrm{C}][\varepsilon] \tag{5-4}$$

with

$$[\mathrm{C}] = \begin{bmatrix} C_{11} & C_{12} & C_{12} & 0 & 0 & 0 \\ C_{12} & C_{22} & C_{23} & 0 & 0 & 0 \\ C_{12} & C_{23} & C_{22} & 0 & 0 & 0 \\ 0 & 0 & 0 & \frac{C_{22}-C_{23}}{2} & 0 & 0 \\ 0 & 0 & 0 & 0 & C_{55} & 0 \\ 0 & 0 & 0 & 0 & 0 & C_{55} \end{bmatrix} \tag{5-5}$$

$$[\sigma]^T = \left[\sigma_{xx}, \sigma_{yy}, \sigma_{zz}, \tau_{yz}, \tau_{xz}, \tau_{xy}\right] \equiv [\sigma_1, \sigma_2, \sigma_3, \sigma_4, \sigma_5, \sigma_6] \tag{5-6}$$

$$[\varepsilon]^T = \left[\varepsilon_{xx}, \varepsilon_{yy}, \varepsilon_{zz}, \gamma_{yz}, \gamma_{xz}, \gamma_{xy}\right] \equiv [\varepsilon_1, \varepsilon_2, \varepsilon_3, \varepsilon_4, \varepsilon_5, \varepsilon_6] \tag{5-7}$$

Where [C] is the stiffness tensor; [σ] and $[\varepsilon]$ are stress and strain tensors expressed in the Voigt notation; $\gamma_{yz}, \gamma_{xz}, \gamma_{xy}$ are the engineering shear strains.

By inversing Equation (5-4), the elastic properties can be substitute into the compliance matrix as follows:

$$[\varepsilon] = [S][\sigma] \tag{5-8}$$

$$[\mathrm{S}] = [\mathrm{C}]^{-1} \tag{5-9}$$

$$\begin{bmatrix} \varepsilon_{xx} \\ \varepsilon_{yy} \\ \varepsilon_{zz} \\ \gamma_{yz} \\ \gamma_{xz} \\ \gamma_{xy} \end{bmatrix} = \begin{bmatrix} \frac{1}{E_x} & -\frac{v_{zx}}{E_z} & -\frac{v_{zx}}{E_z} & 0 & 0 & 0 \\ -\frac{v_{xz}}{E_x} & \frac{1}{E_z} & -\frac{v_{yz}}{E_z} & 0 & 0 & 0 \\ -\frac{v_{xz}}{E_x} & -\frac{v_{yz}}{E_z} & \frac{1}{E_z} & 0 & 0 & 0 \\ 0 & 0 & 0 & \frac{2(1+v_{yz})}{E_z} & 0 & 0 \\ 0 & 0 & 0 & 0 & \frac{1}{G_{xz}} & 0 \\ 0 & 0 & 0 & 0 & 0 & \frac{1}{G_{xz}} \end{bmatrix} \begin{bmatrix} \sigma_{xx} \\ \sigma_{yy} \\ \sigma_{zz} \\ \tau_{yz} \\ \tau_{xz} \\ \tau_{xy} \end{bmatrix} \tag{5-10}$$

Where [S] is the compliance tensor; E_{i} is the young's modulus along the i axis; v_{ij} is the i-j plane Poisson's ratio (where the length increases in the i axis); and G_{ij} is the shear modulus in the i-j plane. The values of all elastic constants are estimated according to the rule of mixture.

Further, the carbon fiber layer is taken as a thin ply in the composite and the ANA model assumes plane stress conditions. As a result, the stress tensor along the sample thickness can be neglected and the stress-stain relation is further reduced to:

$$\sigma_{yy} = \sigma_{yz} = \sigma_{xy} = 0 \tag{5-11}$$

$$\begin{bmatrix} \varepsilon_{xx} \\ \varepsilon_{zz} \\ \gamma_{xz} \end{bmatrix} = \begin{vmatrix} \frac{1}{E_x} & -\frac{v_{zx}}{E_z} & 0 \\ -\frac{v_{xz}}{E_z} & \frac{1}{E_z} & 0 \\ 0 & 0 & \frac{1}{G_{xz}} \end{vmatrix} \begin{bmatrix} \sigma_{xx} \\ \sigma_{zz} \\ \sigma_{xz} \end{bmatrix} \tag{5-12}$$

Where E_x and E_z are the longitudinal and transverse young's moduli; v_{xz} and v_{zx} are the major and minor Poisson's ratio, with $\frac{v_{xz}}{E_L} = \frac{v_{zx}}{E_T}$; and G_{xz} is the in-plane shear modulus. The values of all elastic constants are also estimated according to the rule of mixture.

The rule of mixture (ROM) is widely used to predict the mechanical properties such as stiffness, Poisson's ratio and strength of laminated long reinforcement composites as shown in Figure 5-6. The basic assumptions of the phenomenological ROM equations are [49]:

(1) Unidirectional composites consisting of homogenous, linear elastic matrix and isotropic or anisotropic reinforcement phase.

(2) Reinforcement is uniformly distributed in the matrix. Composites are homogenous and linear elastic in each laminate.

(3) The microstructure and interface bonding are ideal and continuous. Voids and defects are not included.

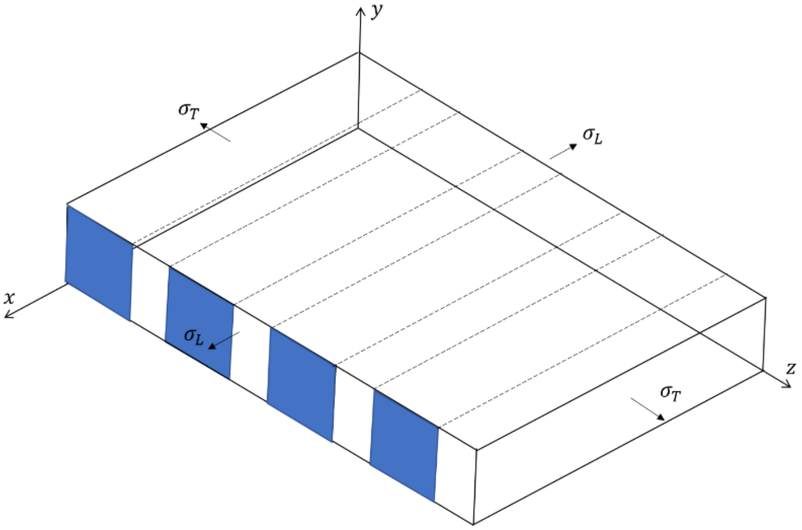

Figure 5-6: Unidirectional fiber reinforced composite assumption for ROM

The modulus of elasticity has two different ROM equations as seen in Equation (5-13) to Equation (5-17). Equation (5-13) is the Voigt model that describes the longitudinal performance with uniform stain in the composite volume. Equation (5-15) is the Reuss model that assumes uniform stress in the composite under loading in the transverse direction [50].

$$E_L = V_f \cdot E_f + \left(1 - V_f\right) \cdot E_m \tag{5-13}$$

$$v_L = V_f \cdot v_f + (1 - V_f) \cdot v_m \tag{5-14}$$

$$E_T = \left(\frac{V_f}{E_f} + \frac{1-V_f}{E_m}\right)^{-1} \tag{5-15}$$

$$G_c = \left(\frac{V_f}{G_f} + \frac{1-V_f}{G_m}\right)^{-1} \tag{5-16}$$

$$v_T = \frac{E_T}{E_L} \cdot v_L \tag{5-17}$$

Where E_L, E_T, v_L, v_T are the composite young's moduli and passion's ratios in the longitudinal and transverse directions, respectively; V_f is the carbon fiber volume fraction; E_m,

E_f, v_f, v_m, G_f and G_m are the Young's moduli, Passion's ratios and shear moduli of matrix and fiber, respectively; and G_c is the shear modulus in the composite x-z plane.

The fiber reinforcement geometric effect on the longitudinal direction is minimal as the uniform strain is assumed. However, the volume occupied by the fibers and their circular cross-section can well affect the transverse modulus and the shear modulus in the fiber reinforced layers. The effective transverse modulus of the fiber reinforced layers with cylindrical fibres in a square array is estimated using the Hopkins-Chamis model. The basic idea is shown in Figure 5-7.

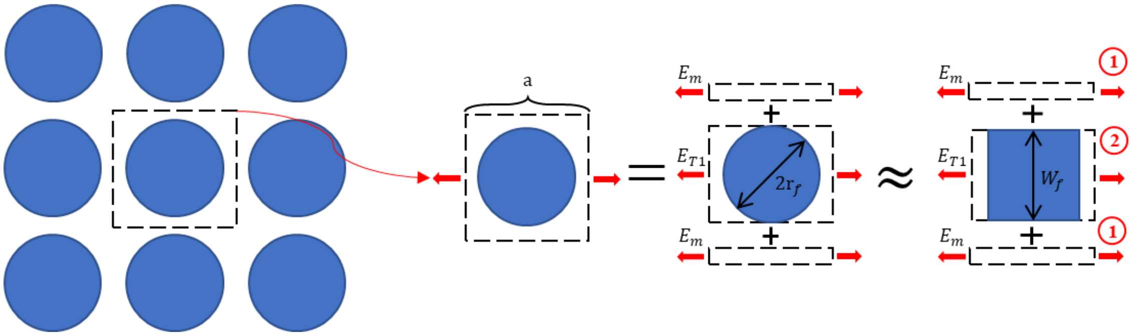

Figure 5-7: Hopkins-Chamis model for composite transverse elastic modulus

In the Hopkins-Chamis model, the transverse performance of each unit is composed of two different regions as seen in Figure 5-7. The first regions are only the unreinforced matrix material and the second region is the circle fiber cross-section, which is approximated by an effective square with the same area. The effective square side length is given in Equations (5-18) and (5-19):

$$r_f{}^2\pi = W_f{}^2 \tag{5-18}$$

$$W_f = r_f\sqrt{\pi} \tag{5-19}$$

Where r_f is the radius of fiber reinforcement and W_f is effective square side length.

In the second region, the transverse modulus is calculated assuming uniform stress conditions as shown in Equation (5-20):

$$E_{T1} = \left[\frac{(a-W_f)}{aE_m} + \frac{W_f}{aE_f}\right]^{-1} \tag{5-20}$$

Where a is the effective square side length. The integral transverse modulus of the whole basic unit is combined in each region under the uniform strain condition as seen in Equation (5-21):

$$E_T = \frac{(a-W_f)}{a}E_m + \frac{W_f}{a}E_{T1} \tag{5-21}$$

The relation between the fiber volume fraction and the transverse elastic modulus is given by

$$V_f = \frac{{W_f}^2}{a^2} \tag{5-22}$$

$$E_T = E_m(1 - \sqrt{V_f} + \frac{\sqrt{V_f}}{1-(1-E_m/E_f)\sqrt{V_f}}) \tag{5-23}$$

Moreover, the in-plane shear stress is solved following the same steps. The result is given by

$$G_c = G_m(1 - \sqrt{V_f} + \frac{\sqrt{V_f}}{1-(1-G_m/G_f)\sqrt{V_f}}) \tag{5-24}$$

The stress tensors in the x-z coordinate system (Figure 5-8 (b)) are obtained by the rule of mixture. For the off-axis stiffnesses with different orientation angles, as seen in Figure 5-8 (c), the transformed properties calculated by the transformation matrix are given in Equation (5-25) to Equation (5-29).

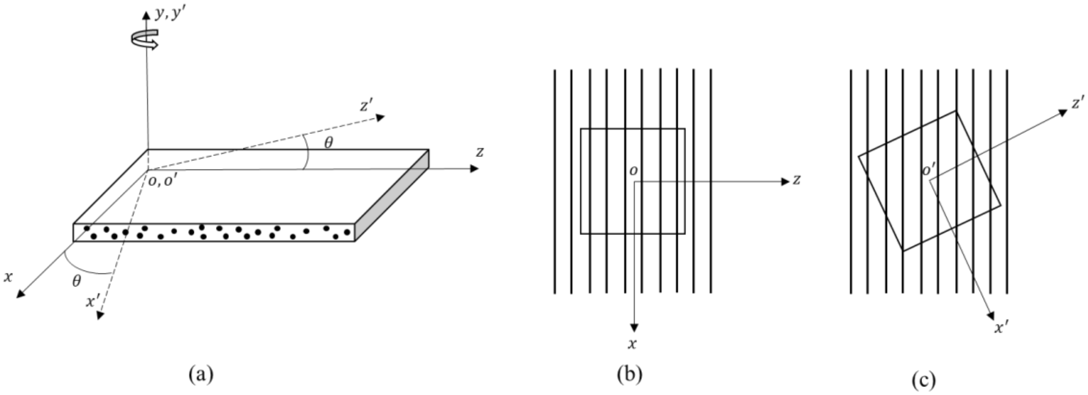

Figure 5-8: (a) Definition of unidirectional carbon fiber reinforced laminar coordinate systems; (b) on-axis fiber arrangement; (c) off-axis fiber arrangement

$$\sigma' = \mathrm{T}(\theta)\sigma \tag{5-25}$$

$$\varepsilon' = T(\theta)\varepsilon \tag{5-26}$$

$$[\sigma'] = [C'(\theta)][\varepsilon'] \tag{5-27}$$

with

$$\mathrm{T}(\theta) = \begin{bmatrix} \cos^2\theta & \sin^2\theta & 0 \\ \sin^2\theta & \cos^2\theta & 0 \\ 0 & 0 & 2cos\theta sin\theta \end{bmatrix} \tag{5-28}$$

$$C'(\theta) = \mathrm{T}(\theta)C\mathrm{T}(\theta)^{-1} \tag{5-29}$$

Where σ' and ε' are the stress and strain tensors in off-axis coordinate; $\mathrm{T}(\theta)$ is the rotation matrix; θ is the rotation angle; and $C'(\theta)$ is the off-axis stiffness.

Combining Equation (5-8) and Equation (5-10), the young's modulus and the in-plane Poisson's ratio can be expressed by extracting elements from the compliance matrix as:

$$E'(\theta) = \frac{1}{[S'(\theta)](1,1)} \tag{5-30}$$

$$v_{xz}'(\theta) = \frac{[S'(\theta)](2,1)}{[S'(\theta)](1,1)} \tag{5-31}$$

Where E' and $v_{xz}'$are the young's modulus and in-plane Poisson's ratio by the θ degree rotated coordinate system, respectively. $[S'(\theta)](1,1)$ and $[S'(\theta)](2,1)$ are the first and second elements in the off-axis compliance matrix, respectively.

The effective elastic modulus and Poisson's ratio of the carbon fiber reinforced layers are the result of two orthogonal carbon fiber arrangements. During the POR bending test, assuming uniform deformation of the composite in all directions results in effective properties that are identical and equal to the average of all loading directions, that is:

$$E_f = \frac{\int_0^{\frac{\pi}{2}} \mathrm{E}'(\theta)d\theta + \int_0^{\frac{\pi}{2}} \mathrm{E}'(\frac{\pi}{2}-\theta)d\theta}{\pi} \tag{5-32}$$

$$v_{xzf} = \frac{\int_0^{\frac{\pi}{2}} v_{xz}'(\theta)d\theta + \int_0^{\frac{\pi}{2}} v_{xz}'(\frac{\pi}{2}-\theta)d\theta}{\pi} \tag{5-33}$$

Where E_f and v_{xzf} are the averaged young's modulus and in-plane Poisson's ratio of carbon fiber reinforced layers.

5.2.2 Multilayered discs

Hsueh et al. suggested formulas that are suitable for the calculation of multilayered biaxial bending problems [51]. This theory is based on monolayered solutions and assumes a perfect interface bonding between layers. For a pure bending case, the bending moment results in bending normal stress maxima at the top and bottom surfaces, which can be written as:

$$\sigma_b = \frac{M(y-y^*)}{I} \qquad (5\text{-}34)$$

Where σ_b is the bending normal stress; y is the position in y-axis; y^* is the neutral plane position (for the monolayer disc, $y^* = 0$); I is the moment of inertia along the neutral plane (for the monolayer disc, $I = \frac{t^3}{12}$).

For multilayer composites, layers with distinguished properties result in changes in neutral plane and moment of inertia. In order to solve this problem, the flexural rigidity is considered. The flexural rigidity of an elastic circular plate is determined by Equation (5-35).

$$D = \frac{EI}{(1-v^2)} \qquad (5\text{-}35)$$

Where D is the flexural rigidity; E is the young's modulus; and v is the Poisson's ratio.

Based on the composite structure as seen in Figure 5-3, by combining Equation (5-35) into Equation (5-34), the stress-moment relation is calculated by Equations (5-36) and (5-37).

$$\sigma_i = \frac{E_i(y-y^*)M}{(1-v_i)(1+v_{ave})D^*} \qquad (5\text{-}36)$$

$$E_{1,3,5} = E_{Al}; v_{1,3,5} = v_{Al}; E_{2,4} = E_f; v_{2,4} = v_{xzf} \qquad (5\text{-}37)$$

Where σ_i, E_i and v_i are flexural stress, elastic modulus and Poisson's ratio of the ith layer, respectively; y is the position in the direction of the composite thickness and loading direction; y^* and D^* are the neutral plane position and flexural rigidity, respectively; M is the bending moment; and v_{ave} is the average Poisson's ratio of the entire material. y^*, D^* and v_{ave} are defined in Equation (5-38), (5-39) and (5-40).

$$y^* = \frac{\sum_{i=1}^{n}\left(\frac{E_i t_i}{1-v_i{}^2}\right)\left(h_{i-1}+\frac{t_i}{2}\right)}{\sum_{i=1}^{n}\frac{E_i t_i}{1-v_i{}^2}} \qquad (5\text{-}38)$$

$$D^* = \sum_{i=1}^{n}\left(\frac{E_i t_i}{1-v_i{}^2}\right)\left(h_{i-1}{}^2 + h_{i-1}t_i + \frac{t_i{}^2}{3} - \left(h_{i-1} + \frac{t_i}{2}\right)y^*\right) \tag{5-39}$$

$$v_{ave} = \frac{1}{h_i}\sum_{i=1}^{n} v_i t_i \tag{5-40}$$

Where E_i, v_i, t_i and h_i are the elastic modulus, Poisson's ratio, thickness and position of the ith layer, respectively.

The moment-force relation in piston-on-ring biaxial bending is given by Equation (3-15). Thus, the stress distribution along the thickness can be solved by Equation (5-36). Moreover, the effective young's modulus of the composite sample is calculated by the inverse of Equation (5-35):

$$E_{eff} = \frac{12(1-v^2)D^*}{t_s{}^3} \tag{5-41}$$

Where E_{eff} is the effective flexural modulus of the entire composite and t_s is the sample total thickness.

5.2.3 Piston-on-ring bending strength

The elongation to fracture of aluminum is much larger than that of carbon fiber. Therefore, the failure criterion of the composite can be based on the carbon fiber strength limit in cases where substantial plastic deformations are observed at sample fracture.

For modelling and assessment purposes, the aluminum matrix is assumed as an ideal elastic-plastic material as presented in Figure 5-9. This means, prior to the yield point (ε_y), the material has a perfectly elastic behaviour with a linear stress-strain relation. Beyond yielding, ideal plasticity results in a constant plastic stress that is independent of the strain until material fracture. Considering the mechanical properties of 6061 aluminum with T4 treatment, the yield stress (σ_y) of the matrix is taken to be 145 MPa.

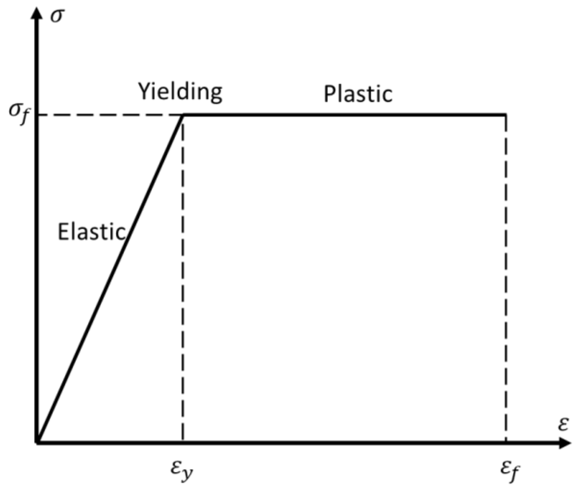

Figure 5-9: Stress-strain curve of an ideal elastic-plastic material

In contrast, the carbon fiber reinforcement is assumed to behave purely linear elastically, with no plastic deformation, during the entire bend test until failure. As such, the elastic behaviour of the strengthened layer at high bending loads is only contributed by carbon fiber while the aluminum in the layer deforms purely plastically. Adding up the two deformation contributions, the stress distribution in the strengthened composite layers can be represented as in Figure 5-10. The failure bending moment in the system can then be assessed as in Equation (5-42).

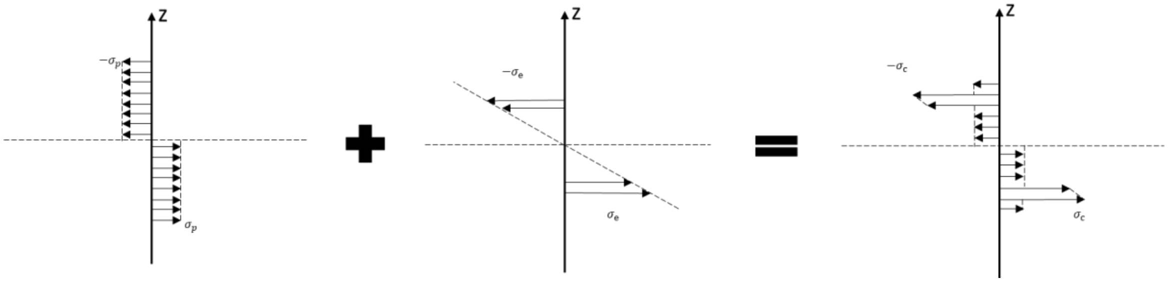

Figure 5-10: Combination of elastic and plastic bending stresses along the thickness

$$\mathrm{M}_{por} = \mathrm{M}_{matrix} + M_{cf} \tag{5-42}$$

Where M_{por} is the bending moment in the POR test; M_{matrix} is the bending moment contribution by plastic deformation of the Aluminum matrix; and M_{cf} is the bending moment contribution of carbon fiber.

The failure strength of the carbon fiber reinforced layer is calculated by the rule of mixture, that is:

$$\sigma_{failure} = V_f \sigma_f + \left(1 - V_f\right) \cdot \sigma_m \tag{5-43}$$

Where $\sigma_{failure}$ is the flexural strength of the composite; σ_f and σ_m are the ultimate failure strengths of carbon fiber and aluminum, respectively; and V_f is the carbon fiber volume fraction.

5.2.4 Interfacial shear stress

Figure 5-11 shows the reaction force and moment in the pure bending beam. The relationship between the bending moment and the shear force in the cross-section is obtained by the moment equilibrium Equation (5-44):

$$\sum M = 0 \Rightarrow dM - F_s dx = 0 \tag{5-44}$$

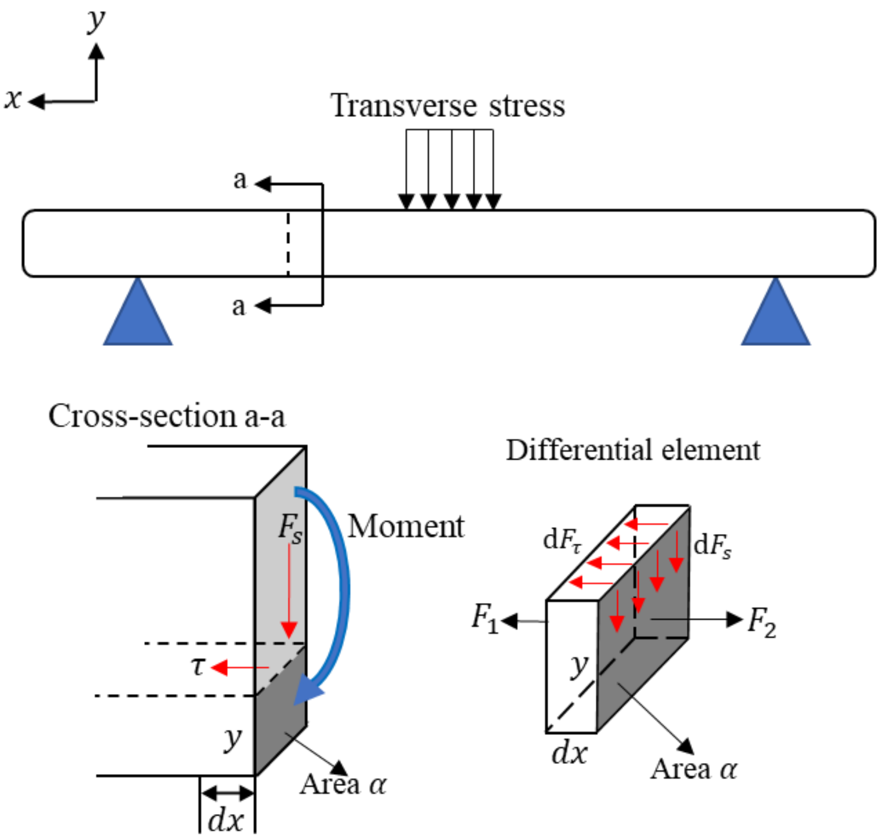

Figure 5-11: Free-body diagrams of a bending beam

The interfacial shear stress is defined by the transverse shear stress in the x-axis. The force equilibrium expression is given in Equation (5-45).

$$\sum F_x = 0 \Rightarrow dF - \tau dx = 0 \tag{5-45}$$

Where τ is the transverse shear stress; and dx is the differential element along the radial direction.

Combining Equation (5-44) and (5-45) gives the expression of the interfacial shear stress:

$$\tau = \frac{F_s \int y dx}{I_z} \tag{5-46}$$

Where F_s is the transverse shear force; $\int ydx$ is the first moment of area; and I_z is the moment of inertia.

Opposite maximum bending normal stresses are located at upper and lower surfaces, while the maximum interfacial shear stress is located at the neutral axis and vanishes at the two sides. Meanwhile, the value of interfacial shear stress is only affected by the shear force and the cross-section geometry, which are nonrelated to the aluminum plastic behavior. For POR bending, the maximum applied transverse shear force is located along the piston circumference as shown in Figure 5-12. The relation between the applied bending load and the transverse shear force is given in Equation (5-47).

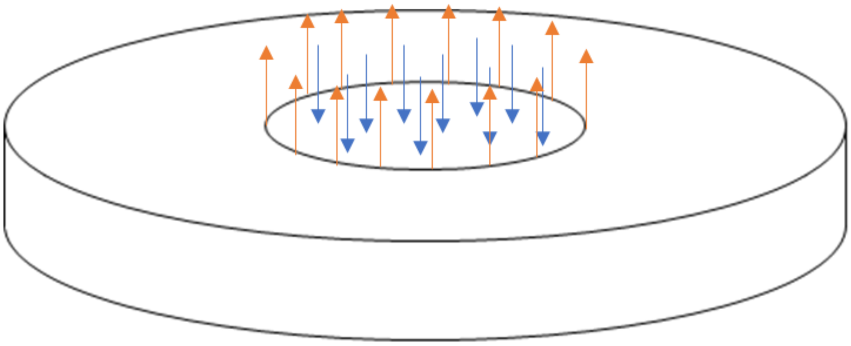

Figure 5-12: Illustration of the maximum applied transverse shear force in piston-on-ring testing

$$F_s = \frac{P}{2\pi r_1} \tag{5-47}$$

5.3 Finite element analysis (FEA)

Finite element analysis (FEA) is one of the most important analytical and numerical tools for simulating engineering problems, particularly for complex geometry. In this study, FEA is applied to assess the effective young’s modulus of the composites with the given arrangement of carbon fibers. The overall composite behaviour is predicted by analysing the compounded elastic behaviour of its basic unit cells. The basic principle of FEA is finding the approximate solution by dividing a continuum mechanics region into small elements. Thus, the accuracy of the simulation is highly dependent on an appropriate definition of geometry, property and mesh elements.

Abaqus is one of the most widely used FEA software. With a powerful graphical environment, Abaqus is suitable for modelling structural components. The mechanical problems are solved by adding the material properties, loading and limiting conditions. In this study, 3D modelling is applied on a uniform strain across the composite. An effective young’s modulus is applied uniformly across the composite and the plain weave fiber fabric pattern is assumed to be maintained.

Composite layers are represented by periodic element units. The representative unit model has two sections: fiber yarns and matrix. The properties of the yarns are assumed to be the same as those of carbon fiber. Three different yarn distances are considered as shown in Table 5-2. Figure 5-13 shows the geometry simulation for the original fabric structure.

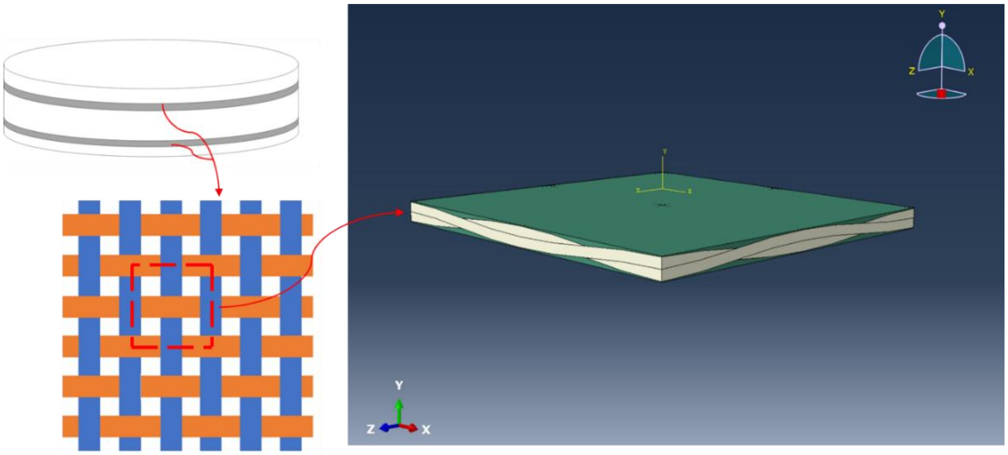

Figure 5-13: Geometry simulation for the original plain weave carbon fiber fabric

The elastic constants of periodic element units are solved by applying specific strains in different sets, as seen in Figure 5-14. As the plain weave fabric provides identical elastic properties in x and z axes, the elastic constants can be simplified to 4 independent sets. The boundary conditions are specified for each set as follow:

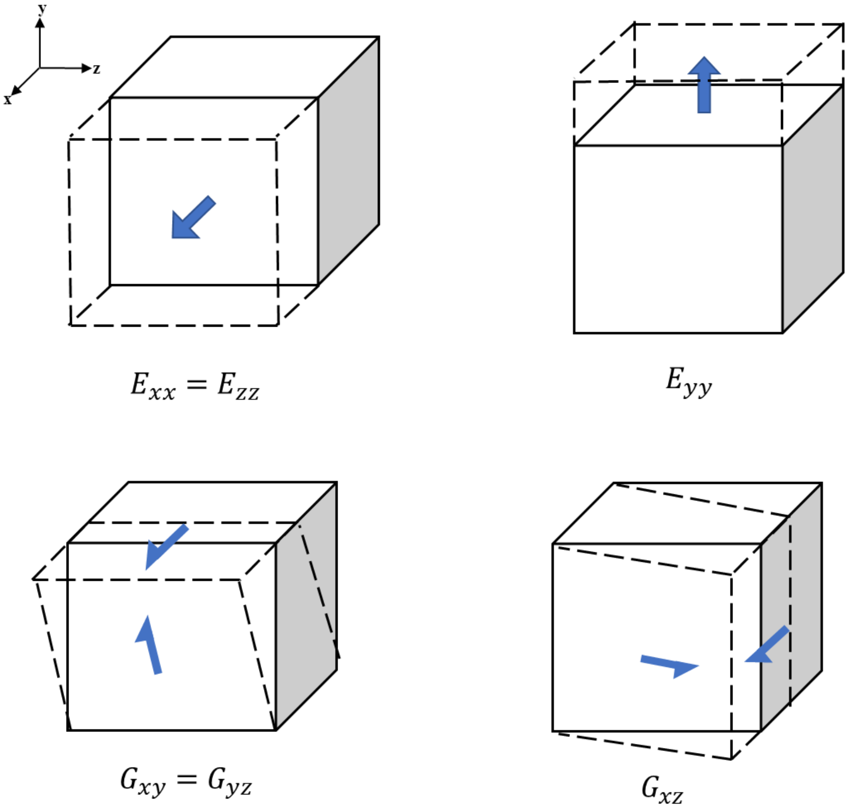

$E_{xx} = E_{zz}$ E_{yy}

$G_{xy} = G_{yz}$ G_{xz}

Figure 5-14: 4 different deformation conditions solved in FEA model

For elastic modulus $E_{xx} (E_{xx} = E_{zz})$:

$$X_{(Surface)} = \frac{x}{a} \tag{5-48}$$

$$Y_{(Surface)} = Z_{(Surface)} = 0 \tag{5-49}$$

For elastic modulus E_{yy}:

$$Y_{(Surface)} = \frac{y}{b} \tag{5-50}$$

$$Y_{(Surface)} = Z_{(Surface)} = 0 \tag{5-51}$$

For shear modulus $G_{xy} (G_{xy} = G_{yz})$:

$$X_{(Surface)} = \frac{y}{b} \tag{5-52}$$

$$Y_{(Surface)} = Z_{(Surface)} = 0 \tag{5-53}$$

For shear modulus G_{xz}:

$$X_{(Surface)} = \frac{z}{c} \tag{5-54}$$

$$Y_{(Surface)} = Z_{(Surface)} = 0 \tag{5-55}$$

Where $Surface = \{(0, y, z), (a, y, z), (x, 0, z), (x, b, z), (x, y, 0), (x, y, c)\}$ is all the surface positions of representative units. X, Y and Z are the displacement components along x, y and z axes. Figure 5-15 shows the coordinate reference applied in FEA modelling.

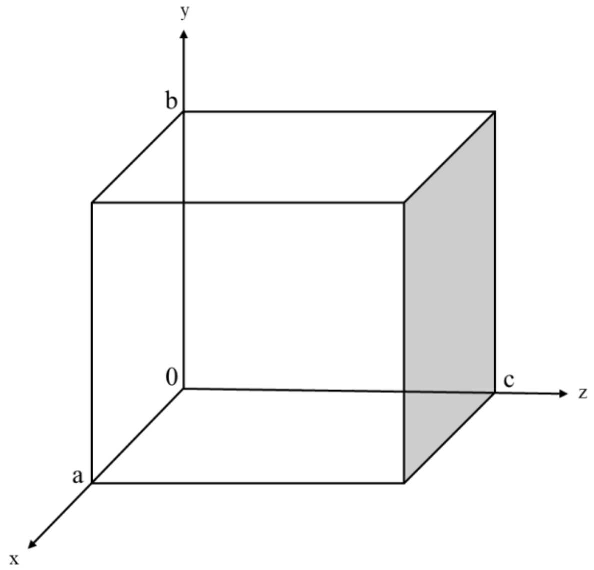

Figure 5-15: The coordinate reference applied in FEA modelling

Abaqus/CAE provides a sweep meshing technique for simulating parts with complex surface regions. In this study, hexahedral mesh elements are applied for the 3D analysis. 0.1mm element size provided reliable results with a proper solving time. In order to obtain the effective elastic properties, a uniform strain is applied to the structure with a specific value of

1. Figure 5-16 shows the displacement and boundary conditions applied on the original plain weave carbon fiber representative unit.

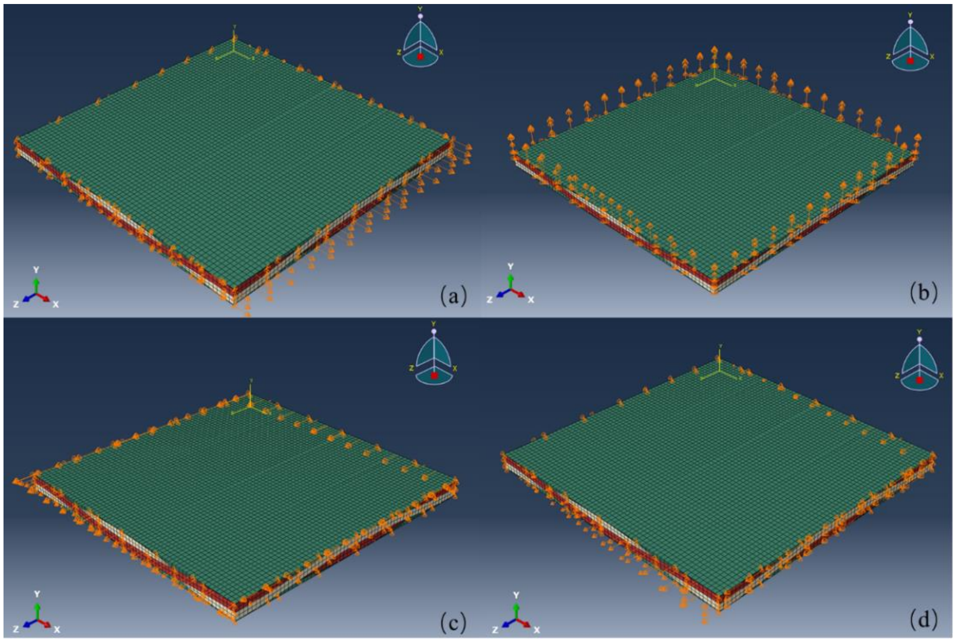

Figure 5-16: Displacement and boundary conditions for FEA modelling: (a) and (b) are the normal displacements in x and y axes; (c) and (d) are the shear displacements in y-z and x-z planes, respectively

FEA modelling results provide the stiffness matrix of each finite element. The composite macroscopic properties are homogenized by averaging the microscopic stresses using Equation (5-56). All effective elastic constants can be solved by substituting Equation (5-56) into Equation (5-10).

$$[S] = \frac{1}{V}\int_{\Omega} [S]\, dv = \frac{\sum_{i}^{N} V_i [S]_i}{V} \qquad (5\text{-}56)$$

Where [S] is the compliance matrix and V is the total volume of the representative unit. Ω is the whole structure; dv is the differential volume; V_i and $[S]_i$ are the volume and compliance at each element, respectively.

The second model simulates the entire sample used in POR bend testing. The bend test samples have a 4mm thickness with 2 carbon fiber strengthened layers. The sample diameter is 76.2mm. Two partitions are created to simulate the loading piston and the supporting ring during the bend tests.

The aluminum matrix has two regions: In the purely elastic deformation case, the load-displacement curve shows the effective bending modulus of the composite. At the yield stress (145 MPa), ideal elastic-plasticity deformation gives a prediction of composite maximum bending strength. Moreover, the strengthened layers are assumed to deform purely linear elastically until failure.

The symmetric condition is applied to optimize the computing efficiency. Thus, only a quarter of the sample set-up is modelled. The force is assumed uniformly distributed on the contact surface with the loading piston, and the supporting ring is defined to restrict the sample displacement in the z direction only. Hexahedral mesh elements and sweep meshing technique are used. The mesh element size is 1mm as shown in Figure 5-17.

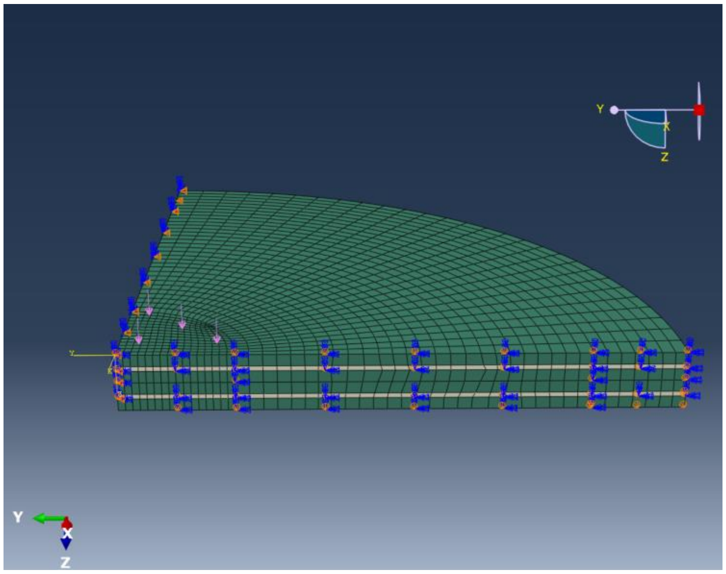

Figure 5-17: Modelling set-up for piston-on-ring bend testing

Besides considering strengthened layers with different carbon fiber volume fractions, a monolayer sample with only aluminum is also solved to calibrate the applied load by matching with the flexural bend strength of aluminum.

After solving the modelling, the mechanical properties are evaluated by tracking stress components at specific positions. The maximum bending displacement is found at the neutral center of the sample as shown in Figure 5-18 (a). Thus, the flexural modulus of the composite can be solved by Equation (3-16) and Equation (3-19). Furthermore, Figure 5-18 (b) and Figure 5-18 (c) give the stress distribution along the thickness and the maximum interfacial shear stress along the piston circumference.

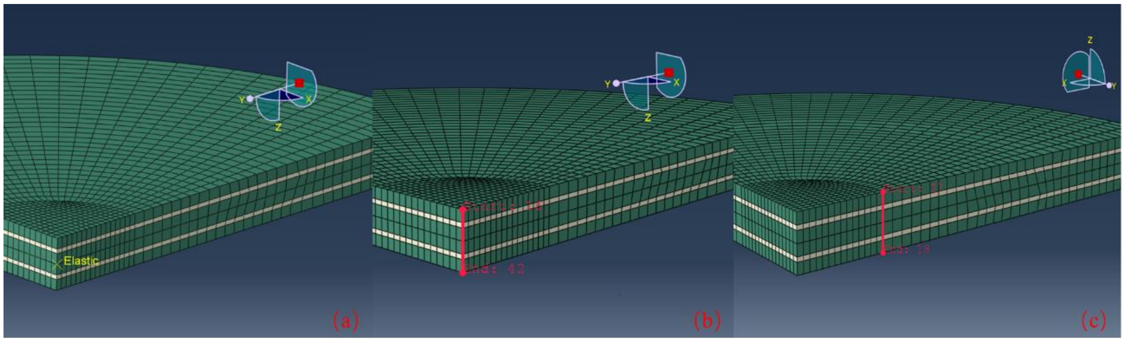

Figure 5-18: Data collection for mechanical properties calculation: (a) maximum elastic deformation; (b) maximum bending stress distribution; (c) maximum interfacial shear stress at carbon fiber effected layer.

5.4 Modelling results

The FEA simulation in Figure 5-19 shows the stress distribution within the strengthened layer with Vf= 63.13vol%, 42.06vol% and 31.53vol% corresponding to overall composite carbon fiber volume fraction of 4.89vol%, 3.26vol% and 2.44vol%, respectively. The high stress concentration in the longitudinal fiber yarns with high elastic modulus can be seen. The maximum stresses are located at the intersection of orthogonal yarns. Meanwhile, the transverse yarns carry the least stresses in the strengthened layer.

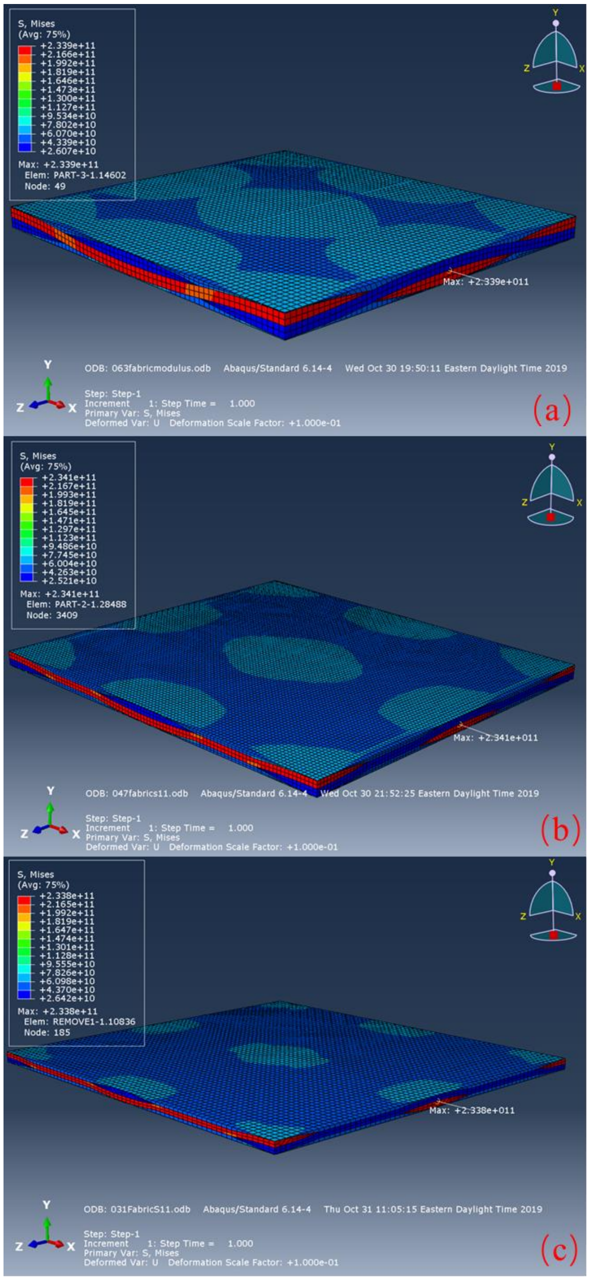

Figure 5-19: Von Mises stress results of the FEA model for different carbon fiber volume fractions in the strengthened layers: (a) 63.13vol% ; (b) 42.06vol%; (c) 31.53vol%

Table 5-3 shows the prediction of the carbon fiber strengthened layer elastic properties. In this table, the out-plane shear moduli and Poisson's ratios are not provided for the ANA solution because it's based on plane stress conditions. The FEA results show higher bending moduli, but lower in-plane Poisson's ratios.

Table 5-3: Elastic properties of the strengthened layers calculated by the ANA and FEA models for different carbon fiber volume fractions

Properties	**31.53vol%**		**42.06vol%**		**63.13vol%**	
	ANA result	FEA result	ANA result	FEA result	ANA result	FEA result
E_{xx}, E_{zz} **(GPa)**	88.93	91.10	95.91	97.51	110.1	111.1
E_{yy} **(GPa)**	57.79	61.34	54.69	57.93	48.96	50.71
G_{xy}, G_{yz} **(GPa)**	----	23.04	----	22.12	----	20.25
G_{xz} **(GPa)**	25.94	24.05	25.94	23.42	22.00	22.18
v_{xy}, v_{yz}	----	0.3424	----	0.3416	----	0.3060
v_{xz}	0.2793	0.2108	0.2687	0.1660	0.2501	0.1273

Table 5-4 gives the effective flexural moduli of the whole composite in POR test. It shows that the effective flexural moduli constantly increase with the carbon fiber volume fractions in both the ANA and FEA solutions that are in good agreement.

Table 5-4: Modelled effective flexural modulus of the entire composite for different carbon fiber volume fractions

Carbon fiber volume fraction in the strengthened layer ($V_{f_{CF}}$)	**Overall carbon fiber volume fraction in the entire composite (V_f)**	**Whole composite (GPa)**	
		ANA result	FEA result
Pure Al	-	69.00	68.68
31.53vol%	**2.44vol%**	70.51	69.78
42.06vol%	**3.26vol%**	71.10	69.96
63.31vol%	**4.89vol%**	72.34	70.80

In order to compare modelling and experimental results, the relationship between the flexural modulus and the fiber volume fraction is linearly fitted as seen in Figure 5-20. In contrast to the estimate for the carbon fiber strengthened layers, the FEA model yields a lower flexural modulus prediction for the overall composite compared with ANA results. The discrepancy in composite flexural modulus between the two models increases with the carbon fiber volume fraction.

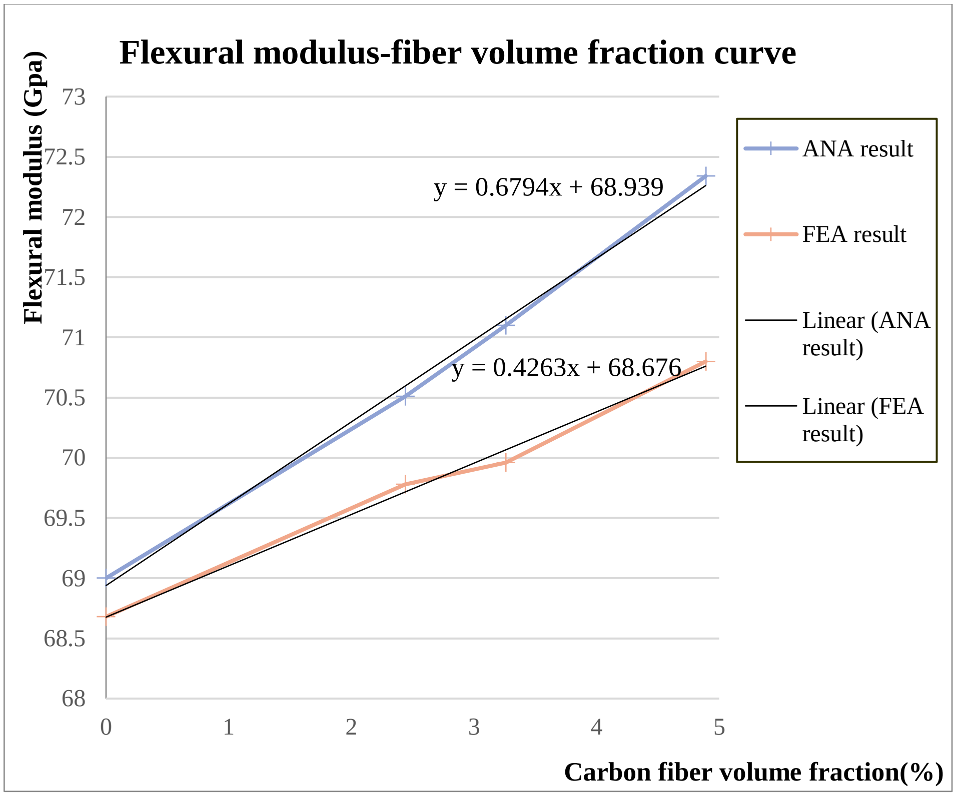

Figure 5-20: Increase in composite flexural modulus as the overall carbon fiber volume fraction increases from 0 to 4.89vol%

By extracting the displacement and reaction force data for the neutral plane from the FEA model as defined in Figure 5-21, the flexural stress-strain curve is calculated by combining Equation (3-12) and Equation (3-19). A significant strengthening effect is found in composites in the high strain region.

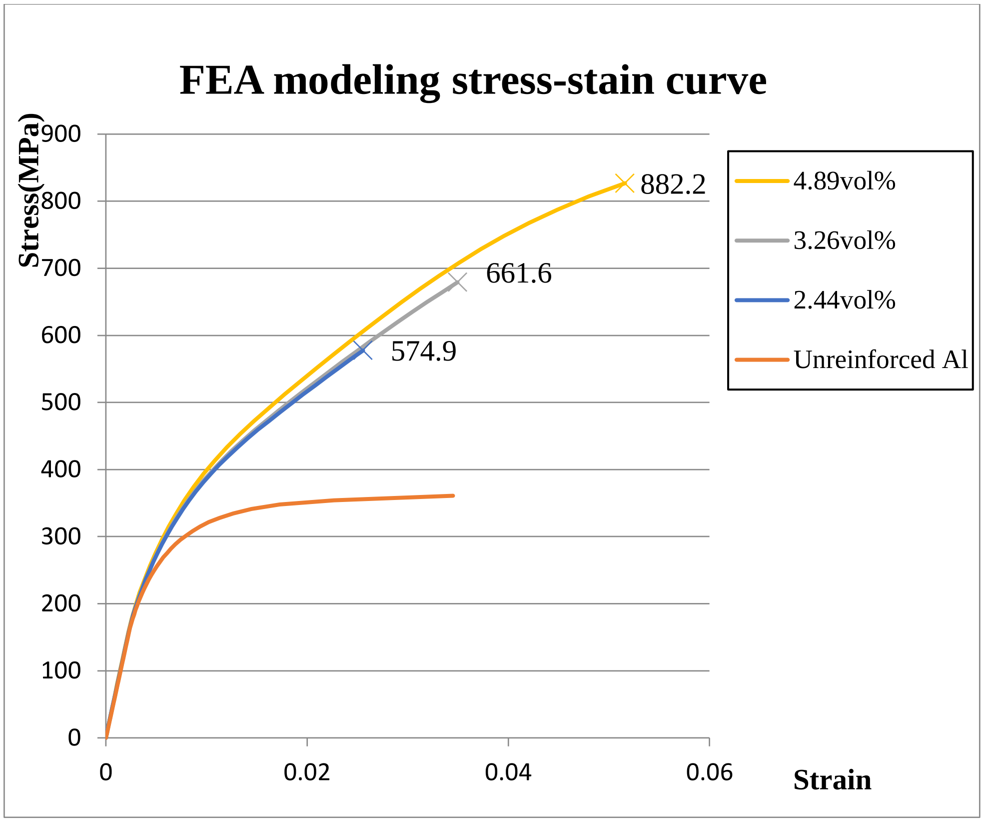

Figure 5-21: POR test stress-strain curves by the FEA model

The offset yield strength is determined at 0.2% strain of each curve as displayed in Table 5-5. Figure 5-22 shows the yield strength of unreinforced aluminum. As the ideal plastic performance is applied in FEA, the maximum flexural strength of unreinforced aluminum is assumed equal to the yield strength which is 271.0 MPa.

Table 5-5: FEA modelled flexural yield strength for different carbon fiber volume fractions

V_f	Flexural Yield strength (MPa)
Unreinforced Al	271.0
2.44vol%	313.2
3.26vol%	315.6
4.89vol%	323.5

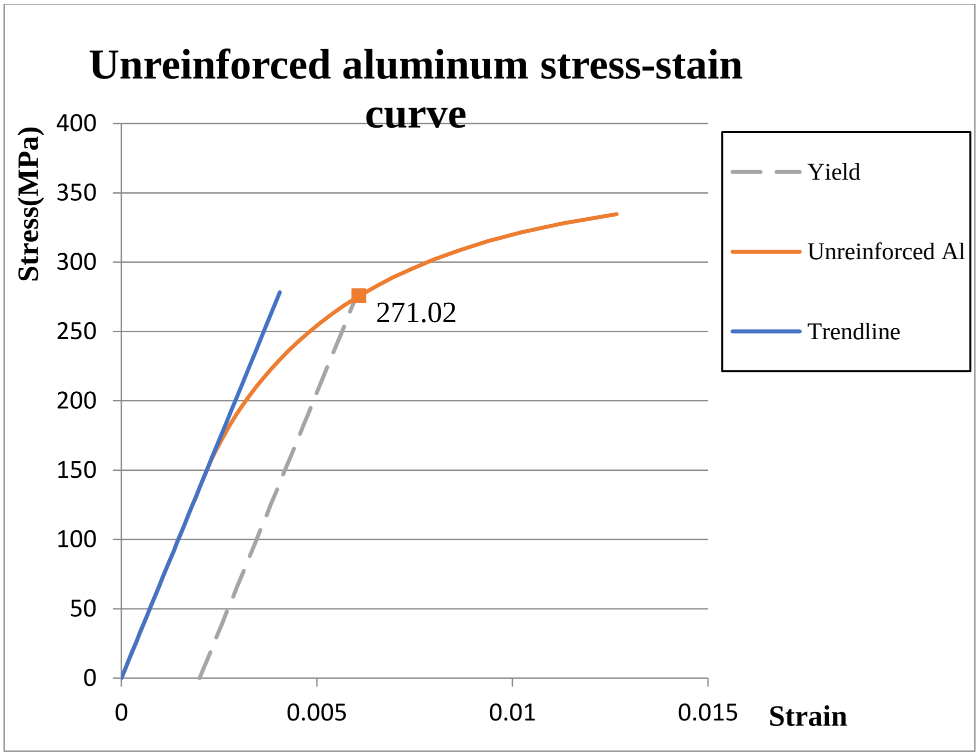

Figure 5-22: Yield point of unreinforced aluminum by FEA model

The linear relationship between bending strength and carbon fiber volume fraction is shown in Figure 5-23. In general, the composite strength increases with the addition of reinforcements. For the ANA model, the flexural strength of unreinforced aluminum is unavailable due to the assumption of ideal plastic behaviour of aluminum. The FEA model predicts a dramatic improvement of the effective flexural strength of all strengthened composite materials with 3 times increase at V_f =4.89vol% carbon fiber compared to unreinforced Aluminum. Moreover, the FEA simulation results are higher than the ANA results at 2.44vol% and 3.26vol% volume fraction due to the consideration of non-linear bending behaviour. In contrast, FEA yields results lower than the ANA model at 4.89vol% volume fraction due to the three-dimensional strain effect. Also, the simulation results of the maximum bend load and effective flexural strength are summarized in Table 5-6.

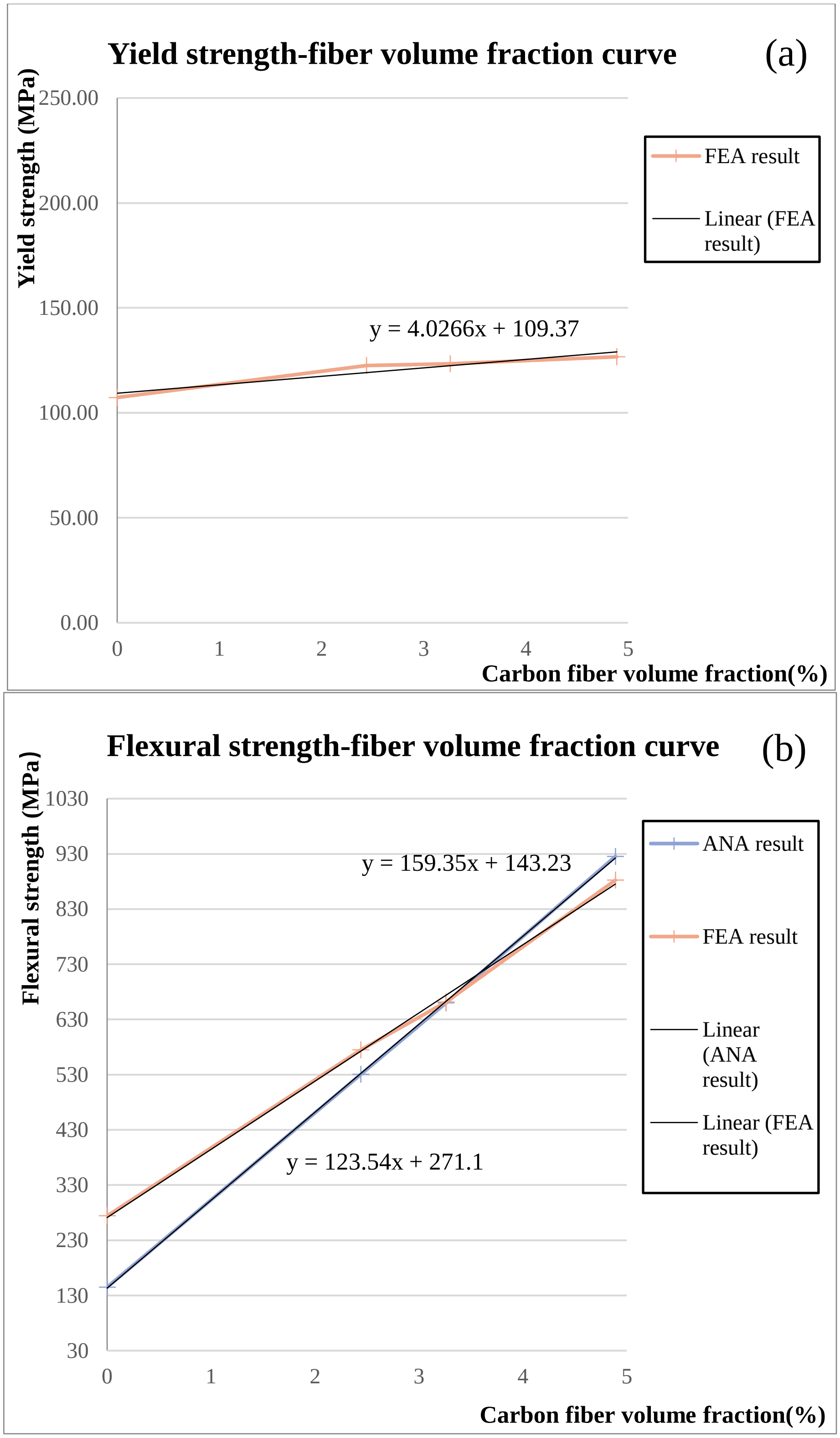

Figure 5-23: Linear relationship between the bending strength and the carbon fiber volume fraction as obtained from FEA and ANA models: (a) yield strength; (b) flexural strength

Table 5-6: Comparison of ANA and FEA results for maximum bend load and flexural strength

V_f	Maximum bend load (N)		Effective flexural strength (MPa)	
	ANA value	FEA value	ANA value	FEA value
Pure Al	----	4080	----	271.0
2.44vol%	6420	6960	530.3	574.9
3.26vol%	7990	8010	660.0	661.6
4.89vol%	11200	10680	925.1	882.2

Figure 5-24 shows the stress distribution along the thickness of the composites subjected to bend loading. Due to the low strength and strong plasticity of the aluminum matrix, the highest bend stresses are observed in the carbon fiber strengthened layers. The results of the FEA simulation give a uniform distribution of the stress across the thickness of the strengthened layers due to the element size restriction. Figure 5-25 shows the interfacial shear stress under the maximum bending load. High carbon fiber volume fractions require a better interface shear strength to prevent fiber pull-out. For interfacial shear strength higher than the threshold value, no interface debonding takes place and the composites will fail by fiber breakage above the fiber ultimate tensile strength. Otherwise, interface failure occurs by delamination at lower stresses.

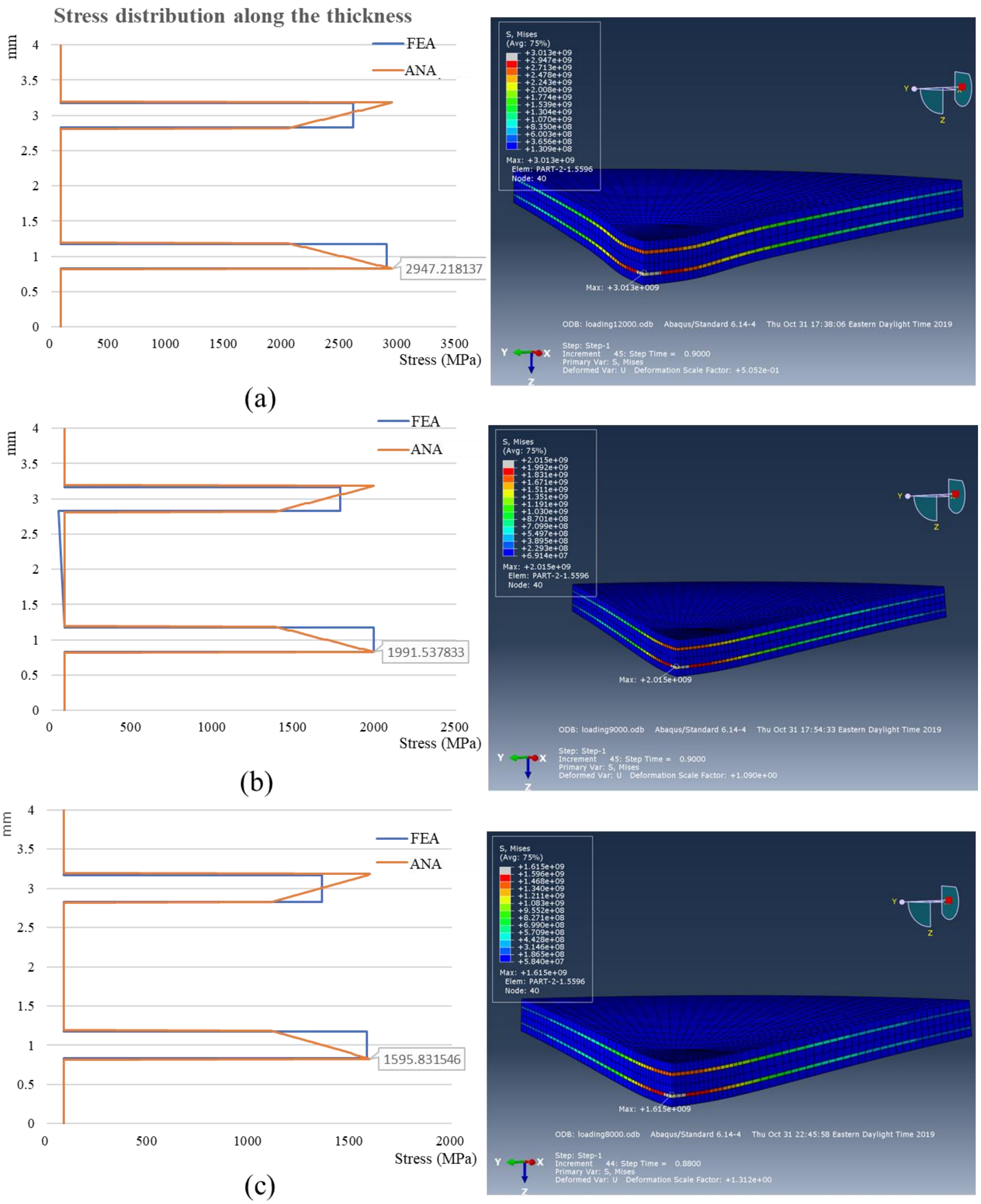

(a)

(b)

(c)

Figure 5-24: ANA and FEA results comparison of bend stresses along the thickness of the composite samples subjected to POR bend testing at maximum bending load: (a) $V_f = 4.89$vol%; (b) $V_f = 3.26$vol%; (c) $V_f = 2.44$vol%

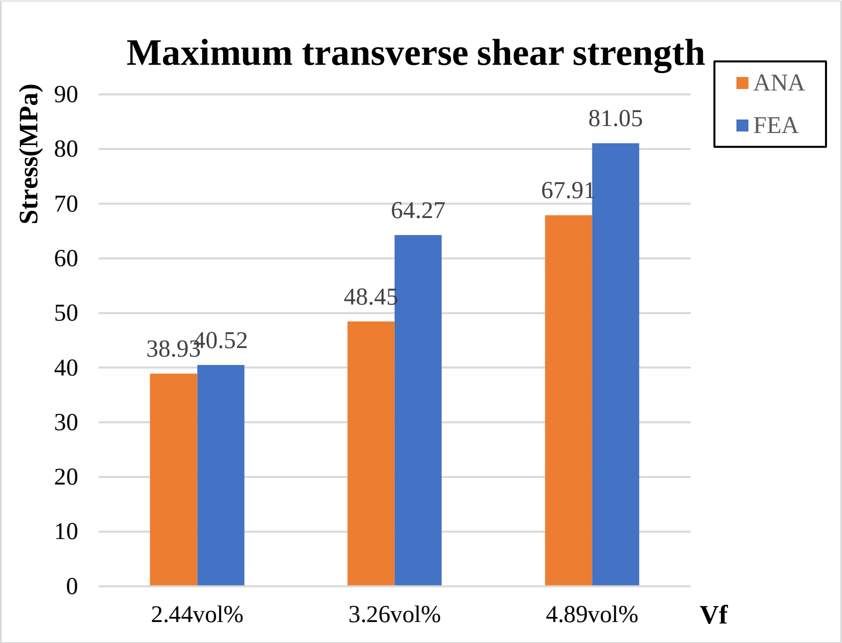

Figure 5-25: ANA and FEA results comparison of the maximum transverse shear strength in the strengthened layers with different carbon fiber volume fractions

6 DISCUSSION

6.1 Comparison of experimental and modelling results

As mentioned in Chapter 3, the experimental results include three different carbon fiber densities with 4 groups of squeeze casting processes: Short casting die results (G1); Long casting die results (G2); Squeeze casting with long die combined with 40 MPa hydraulic press post-processing (G3); and Squeeze casting with long die combined with 20 MPa hydraulic press post-processing (G4). The results confirm that the different manufacturing processes result in the distribution of composite bending properties in a wide range. Figure 6-1 shows the experimental flexural modulus of each process group compared with the model results. Both models show a continuous increase in flexural modulus with increasing carbon fiber content. However, the FEA results are slightly lower than the ANA results due to the considering of the stress in thickness direction in contrast to the ANA model that is based on plane stress conditions. G3 and G4 samples with hydraulic post-processing show a continuous improvement in the flexural modulus with carbon fiber content at all three investigated carbon fiber volume fractions, while G1 samples show a decrease in flexural modulus at high carbon fiber volume fractions from 3.08vol% to 4.55vol%. Moreover, the G3 samples and sample S15 with 4.42vol% carbon fiber volume fraction in the G4 group exhibit superior results exceeding both model predictions.

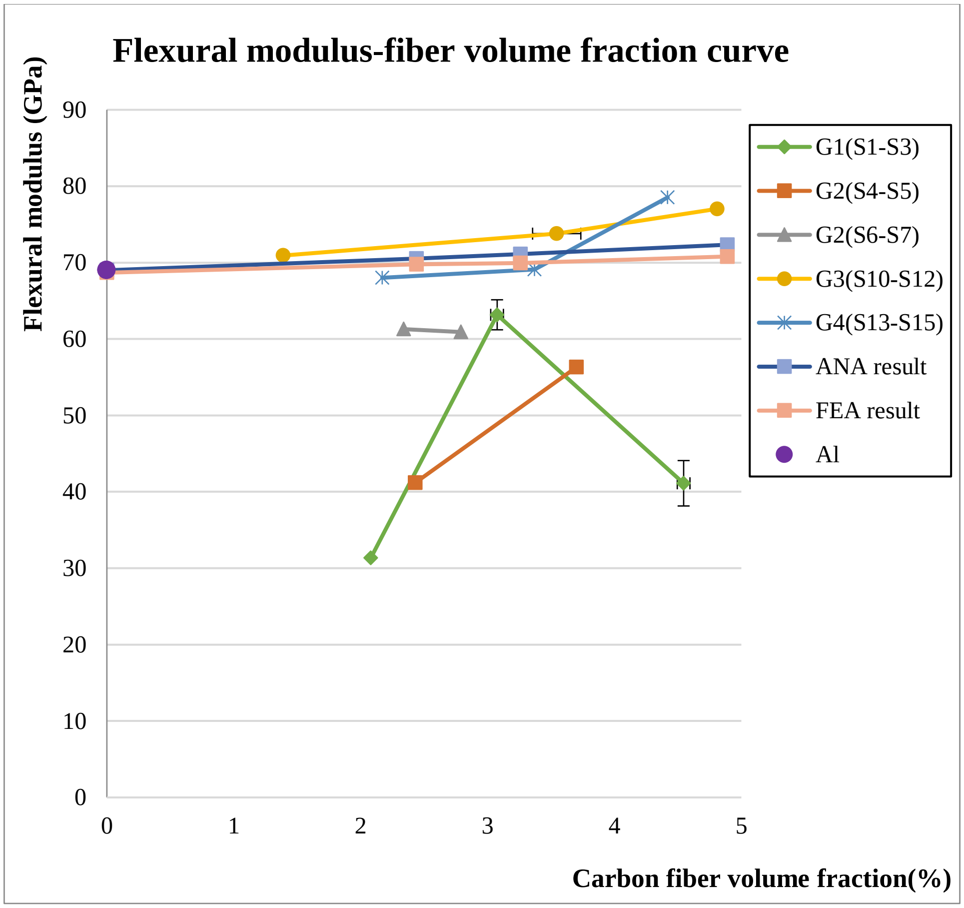

Figure 6-1: Flexural modulus comparison between experiment data, ANA results and FEA results

As the samples in G3 group provide the most consistent results, they are further compared with the model results as displayed in Table 6-1. The experimental data agree well with prediction results, with relatively small differences increasing from 1.48% to 8.54% as the carbon fiber volume fraction increases from 1.23vol% to 4.81vol%. This good agreement suggests good interface bonding between carbon fiber and aluminum matrix, which is a basic assumption of the models. One reason for the discrepancy is that the carbon fibers were observed to move upward during squeeze casting due to their lower density compared to molten aluminum, as illustrated in Figure 6-2. As a result, the strengthened layers are closer to the top surface of the composites. Consequently, the composite samples are stronger than predicted because the composites were tested with the carbon fiber strengthened layers closer to tensile surface on the ring side during the POR bend tests. In this case, the neutral axial is shifted, and carbon fibers carry more stress during the biaxial bend testing, resulting in higher than predicted flexural moduli.

Table 6-1: Flexural modulus differences between modelling and experimental data

Carbon fibre volume fraction[vol%]	**Experimental flexural modulus (GPa)**	**ANA (% difference)**	**FEA (% difference)**
1.39	70.93	1.48	2.04
3.55	73.80	3.37	5.01
4.81	77.04	6.47	8.54

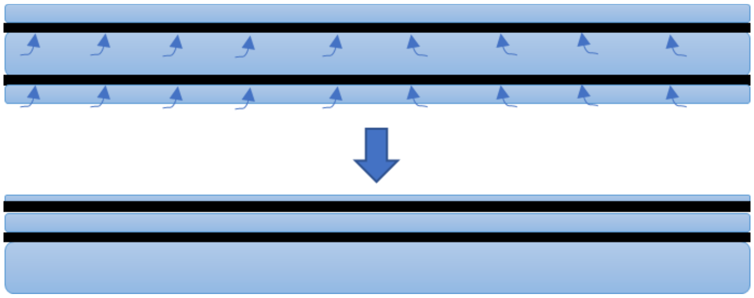

Figure 6-2: Schematic illustration of the upward shifting of carbon fiber fabric during squeeze casting

The comparison between models and experiments for the yield strength are shown in Figure 6-3. The percentage differences between the best sample group G3 and the FEA model results are shown in Table 6-2. The ANA model predictions do not include the yield strength as the bending deflection is not considered. Similar to the case of experimental flexural modulus values, the yield strength of G3 and G4 samples continuously increased with increasing carbon fiber volume fraction, while that of the G1 samples first increases, and then deceases at higher carbon fiber volume fractions. At the maximum investigated carbon fiber volume fraction of 4.81vol%, FEA underestimates the experimental yield strength by 45.25% primarily because the prediction models assume an ideal elastic-plasticity material behaviour of the aluminum matrix. As such, the non-linear stress increase observed during plastic deformation of the samples in the POR tests is the reason experimental results overperform the models. This means the aluminum matrix strain hardens during plastic deformation, leading to a maximum flexural strength higher than the yield strength used as plateau for both modelling approaches.

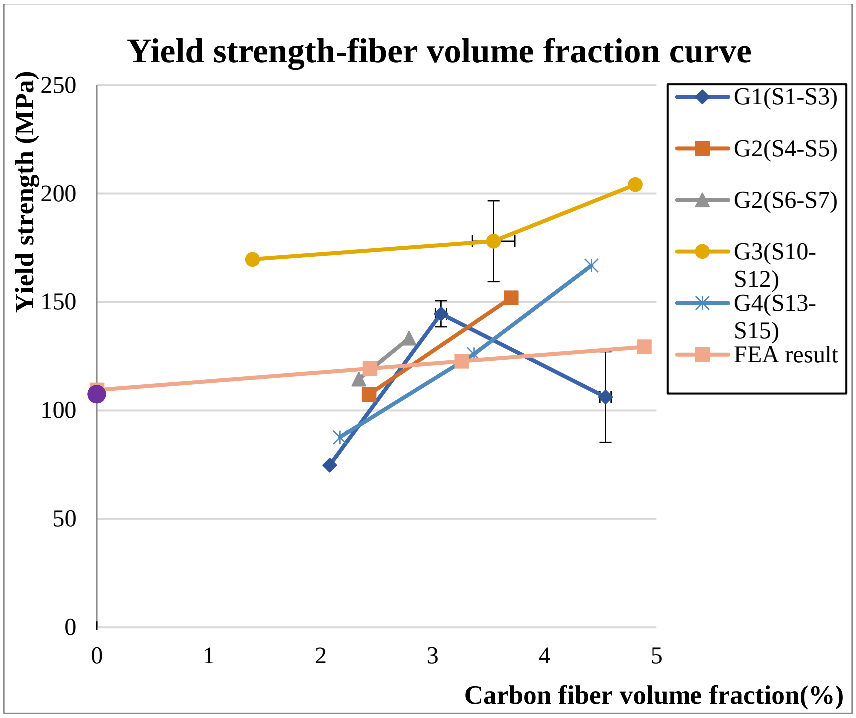

Figure 6-3: Comparisons of experimental yield strength with FEM model results for different carbon fiber volume fractions and infiltration pressures

Table 6-2: Yield strength difference between FEA modelling and G3 samples

Carbon fibre volume fraction(vol%)	Experimental yield strength (MPa)	FEA (% difference)
1.39	169.6	38.42
3.55	178.0	36.01
4.81	204.0	45.25

For the ultimate flexural bending stress, the comparison is shown in Figure 6-4. The FEA results are higher than the ANA results at lower carbon fiber volume fractions and smaller at higher carbon fiber volume fractions due to three-dimensional deformation. At the carbon fiber volume fraction of 3.74vol% where the maximum flexural strength is experimentally measured, ANA and FEA models underestimated this property by 15.84% and 15.73% as seen in Table 6-3, respectively. For the lower carbon fiber volume fraction of 1.39vol%, ANA and FEA underestimate the composite strength by 30.43% and 11.25%, respectively. The largest discrepancy between models and experimental results is at the highest investigated carbon fiber volume fraction of 4.81vol%. Here, ANA and FEA overestimate the flexural strength by 34.34% and 29.46%, respectively. The strong underperformance of the composites at the highest investigated carbon fiber volume fraction can be rationalised by poor infiltration and poor fiber/matrix interface bond in the experimental samples.

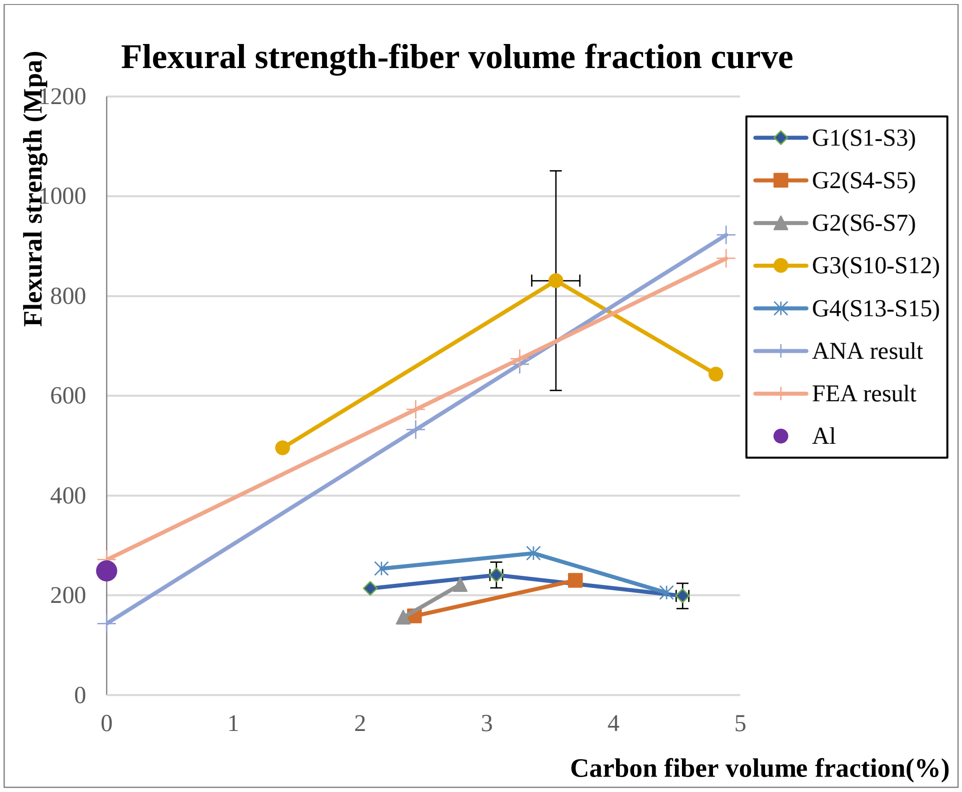

Figure 6-4: Flexural strength comparison between experiment data, ANA and FEA results

Table 6-3: Flexural strength difference between both modelling approaches and G3 samples

Carbon fiber volume fraction(vol%)	Experimental flexural strength (MPa)	ANA (% difference)	FEA (% difference)
1.39	495.6	30.43	11.25
3.55	830.9	15.84	15.73

4.81	643.1	34.34	29.46

6.2 Bending behavior of carbon fiber reinforced aluminum matrix composites

The piston-on-ring bending stress-deflection curves of the S3, S12 composite samples and unreinforced aluminum control sample are shown in Figure 6-5. Both composites have similar carbon fiber volume fractions of 4.81vol% and 4.55vol%, respectively. The composite bending behaviour can generally be divided into three regions before failure. Figure 6-5 shows regions of S12. In the first stage, all samples deform elastically, and the slopes of all bending curves are close. This region is controlled by the elastic deformation of the aluminum matrix alone. Since aluminum constitutes most of the composite volume, this practically identical elastic behaviour of all samples can be expected. In the second stage, aluminum starts deforming plastically as can be seen with the unreinforced aluminum sample. At this point, load transfer from the aluminum matrix to the carbon fiber increasingly takes place and fibers take over more and more control over the composite bending strength. S12 with 40 MPa hydraulic pressure, as shown in Figure 6-5, shows a similar linear deformation state with a slightly weaker slope as compared to the elastic range in the first deformation stage. Then, the bending curves evolve into the third linear stage with stronger slope as most of the composite strength is provided by the fibers. For S12, a good interface bonding and improved load transfer result in the strain hardening modulus being significantly improved by up to 248.3% and can be seen as an effective extension of the elastic range with increased stiffness and yield strength. In contrast, in samples like S3, with incomplete infiltration and poor interface bonding, complete load transfer from the aluminum matrix to the fibers seems not to be achieved and load transfer remains partial. Therefore, the bending curve follows the trend of that for unreinforced aluminum, only with some increase in strength due to fiber reinforcement. At the end of the third stage, the S3 sample reaches its ultimate flexural strength point at a lower load level compared to the S12 sample. However, no drop in strength is observed until at higher deflections of around 10mm where the material strength drops slowly similar to unreinforced aluminum. In contrast, the S12 sample reaches the maximum strength level at higher load, but the strength drops rapidly after the peak when the pin pierces through the sample by shearing along its external circumference. This suggests that the flexural bend strength of G3 samples like S12 could be even higher than measured if this transverse shear failure at the loading pin does not take place. Also, the investigation of the samples after testing shows no cracking or interface debonding in the G3 samples with good interface adhesion as seen in Figure 4-5 (c). In contrast, extensive and rapid crack propagation was observed in the S3 sample with poor fiber-matrix interface bond. Cracks and fracture in the S3 sample were observed at the interface between aluminum and fiber fabric layers, which was accompanied by fiber pull-out as shown in Figure 4-5 (a).

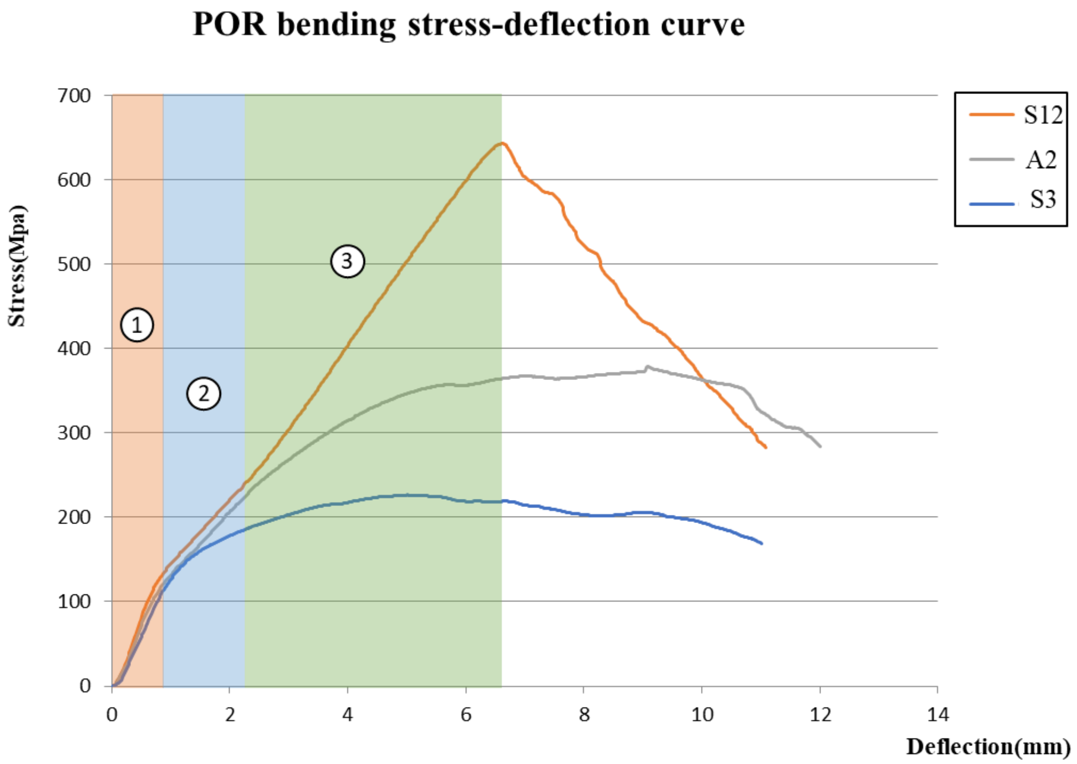

Figure 6-5: POR bending stress-deflection curves of S3 (4.55vol% fiber, short die, no post-processing); S12 (4.81vol% fiber, long die, 40 MPa post-processing); and A2 (unreinforced)

The results of this study agree with those of Junjia Zhang et al. who reported a 33.6% increase in bend strength in hot-pressed aluminum composites through the addition of plain weave PAN-based T300 carbon fiber [52]. They also observed a bending curve behavior similar with the results of this study with the fiber reinforcement playing a bigger role at high bending loads. Furthermore, Franziska Kachold et al. fabricated carbon fiber reinforced aluminum by high-pressure die casting. They achieved a maximum tensile strength of 155 MPa at 26.8% bidirectional PAN-based carbon fiber volume fraction. However, all their composite samples showed lower tensile strength and a shorter elastic region compared to the unreinforced aluminum matrix [53]. Their results agree rather with the S3 sample indicating that the samples may have contained extensive manufacturing defects and poor fiber-matrix interface bond. Junjia Zhang et al. disused the effect of fiber orientation on tensile stress-strain curves. Composites fabricated by semi-solid rolling showed a significant strength improvement. The ultimate tensile strength improved by 52% for 0/90^o composites (plain weave fabric fiber yarns oriented 0^o and 90^o with respect to the loading direction), and by 60% for 45^o composites (plain weave fabric fiber yarns oriented 45^o with respect to the loading direction). The sample plasticity of both fiber orientations was limited due to good interface bonding. However, the 0/90^o fiber orientation composites had a stress jump at the transition from elastic to plastic deformation, and the tensile stress increased sharply in the plastic region. They reported straightening of the woven fibers with increasing deformation and stress as carbon fibers carry more load before composite failure. For composites with 45^o fiber orientation, the tensile stress-strain curve was smoother and fiber strengthening showed stronger effect in the plastic region. Comparing with this study, piston-on-ring bend testing seems to yield an average performance resulting from two-dimensional plane loading in all directions. As a result, the stress-deflection curve is between those of the 0/90^o and 45^o fiber orientation [54]. As such, our study suggests that thermal expansion squeeze casting combined with hydraulic post-pressing yields samples with good load transfer between the carbon fiber and aluminum matrix, and therefore, can be expected to provide overall good quality composites with significantly improved stiffness and strength.

6.3 Effect of carbon fiber volume fraction

The composite mechanical properties are expected to improve with the addition of carbon fiber reinforcement based on the rule of mixture. However, the experimental results also show a detrimental effect at high carbon fiber volume fractions. This is primarily because the threshold pressure required for the liquid to infiltrate the fibers increases with the carbon fiber volume fraction. This threshold or critical pressure is described by the Young-Laplace equation (Equation (6-1)) that gives the relationship between the capillary pressure and the infiltration parameters as [55]

$$\mathrm{P}_c = S\gamma_{lv}cos\theta \text{ [55]} \tag{6-1}$$

Where P_c is the critical capillary pressure; S is the specific area of the preform which is equal to the ratio of the fiber-matrix interface to the matrix volume; γ_{lv} is the surface tension of the liquid; θ is the contact angle at the interface.

Considering an hexagonal packing of cylindrical fibers and the corresponding capillary pressure during liquid penetration as seen in Figure 6-6 [56], K. J. Ahn et al. derived the average critical pressure using Equation (6-2) and (6-3) [57].

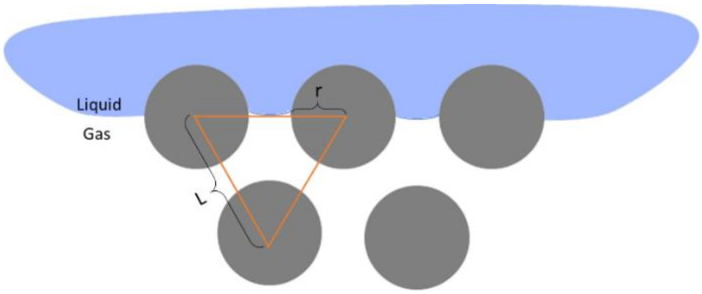

Figure 6-6: Schematic illustration of the capillary pressure during fiber infiltration [56]

$$S = \frac{2V_f}{r(1-V_f)} \text{ [57]} \tag{6-2}$$

$$\mathrm{P}_c = \frac{2\gamma_{lv}V_f cos\theta}{r(1-V_f)} \text{ [57]} \tag{6-3}$$

Where r is the radius of the carbon fibers and V_f is the carbon fiber volume fraction.

It is obviously from Equation (6-3) that the capillary pressure increases with carbon fiber volume fraction. In this study, the laminate composite structure results in a relatively high local carbon fiber volume fraction in the strengthened layers, which is 31.53vol%, 42.06vol% and 63.13vol%, respectively as estimated from the geometric modelling. Junjia Zhang et al. found that insufficient pressure during squeeze casting can result in considerable center crack defects at the fabric yarns, as shown Figure 6-7 [52]. The presence of un-infiltrated defects is extremely harmful to composite mechanical behaviors as they facilitate interlaminar crack propagation, resulting in premature composite failure and low composite strength.

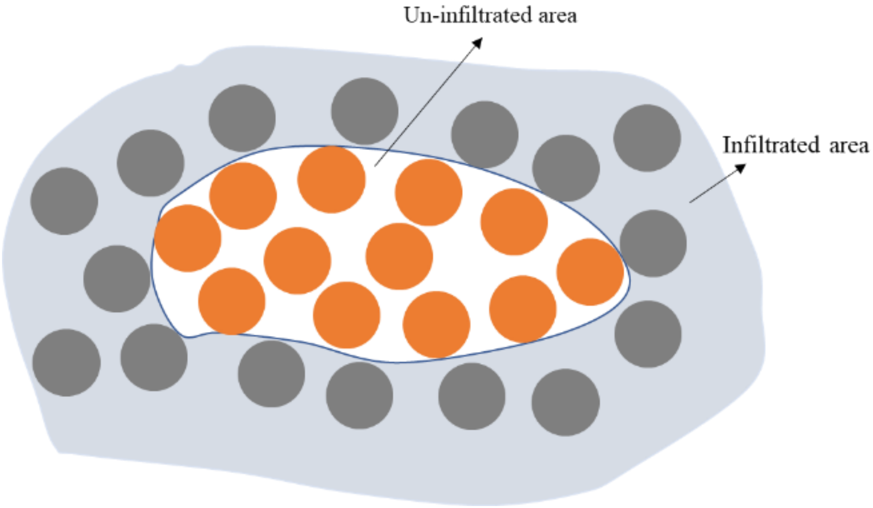

Figure 6-7: Un-infiltrated center crack defect [52]

The process group G1 (S1, S2, S3) is fabricated using the short casting die yielding low thermal expansion squeeze pressure. Therefore, sample S3 (4.55vol% total carbon fiber volume fraction) shows a dramatic drop in flexural young's modulus compared with S2 (3.08vol% total carbon fiber volume fraction). It means the applied pressure provided by the short casting die is insufficient for aluminum flow though the fabric when the total carbon fiber volume fraction is too high, in this case beyond 3.08vol%. The poor infiltration and low fiber-matrix bond are also reflected in extensive fiber pull-out observed on failed bend test samples. Franziska Kachold et al. reported a smooth tensile fracture surface at 8.9vol% carbon fiber volume fraction for carbon fiber reinforced aluminum composites fabricated by high-pressure die casting. However, they observed delamination and visible fiber pull-out when the fiber volume fraction increased to 26.8%. They concluded that excessively high carbon fiber volume fraction results in insufficient infiltration and poor interface bonding [53].

Composites fabricated using the long casting die with post-processing (G3 and G4 groups) show a continuous increase in the flexural modulus as the carbon fiber volume fraction increases. The enhanced external pressure achieved with the long die and post-processing pressing are efficient in enabling molten aluminum to overcome the infiltration threshold pressure. For the flexural strength performance, all groups first show an increase in strength with increasing carbon fiber volume fraction, but then the strength drops at high fiber contents due to increased defect concentration and poor interface bonding. Anil Alten et al. presented a similar result with Ni-coated carbon fiber reinforced 6063-aluminum alloy. When the carbon fiber volume fraction increased from 2vol% to 4vol%, the bend strength dropped by 13.5% and 10% with 0.9 µm and 4.2 µm thick fiber coatings, respectively [58]. Moreover, the composites with lower carbon fiber content showed slightly higher values of young's modulus.

In summary, this research shows that carbon fiber addition can improve the composite flexural modulus and the flexural strength. However, while an optimised fabrication method enabled to further increase the young's modulus up to fiber contents above 4.81vol%, the flexural strength consistently dropped beyond a critical fiber volume fraction. Comparing all experiment results, the original plain weave carbon fiber fabric (4.81vol% fiber) yielded the highest flexural modulus and yield strength, while samples with 25% (3.55vol% fiber) reduced fiber density resulted in the highest flexural strength.

6.4 Effect of squeeze casting pressure

Figure 6-8 shows the flexural modulus and flexural yield strength after 25% reduction in carbon fiber volume fraction compared to the initial plain weave fiber fabric. This reduction in carbon fiber content yielded a carbon fiber volume fraction between 2.79vol% and 3.70vol%

and produced the highest stiffness and strength values at all investigated squeeze casting pressures. The S11 sample with 3.55vol% averaged carbon fiber content fabricated using the long die and 40 MPa post-processing pressure yielded the overall best results with the highest flexural modulus of 73.8 GPa and the highest flexural yield strength of 178.0 MPa. For the S14 sample with a similar carbon fiber content obtained at a lower post-processing pressure of 20 MPa, the flexural modulus drops to 69.09 GPa and the flexural yield strength is significantly reduced by 41% compared with S11 to 125.9 MPa. This illustrates the role of the squeeze pressure as one of the most important process parameters for carbon fiber reinforced aluminum matrix composites. The squeeze pressure crucially determines fiber wettability by molten aluminum and defines the quality of interface bonding. Complete infiltration and high-quality interface bond are critical to achieving high flexural modulus and strength. The contact angle is reduced under sufficient squeeze pressure to achieve better wetting and larger bonding area, while reducing porosity and stress concentrations at the fiber-matrix interface. However, excessively high squeeze pressures can also induce carbon fiber fracture and decomposition leading to enhanced interface reactions, which can result in sample delamination as observed on samples fabricated at 90 MPa post-processing pressure. This phenomenon is also reported by E. Hajjari et al. who observed a decrease in composite tensile strength from 492 MPa to 376 MPa, when the squeeze casting pressure increased from 30 MPa to 70 MPa [59]. The strong effect of post-processing hydraulic pressing observed in this study can be explained as follow: Firstly, it compensates thermal expansion pressure loss as the die inserts cool and shrink during cooling. This helps eliminate shrinkage porosity and close un-infiltrated cracks. Secondly, it compensates for aluminum shrinkage as it solidifies to prevent separation of aluminum from the carbon fiber. This improves interface bonding by maintaining intimate contact between carbon fiber and aluminum during cooling and solidification. Thirdly, high post-processing pressure maintained during complete solidification prevents the creation of microporosity by pressing out potential gases from molten aluminum and seal material, which reduces defects in the final composite samples. This is in agreement with Junjia Zhang et al. who found that 6vol% compression by hot-pressing can efficiently improve the fiber/matrix interface bonding. However they also observed significant interface delamination and fiber debonding when the post-pressing pressure was increased to achieve 15vol% compaction [52].

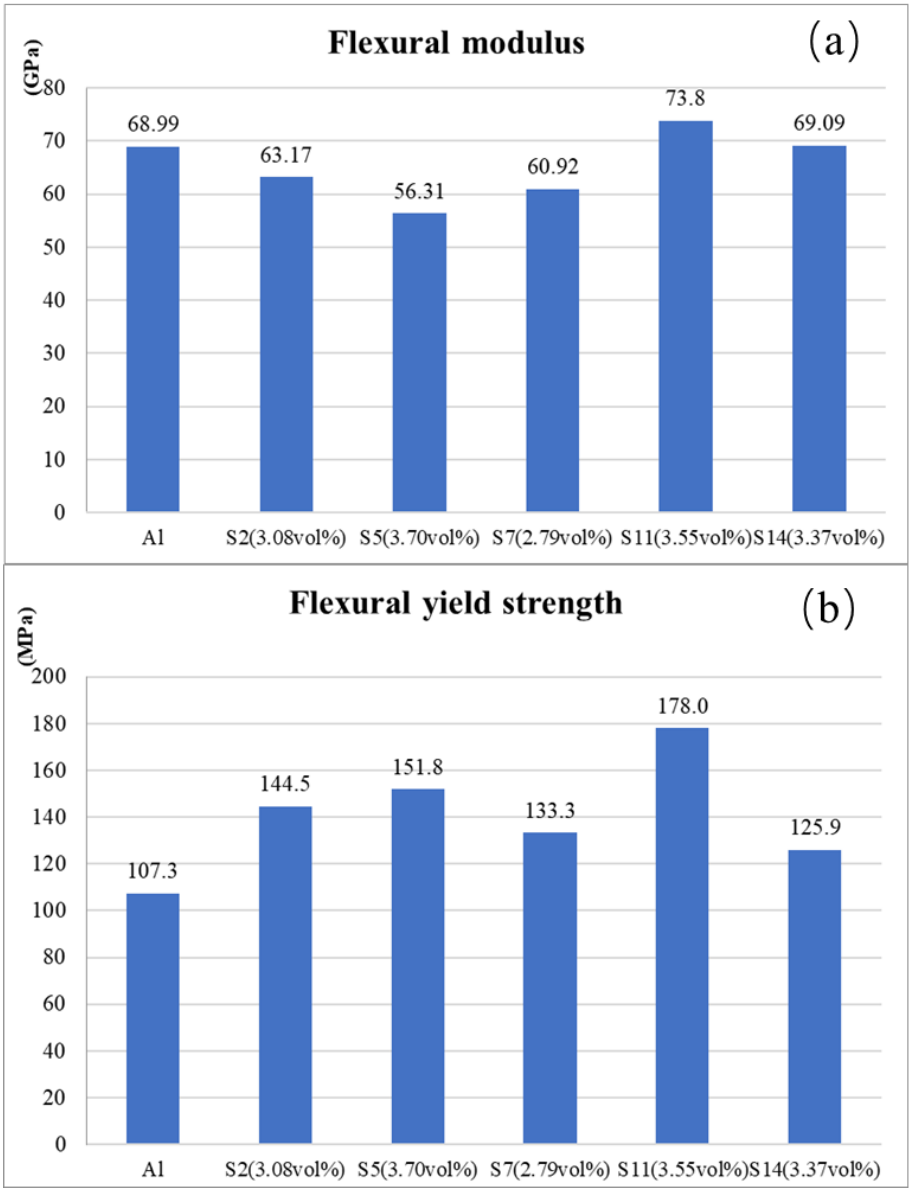

Figure 6-8: (a) Flexural modulus and (b) flexural yield strength of composites with 25% reduction in carbon fiber content compared to plain weave fiber fabric

The results of this study also show that the composite mechanical performance is sensitive to the squeeze cast atmosphere. As the aluminum and fiber fabric disks in S4 to S8 samples were cut smaller that the inner die diameter, they left space for air to fill. This air left between the aluminum disk and die wall seems to infiltrate into the molten matrix and induce gas porosity in the composites. In addition, this air can considerably oxidise molten aluminum and carbon fiber at the high squeeze cast temperature around 800℃. Consequently, these samples show significantly inferior mechanical properties compared to samples where aluminum disks were cut to slide fit into the inner diameter of the die, leaving less space for air enclosure inside the die.

6.5 Impact of squeeze casting temperature and thermal effects

The thermal property mismatch between the reinforcement and matrix has a significantly influence on the composite mechanical performance. The thermal conductivity of carbon fiber is 6.83 W/m-ºK, which is much smaller than 167 W/m-K for the 6061-aluminum matrix. When the reinforcement and matrix start to cool from the casting temperature, the temperature within the fibers can gradually become higher than in their surrounding matrix. Consequently, aluminum around the carbon fibers tends to remain longer in liquid form and to become the last solidification regions. As a result, defects and residual stresses generally aggregate around the fiber/matrix interfaces. Therefore, higher carbon fiber volume fractions and longer cooling times can lead to more defect formation at the interface during cooling, leading to overall deteriorated mechanical properties [52].

On the other hand, as previously mentioned, the thermal expansion of carbon fiber is constantly smaller at all processing temperature. At the same time, the aluminum matrix, with the larger coefficient of thermal expansion, shrinks significantly more during solidification and cooling. Consequently, substantial thermal stresses can arise in the composites as they cool from the relatively high processing temperature of 800°C down to room temperature. The thermal stresses can cause carbon fiber/matrix interface debonding after cooling. Moreover, aluminum carbide formation contributes to thermal stress build-up at fiber/matrix interfaces as reported by H. Nayeb-Hashemi et al.. [60], which can exacerbate fiber pull-out and interface debonding [61].

In this study, samples were held at 800 °C for 40 mins, subjected to squeeze pressure and then the die was cooled relatively slowly in air. As thermal stresses within composites do not only depend on the thermal expansion mismatch between composite constituents, but also on the overall processing temperature, it can be expected that lower casting temperature and shorter cooling times could contribute to achieving stronger interface bonding.

6.6 Effect of interface shear strength

During the piston-on-ring bending tests, the interlamellar shear stresses rise with the applied load. For unreinforced aluminum, the tested samples deformed continuously under bend loading and there are no shear cracks observed due to high shear strength. However, some carbon fiber reinforced composites exhibited both well bonded fibers and fibers that were not bonded to the aluminum matrix due to uncompleted infiltration. The unbonded fibers do not contribute to the composite stiffness and strength. Instead, cavities build up at their interface with the matrix from which fracture starts, leading to premature shear failure at a low bending stress. Other composite samples showed good interfacial shear strength resulting in an overall sharp fracture along the composite thickness with not fiber pull-out or interlamellar shear fracture, especially for samples with post-processing pressing. As POR bend testing was used, it is difficult to identify differences between the interlamellar shear strength and the interface bond quality in different directions. Therefore, only an overall critical interfacial shear strength can be determined that is necessary for full load transfer between the aluminum matrix and the carbon fibers before failure.

For example, S11 and S12 samples, with 3.55vol% and 4.81vol% of carbon fibers, respectively, and fabricated with the long die followed by 40 MPa post-pressing, show good stiffness. This means most fibers in the two samples are well bonded to the matrix, and only a few unbonded fibers may still exist. However, the S12 sample with the original plain weave carbon fiber density failed before reaching the predicted ultimate strength, while S11 failed above the predicted ultimate strength. This means the higher carbon fiber content in S12 samples produces poorer interfacial shear strength, while the lower carbon fiber content in the S11 samples proves to be best with respect to both interface bond strength and composite strength.

FEA modelling predicts higher composite shear strength values than the ANA model, with the best experimental sample S11 exhibiting higher bend strength than predicted by the two modelling approaches. FEA predicts critical interfacial shear strengths of 40.52 MPa and 64.27 MPa for S10 and S11 samples, respectively, which is reached at the ultimate bend load.

Interdiffusion between carbon fibers and aluminum matrix can result in a strong interface bond strength. In this ideal case, the interfacial shear strength would not affect composite failure, as failure would take place across the matrix and the reinforcement. However, no prefect bonding was achieved in the current composites due to imperfect wettability, manufacturing defects, potentially detrimental chemical reactions and other defects at the fiber-matrix interface [34]. In this aspect, sufficient squeeze pressure achieved with the long die and post-processing pressing proves to be able to improve fiber/matrix interface bonding. Other manufacturing parameters, such as casting temperature and holding time, can equally be optimised for improved interfacial shear strength [27][62].

The contact angle of Al on the carbon fiber decreases with temperature and holding duration. It is also strongly affected by aluminum carbide formation at the interface as illustrated in Figure 6-9 [33]. As interface reaction products grow, Al increasingly wets the created aluminum carbide layer instead of the carbon fibers themselves, potentially leading to overall improved infiltration and interface strength. However, excessive levels of interface reaction can also result in brittle, unstable and detrimental interface reaction products. For example, needle shaped aluminum carbides can grow into the surrounding aluminum matrix and damage the carbon fiber surface, which can induce interface cracks. Moreover, aluminum carbides are sensitive to moisture, which can lead to further reactions as described in Equation (6-4). Also, T. Etter et al. found that the degradation of aluminum carbides can lead to their breakage in ambient conditions, creating interface defects and leaving large cavities at graphite/aluminum interfaces [41].

$$\mathrm{Al_4C_3} + 12\mathrm{H_2O} \rightarrow 4\mathrm{Al(OH)_3} + 3\mathrm{CH_4}.[41] \qquad (6\text{-}4)$$

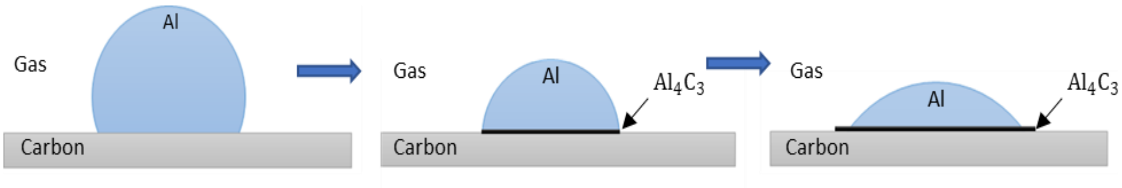

Figure 6-9: Aluminum carbide formation during the wetting process [33]

Hence, only a proper amount of reaction is appropriate for achieving strong interface bonding. In this study, all samples are fabricated at 800°C and this temperature is maintained for 40 mins prior to cooling. Increasing the casting temperature and time is a possible way to improve the wettability and the interfacial shear strength.

7 CONCLUSION

Squeeze casting using thermal expansion pressure and post-processing with hydraulic pressing successfully fabricated carbon fiber fabric reinforced aluminum matrix composites. The following conclusions can be drawn from the study that included experimental sample fabrication and mechanical testing, as well as analytical and finite element modelling:

- Improved mould design with thermal expansion inserts provide adequate initial pressure during heating, helping reduce air presence and oxidation of the composite laminates. Post-pressing during cooling compensates for the shrinkage of composite sample and die components during solidification, which achieves reduced porosity and significantly improved fiber-matrix bond.
- However, excessive pressure during squeeze casting can cause fiber damage and promote detrimental chemical reactions at the fiber-matrix interface, which can result in poor mechanical properties and brittle composite failure.
- POR bend testing shows that the flexural modulus, yield strength and strain hardening modulus increase continuously with the carbon fiber volume fraction up to the maximum tested value of 4.81vol%. At 4.81vol% carbon fiber volume fraction, the flexural modulus and strain hardening modulus increase by 11.6% and 248.3%, respectively, while the yield strength increases by 90.1% compared to the unreinforced reference 6061 aluminum alloy squeeze casted under identical conditions. The mechanical strength improvement of carbon fiber reinforcement is primarily reflected in the high stress region.
- For samples fabricated with 40 MPa post-processing pressure, the predictions of the ANA and FEA models match well with experiment results at low carbon fiber volume fractions, suggesting that the samples have a near-ideal defect free fiber-matrix interface bond as

assumed in the models. As such, the flexural modulus and strength continuously increase with fiber volume fraction.

- In contrast, modeling results suggest compromised mechanical performance at high carbon fiber volume fraction and for samples fabricated with lower post-processing squeeze pressures. This is due to high defect concentrations, such as porosity, which substantially weaken the interface bond, leading to interlayer delamination and premature failure of the composite.
- POR bend testing shows that the composite shear strength is determined by the interlamellar shear strength. A weak interface shear strength results in composites failure before reaching the theoretical ulitmate flexural strength as estimated from the models. In contrast, experimental results show that the effect of the interface shear strength on the flexural modulus is minor.
- The poor ultimate flexural strength observed at high carbon fiber volume fraction is due to high defect concentrations, such as porosity, which substantially weaken the interface bond, leading to interlayer delamination and premature failure of the composite.

8 OUTLOOK

The present study mainly focuses on optimizing the squeeze casting process, improving fiber/matrix interface bonding and developing models to better described the composite behaviour and failure. Future research and development could target further maximizing fiber strengthening for achieving composites with even higher stiffness, strength and toughness. Specific suggestions are listed as follows:

- Increasing the carbon fiber content. In the current work, the overall carbon fiber volume fraction is considerably low. Higher squeeze casting pressure and better liquid fluidity could help overcome flow resistance to improve infiltration and wetting during squeeze casting.
- Improving fiber/matrix interface wettability and reducing interface chemical reactions. This can be achieved through fiber surface modifications such as metallic coating on the carbon fibers. Preliminary trials successfully produced copper coatings on plain weave AS4 Hexcel carbon fiber. Furthermore, shortening the heating, holding and cooling times during squeeze casting could help reduce aluminum carbide formation. Moreover, using a protective atmosphere such as vacuum or argon gas could contribute to reduce oxidation, improve fluidity and minimise gas evolution and pore formation.
- Investigating the effect of thermal stress on composite properties. Specifically, potential residual stresses in the composite samples may contribute to their failure. If so, applying appropriate post-processing solution and aging heat treatments could help further improve the interface structure and final mechanical properties.
- Designing fiber arrangements and different fiber fabric weave structures to optimise in-plane mechanical properties. In fact, simulations and literature suggest that the in-plane

properties are lowest at 45° from the two normal fiber alignment directions in the used plain weave fiber fabric. As such, improving properties in these 45° directions could yield overall better composite performance.

- Studying the effects of manufacturing defects on composite mechanical properties and failure mechanisms more in-depth in order to better identify weaknesses and develop more targeted improvement solutions.

REFERENCES

[1] T. Schubert, B. Trindade, T. Weißgärber, and B. Kieback, "Interfacial design of Cu-based composites prepared by powder metallurgy for heat sink applications," *Mater. Sci. Eng. A*, vol. 475, no. 1–2, pp. 39–44, 2008.

[2] G. Necker and W. Mader, "Characterization of ag/cdo interfaces," *Philos. Mag. Lett.*, vol. 58, no. 4, pp. 205–212, 1988.

[3] S.-J. Park, "History and structure of carbon fibers," in *Carbon Fibers*, Springer Science, 2018, p. 18.

[4] B. A. Newcomb and H. G. Chae, "The properties of carbon fibers," in *Handbook of Properties of Textile and Technical Fibres*, Elsevier Ltd., 2018, pp. 841–871.

[5] S. C. Bennett, D. J. Johnson, and W. Johnson, "Strength-structure relationships in PAN-based carbon fibres," *J. Mater. Sci.*, vol. 18, no. 11, pp. 3337–3347, 1983.

[6] K. Acatay, "Carbon fibers," in *Fiber Technology for Fiber-Reinforced Composites*, Elsevier Ltd, 2017, pp. 123–151.

[7] K. Sagisaka and A. Kondo, "Hollow structured porous carbon fibers with the inherent texture of the cotton fibers," *Chem. Phys. Lett.*, vol. 710, pp. 118–122, 2018.

[8] M. Smith, "New developments in carbon fiber," *Reinf. Plast.*, vol. 62, no. 5, pp. 266–269, 2017.

[9] S. Chand, "Carbon fibers for composites," *J. Mater. Sci.*, vol. 35, no. 6, pp. 1303–1313, 2000.

[10] V. Jiménez, P. Sánchez, and A. Romero, "Materials for activated carbon fiber synthesis," in *Activated Carbon Fiber and Textiles*, Elsevier Ltd., 2016, pp. 21–38.

[11] M. S. A. Rahaman, A. F. Ismail, and A. Mustafa, "A review of heat treatment on

polyacrylonitrile fiber," *Polym. Degrad. Stab.*, vol. 92, no. 8, pp. 1421–1432, 2007.

[12] F. K. Wang, "Carbon fibers and their thermal transporting properties," in *Thermal Transport in Carbon-Based Nanomaterials*, 1st ed., Elsevier Inc., 2017, pp. 135–184.

[13] M. G. Huson, *High-performance pitch-based carbon fibers*. Elsevier Ltd., 2016.

[14] T. Ishikawa and T.-W. Chou, "Stiffness and strength behaviour of woven fabric composites," *J. Mater. Sci.*, vol. 17, no. 11, pp. 3211–3220, 1982.

[15] X. Tang, J. D. Whitcomb, A. D. Kelkar, and J. Tate, "Progressive failure analysis of 2 × 2 braided composites exhibiting multiscale heterogeneity," *Compos. Sci. Technol.*, vol. 66, no. 14, pp. 2580–2590, 2006.

[16] B. K. Behera and P. K. Hari, "The basics of woven fabric structure," in *Woven Textile Structure*, Woodhead Publishing Limited, 2010, pp. 3–8.

[17] J. Whitcomb and X. Tang, "Effective moduli of woven composites," *J. Compos. Mater.*, vol. 35, no. 23, pp. 2127–2144, 2001.

[18] P. K. Hari, "Types and properties of fibres and yarns used in weaving," *Woven Text. Princ. Technol. Appl.*, pp. 3–34, 2012.

[19] N. Chawla and K. K. Chawla, "Matrix materials," in *Metal Matrix Composites*, Springer science, 2013, pp. 45–46.

[20] J. Davis, "Aluminum and aluminum alloys introduction," in *Alloying: Understanding the Basics*, ASM International, 2001, pp. 192–203.

[21] M. V. Glazoff and A. V. Khvan, "Phase diagrams for binary and multicomponent aluminum systems," in *Casting Aluminum Alloys.*, Elsevier Ltd., 2019, pp. 1–10.

[22] D. S. MacKenzie, "Heat treatment of aluminum alloys," *Ind. Heat.*, vol. 71, no. 12, p. 29, 2004.

[23] V. S. Zolotorevsky, N. A. Belov, and M. V. Glazoff, “Influence of heat treatment upon microstructure of casting aluminum alloys,” in *Casting Aluminum Alloys*, Elsevier Ltd., 2019, pp. 236–301.

[24] L. Ceschini, A. Morri, A. Morri, S. Toschi, S. Johansson, and S. Seifeddine, “Effect of microstructure and overaging on the tensile behavior at room and elevated temperature of C355-T6 cast aluminum alloy,” *Mater. Des.*, vol. 83, pp. 626–634, 2015.

[25] M. Dhanashekar and V. S. Senthil Kumar, “Squeeze casting of aluminium metal matrix composites - An overview,” *Procedia Eng.*, vol. 97, no. January 2015, pp. 412–420, 2014.

[26] T. R. Vijayaram, S. Sulaiman, A. M. S. Hamouda, and M. H. M. Ahmad, “Fabrication of fiber reinforced metal matrix composites by squeeze casting technology,” *J. Mater. Process. Technol.*, vol. 178, no. 1–3, pp. 34–38, 2006.

[27] A. A. Moosa, K. K. Al-khazraji, and O. S. Muhammed, “Tensile strength of squeeze cast Carbon fibers reinforced Al-Si matrix composites,” *J. Miner. Mater. Charact. Eng.*, vol. 10, no. 2, pp. 127–141, 2011.

[28] J. Hashim, L. Looney, and M. S. J. Hashmi, “Metal matrix composites: production by the stir casting method,” *J. Mater. Process. Technol.*, vol. 92–93, pp. 1–7, 1999.

[29] S. Naher, D. Brabazon, and L. Looney, “Simulation of the stir casting process,” *J. Mater. Process. Technol.*, vol. 143–144, no. 1, pp. 567–571, 2003.

[30] I. A. Ibrahim, F. A. Mohamed, and E. J. Lavernia, “Particulate reinforced metal matrix composites - a review,” *J. Mater. Sci.*, vol. 26, no. 5, pp. 1137–1156, 1991.

[31] M. Rahimian, N. Ehsani, N. Parvin, and H. R. Baharvandi, “The effect of particle size, sintering temperature and sintering time on the properties of Al-Al2O3 composites,

made by powder metallurgy," *J. Mater. Process. Technol.*, vol. 209, no. 14, pp. 5387–5393, 2009.

[32] A. Mortensen and J. Llorca, "Metal matrix composites," *Annu. Rev. Mater. Res.*, vol. 40, no. 1, pp. 243–270, 2010.

[33] B. A. O. Sarina, T. Kai, A. Kvithyld, T. Engh, and M. Tangstad, "Wetting of pure aluminium on graphite , SiC and Al2O3 in aluminium filtration," *Trans. Nonferrous Met. Soc. China*, vol. 22, no. 8, pp. 1930–1938, 2012.

[34] V. D. Scott, R. L. Trumper, and M. Yang, "Interface microstructures in fibre-reinforced aluminium alloys," *Compos. Sci. Technol.*, vol. 42, no. 1–3, pp. 251–273, 1990.

[35] R. Mogilevsky and S. R. Bryanb, "Reactions at the matrix / reinforcement interface in aluminum alloy matrix composites," *Mater. Sci. Eng. A*, vol. 191, no. 1–2, pp. 209–222, 1995.

[36] H. Ribes, M. Sultry, G. L. E. Rance, and J. G. Legoux, "Microscopic examination of the interface region in 6061-AI / SIC composites reinforced with as-received and oxidized SiC particles," *Metall. Trans. A*, vol. 21, no. 9, pp. 2489–2496, 1990.

[37] C. G. Levi, G. J. Abbaschian, and R. Mehrabian, "Interface interactions during fabrication of aluminum alloy-alumina fiber composites," *Metall. Trans. A*, vol. 9A, no. 5, pp. 697–711, 1978.

[38] Y. Nishida, "Introduction to MMCs," in *Journal of Chemical Information and Modeling*, CORONA PUBLISHING CO., LTD., 2013, pp. 4–5.

[39] B. J. Dalgleish, E. Saiz, A. P. Tomsia, R. M. Cannon, and R. O. Ritchie, "Interface formation and strength in ceramic-metal systems," *Scr. Metall. Mater.*, vol. 31, no. 8, pp. 1109–1114, 1994.

[40] A. Mechanics, “Carbide formation in aluminium — carbon fibre-reinforced composites,” *J. Mater. Sci.*, vol. 32, pp. 5413–5417, 1997.

[41] T. Etter and P. Schulz, “Aluminium carbide formation in interpenetrating graphite/aluminium composites,” *Mater. Sci. Eng. A*, vol. 448, no. 1–2, pp. 1–6, 2007.

[42] V. Bharath, M. Nagaral, V. Auradi, and S. A. Kori, “Preparation of 6061Al-Al2O3 MMC‘s by stir casting and evaluation of mechanical and wear properties,” *Procedia Mater. Sci.*, vol. 6, pp. 1658–1667, 2014.

[43] A. H. Naronikar, “Optimizing the heat treatment parameters of Al-6061 required for better formability,” *Mater. Today Proc.*, vol. 5, no. 11, pp. 24240–24247, 2018.

[44] F. Ozturk, A. Sisman, S. Toros, S. Kilic, and R. C. Picu, “Influence of aging treatment on mechanical properties of 6061 aluminum alloy,” *Mater. Des.*, vol. 31, no. 2, pp. 972–975, 2010.

[45] M. Herráez, D. Mora, F. Naya, C. S. Lopes, C. González, and J. Llorca, “Transverse cracking of cross-ply laminates : A computational micromechanics perspective,” *Compos. Sci. Technol.*, vol. 110, pp. 196–204, 2015.

[46] “ISO 6872:2015 Dentistry—ceramic materials,” *International Standards Organization*, pp. 1–28, 2015.

[47] G. Pe, T. Bause, and J. Malzbender, “Ring-on-ring testing of thin, curved bi-layered materials,” *J. Eur. Ceram. Soc.*, vol. 31, pp. 2037–2042, 2011.

[48] S. Lee, J. Byun, and S. Hyung, “Effect of fiber geometry on the elastic constants of the plain woven fabric reinforced aluminum matrix composites,” *Mater. Sci. Eng. A347*, vol. 347, pp. 346–358, 2003.

[49] Y. J. You, J. H. J. Kim, K. T. Park, D. W. Seo, and T. H. Lee, “Modification of rule of

mixtures for tensile strength estimation of circular GFRP rebars,” *Polymers (Basel).*, vol. 9, no. 12, 2017.

[50] R. Younes, A. Hallal, F. Fardoun, and F. H. Chehade, “Comparative review study on elastic properties modeling for unidirectional composite materials,” in *Composites and Their Properties*, 2012, pp. 391–408.

[51] C. W. Huang and C. H. Hsueh, “Piston-on-three-ball versus piston-on-ring in evaluating the biaxial strength of dental ceramics,” *Dent. Mater.*, vol. 27, no. 6, pp. e117–e123, 2011.

[52] J. Zhang, S. Liu, Y. Lu, Y. Dong, and T. Li, “Fabrication process and bending properties of carbon fibers reinforced Al-alloy matrix composites,” *J. Mater. Process. Tech.*, vol. 231, pp. 366–373, 2016.

[53] F. Kachold and R. Singer, “Mechanical properties of carbon fiber-reinforced aluminum manufactured by high-pressure die casting,” *J. Mater. Eng. Perform.*, vol. 25, no. 8, pp. 3128–3133, 2016.

[54] J. Zhang, J. Liu, Y. Lu, Y. Liu, and T. Li, “Infiltration behavior and mechanism in semi-solid rolling of carbon fibers reinforced Al-matrix composite,” *Mater. Des.*, vol. 182, p. 108102, 2019.

[55] J. Guan, L. Qi, J. Liu, J. Zhou, and X. Wei, “Threshold pressure and infiltration behavior of liquid metal into fibrous preform,” vol. 23, pp. 3173–3179, 2013.

[56] G. Kaptay, “The threshold pressure of infiltration into fibrous preforms normal to the fibers ’ axes,” *Compos. Sci. Technol.*, vol. 68, pp. 228–237, 2008.

[57] J. C. Berg, “Simultaneous measurements of permeability and capillary,” *Polym. Compos.*, vol. 12, no. 3, pp. 146–152, 1991.

[58] D. Dispinar and E. Erzi, “Production and mechanical characterization of Ni-coated carbon fibers reinforced Al-6063 alloy matrix composites,” *J. Alloys Compd.*, vol. 787, pp. 543–550, 2019.

[59] E. Hajjari, M. Divandari, and A. R. Mirhabibi, “The effect of applied pressure on fracture surface and tensile properties of nickel coated continuous carbon fiber reinforced aluminum composites fabricated by squeeze casting,” *Mater. Des.*, vol. 31, no. 5, pp. 2381–2386, 2010.

[60] J. Seyyedi, “Study of the interface and its effect on mechanical properties of continuous graphite fiber-reinforced 201 aluminum,” *Metall. Trans. A*, vol. 20, pp. 727–739, 1989.

[61] Z. Yun-he and W. U. Gao-hui, “Interface and thermal expansion of carbon fiber reinforced aluminum matrix composites,” *Trans. Nonferrous Met. Soc. China*, vol. 20, no. 11, pp. 2148–2151, 2010.

[62] S. Li, C. Chao, and A. S. Morphologies, “Effects of carbon fiber/Al interface on mechanical properties of carbon-fiber-reinforced aluminum-matrix composites,” *Metall. Mater. Trans. A*, vol. 35, pp. 2153–2160, 2004.

Appendix I: POR Bending stress-strain curves

Table A1: POR bending properties of S1

Sample Ref.	Thickness(mm)	Flexural modulus (GPa)	Flexural yield strength (MPa)	Strain Hardening Modulus (GPa)	Flexural Strength (MPa)
S1	4.58	31.34	74.70	18.37	213.5

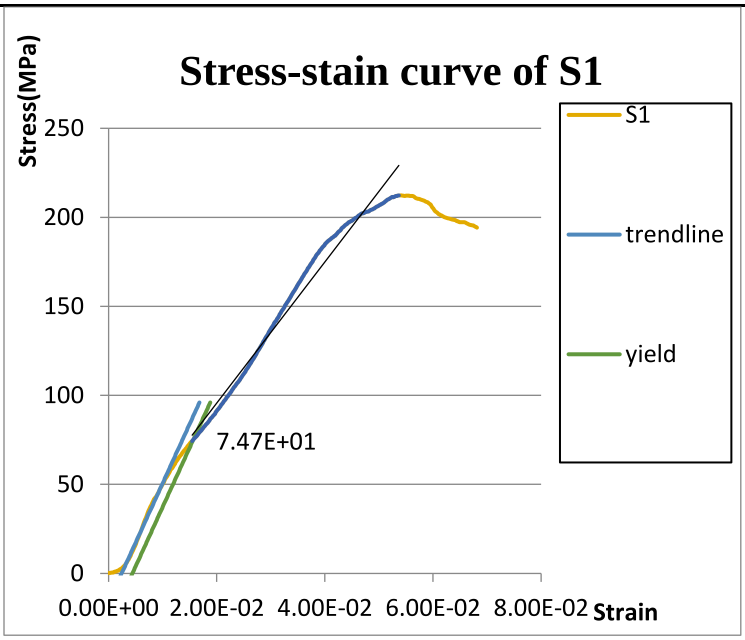

Figure A1: POR bending stress-strain of S1

Table A2: POR bending properties of S2

Sample Ref.	Thickness(mm)	Flexural modulus (GPa)	Flexural yield strength (MPa)	Strain Hardening Modulus (GPa)	Flexural Strength (MPa)
S2	4.8	72.3988	150.52	8.88159	278
	4.75	53.9419	138.54	7.48804	203.3

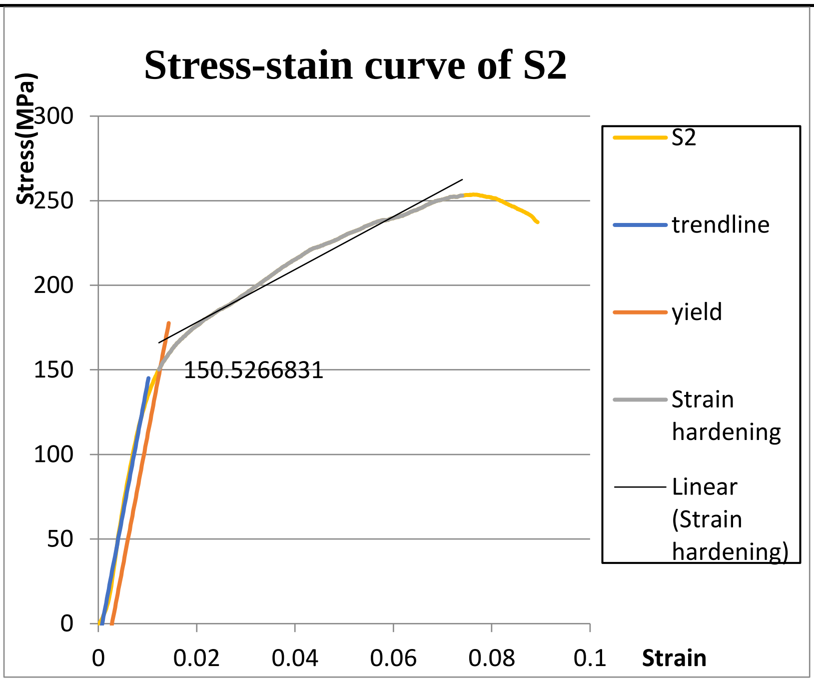

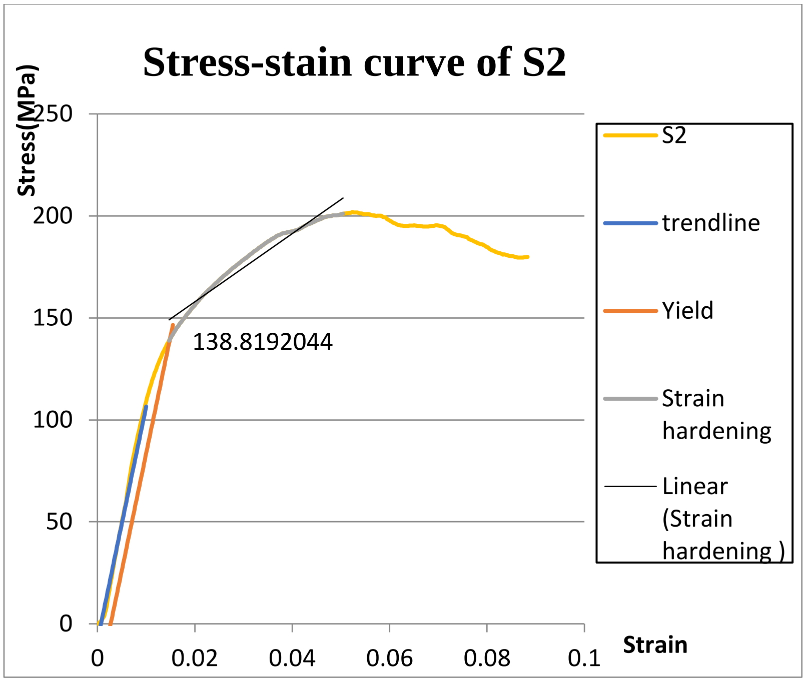

Figure A2: POR bending stress-strain of S2

Table A3: POR bending properties of S3

Sample Ref.	Thickness (mm)	Flexural modulus (GPa)	Flexural yield strength (MPa)	Strain Hardening Modulus (GPa)	Flexural Strength (MPa)
S3	4.53	27.1566	85.26	11.10986	173.1
	4.54	55.0746	127.04	8.01068	224.1

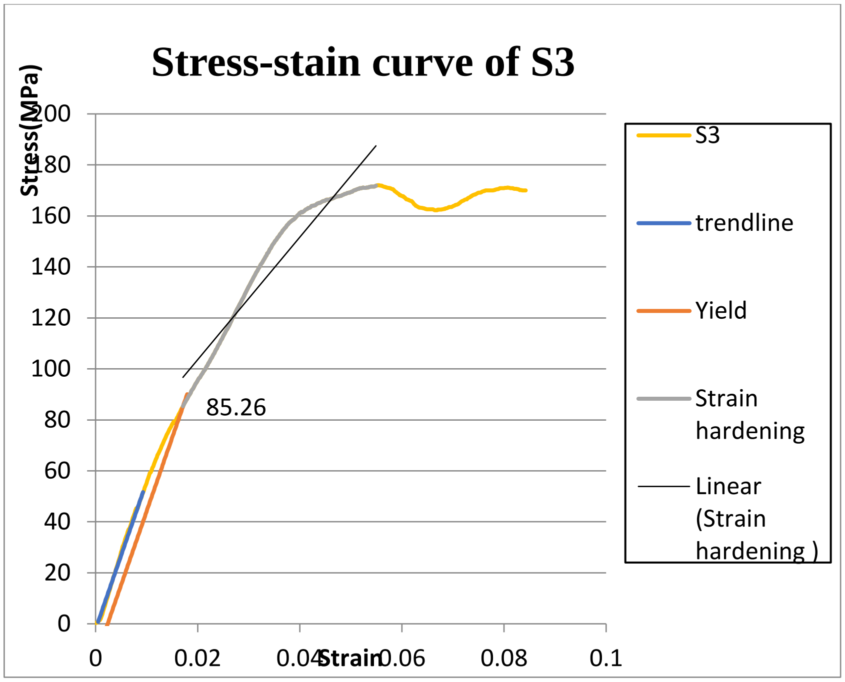

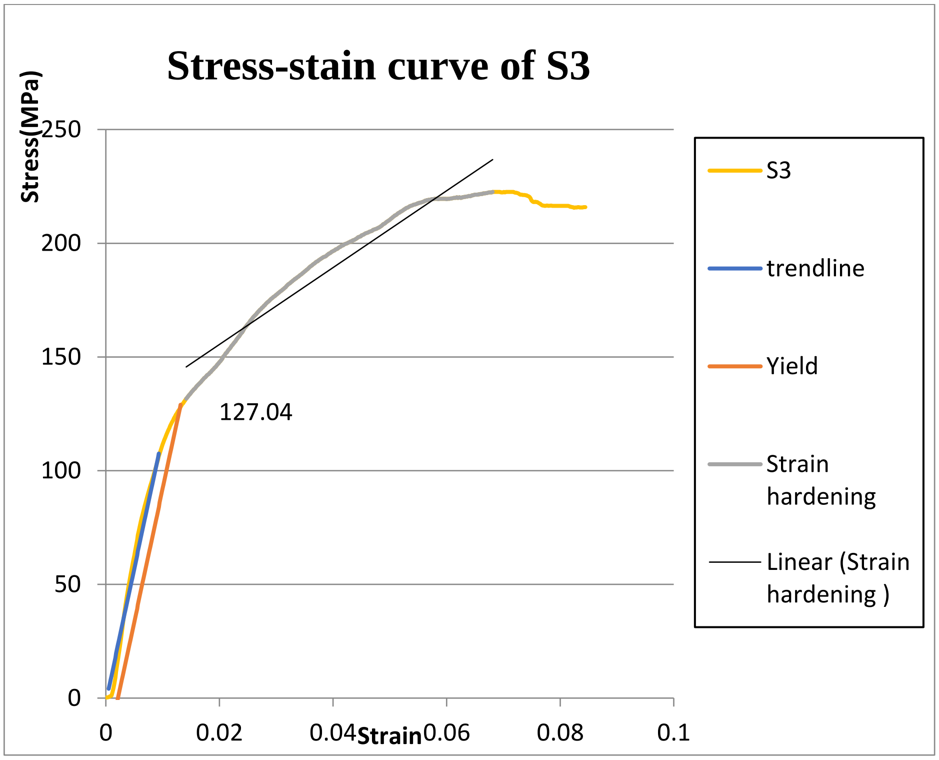

Figure A3: POR bending stress-strain of S3

Table A4: POR bending properties of S4

Sample Ref.	Thickness(mm)	Flexural modulus (GPa)	Flexural yield strength (MPa)	Strain Hardening Modulus (GPa)	Flexural Strength (MPa)
S4	6.35	41.1767	107.3	5.2532	157.2

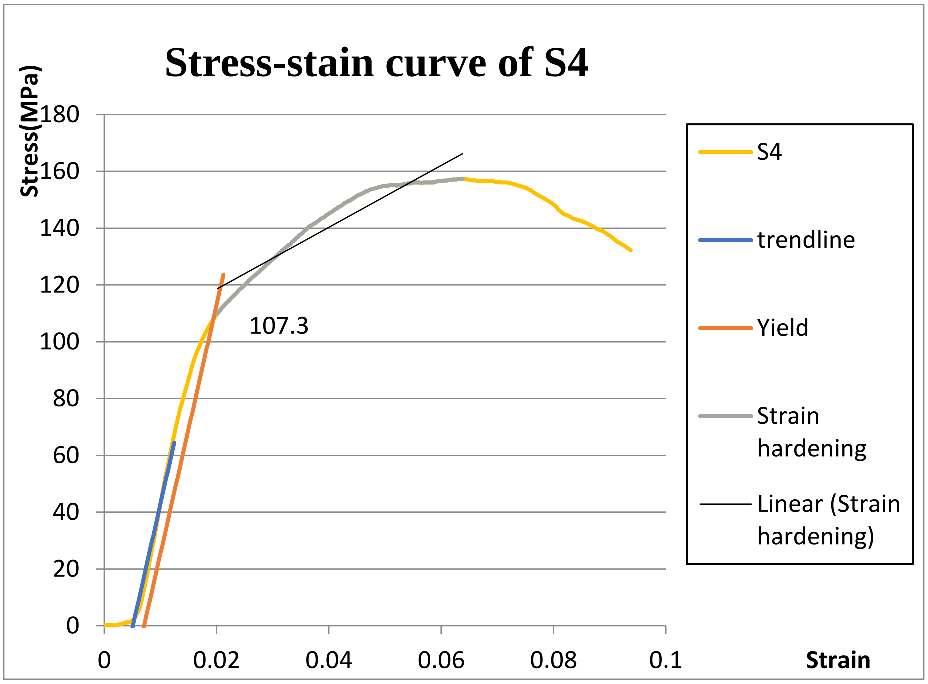

Figure A4: POR bending stress-strain of S4

Table A5: POR bending properties of S5

Sample Ref.	Thickness(mm)	Flexural modulus (GPa)	Flexural yield strength (MPa)	Strain Hardening Modulus (GPa)	Flexural Strength (MPa)
S5	6.10	56.306	151.8	15.337	228.3

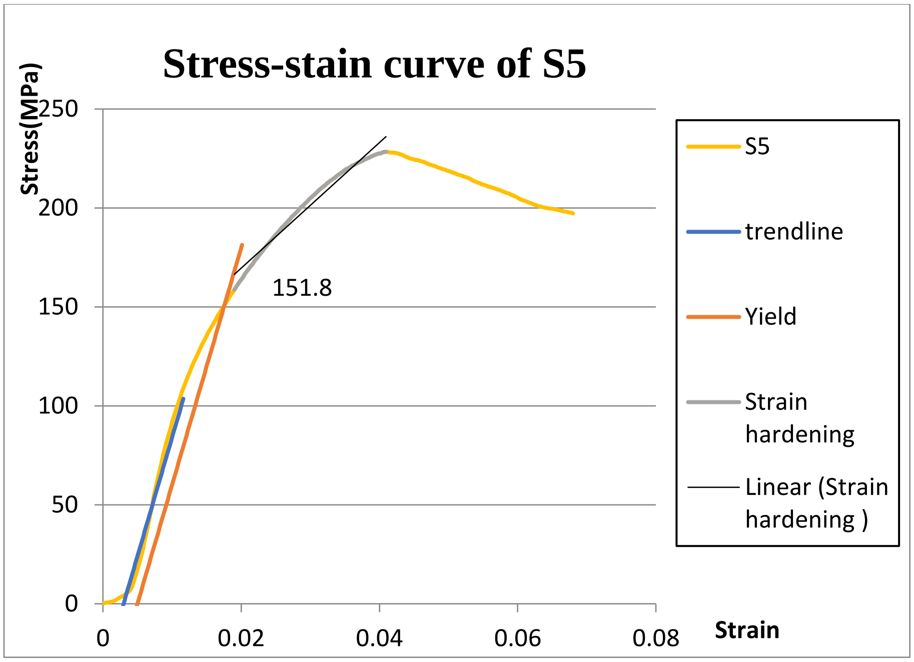

Figure A5: POR bending stress-strain of S5

Table A6: POR bending properties of S6

Sample Ref.	Thickness(mm)	Flexural modulus (GPa)	Flexural yield strength (MPa)	Strain Hardening Modulus (GPa)	Flexural Strength (MPa)
S6	6.22	61.2692	114.3	3.252	154.4

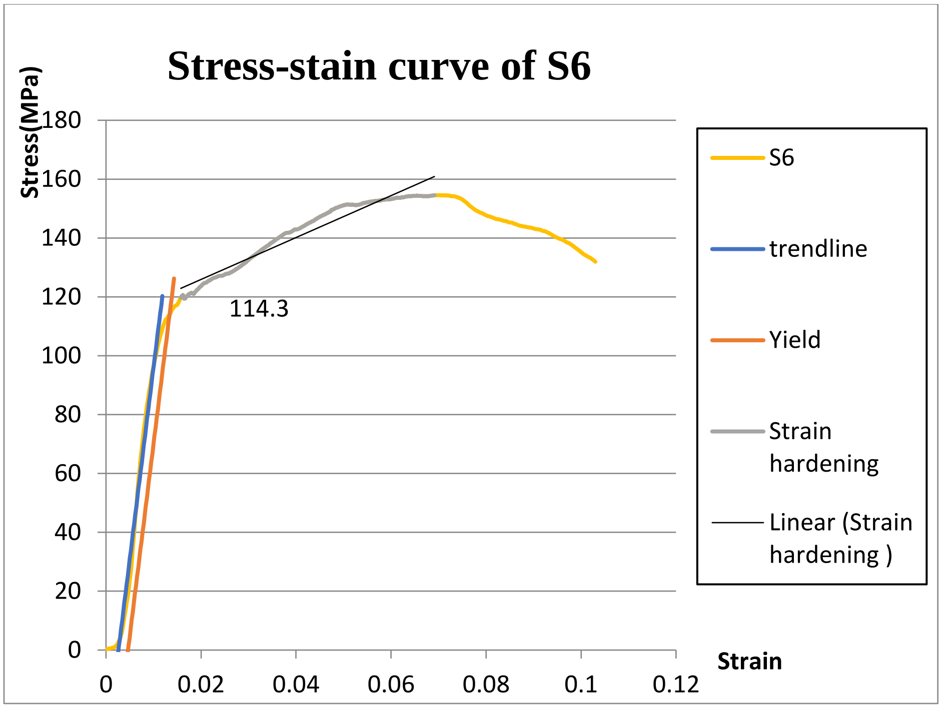

Figure A6: POR bending stress-strain of S6

Table A7: POR bending properties of S7

Sample Ref.	Thickness(mm)	Flexural modulus (GPa)	Flexural yield strength (MPa)	Strain Hardening Modulus (GPa)	Flexural Strength (MPa)
S7	7.04	60.9355	133.3	12.0903	219.7

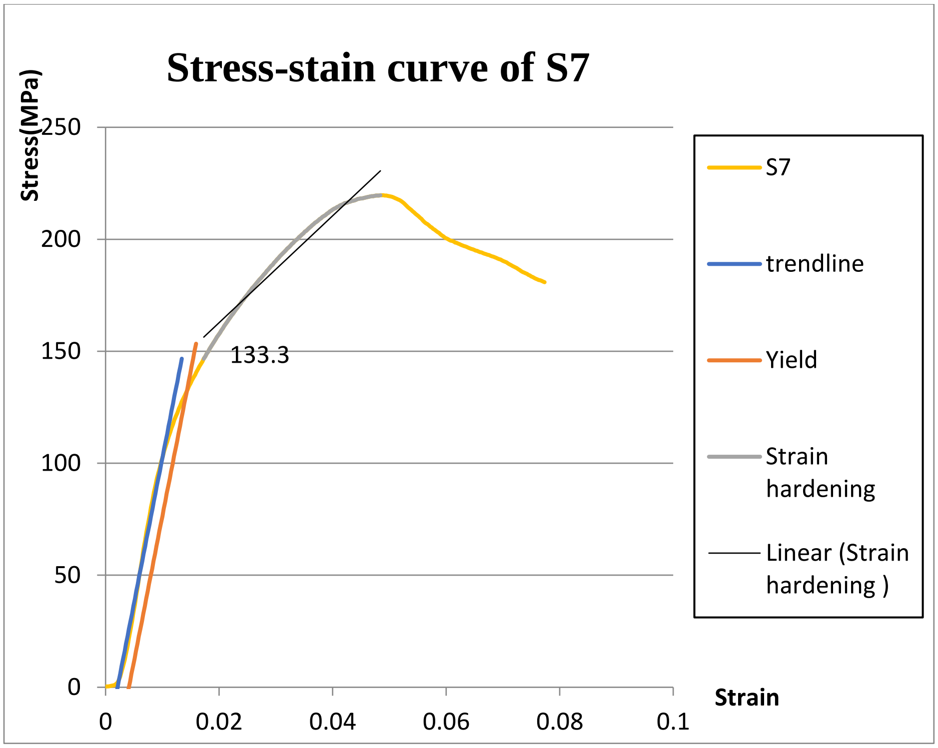

Figure A7: POR bending stress-strain of S7

Table A8: POR bending properties of S8

Sample Ref.	Thickness(mm)	Flexural modulus (GPa)	Flexural yield strength (MPa)	Strain Hardening Modulus (GPa)	Flexural Strength (MPa)
S8	7.3	50.0033	132.9	7.5430	169.8

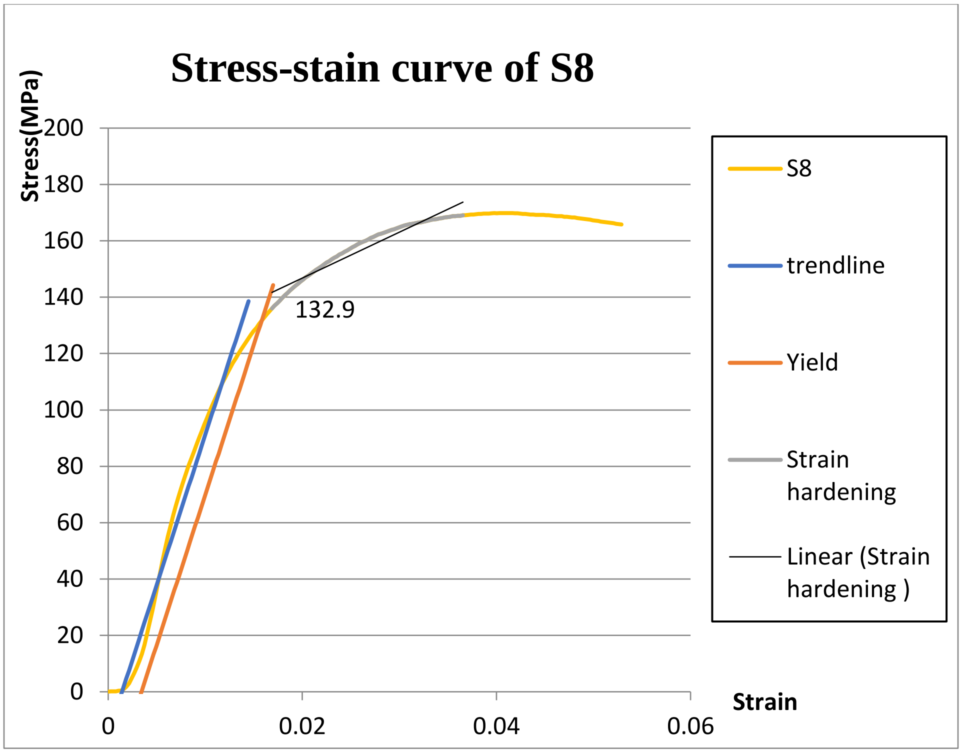

Figure A8: POR bending stress-strain of S8

Table A9: POR bending properties of S9

Sample Ref.	Thickness(mm)	Flexural modulus (GPa)	Flexural yield strength (MPa)	Strain Hardening Modulus (GPa)	Flexural Strength (MPa)
S9			failed		

Table A10: POR bending properties of S10

Sample Ref.	Thickness(mm)	Flexural modulus (GPa)	Flexural yield strength (MPa)	Strain Hardening Modulus (GPa)	Flexural Strength (MPa)
S10	4.0	70.8995	169.6	18.67545	492.1

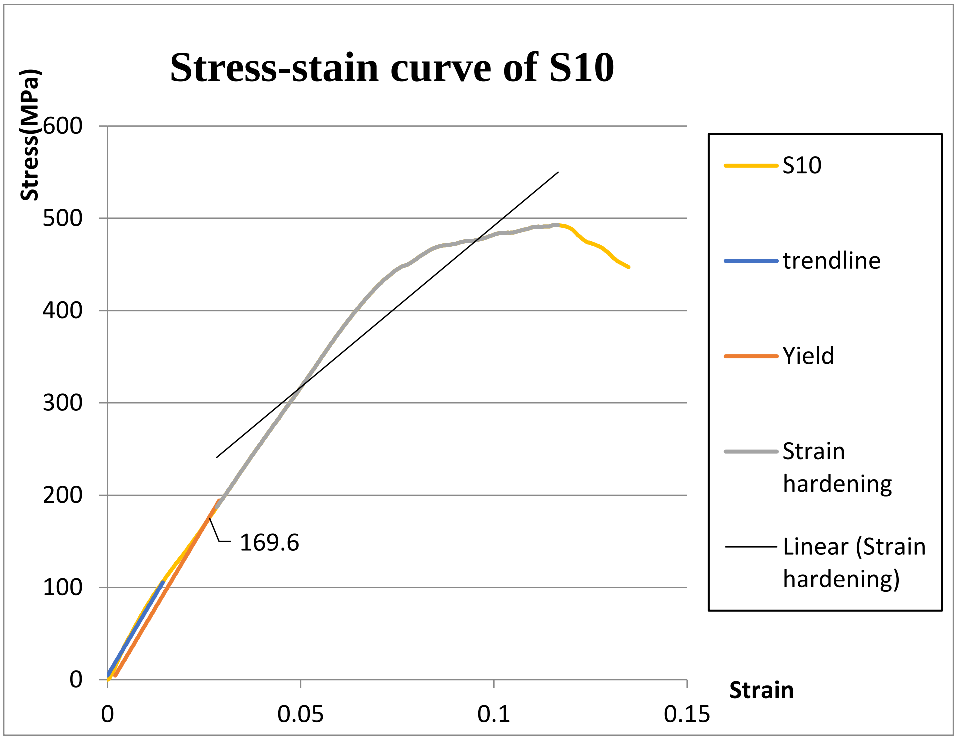

Figure A9: POR bending stress-strain of S10

Table A11: POR bending properties of S11

Sample Ref.	**Thickness(mm)**	**Flexural modulus (GPa)**	**Flexural yield strength (MPa)**	**Strain Hardening Modulus (GPa)**	**Flexural Strength (MPa)**
S11	4	77.0142	196.6055	47.7567	1022.6
	4.1	75.1906	159.3396	36.69572	582.4

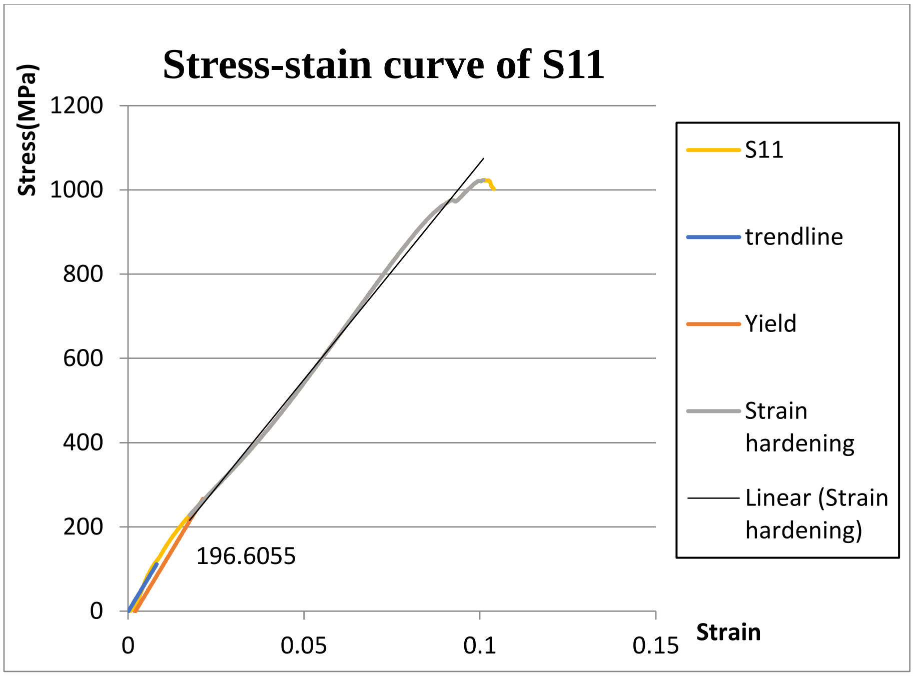

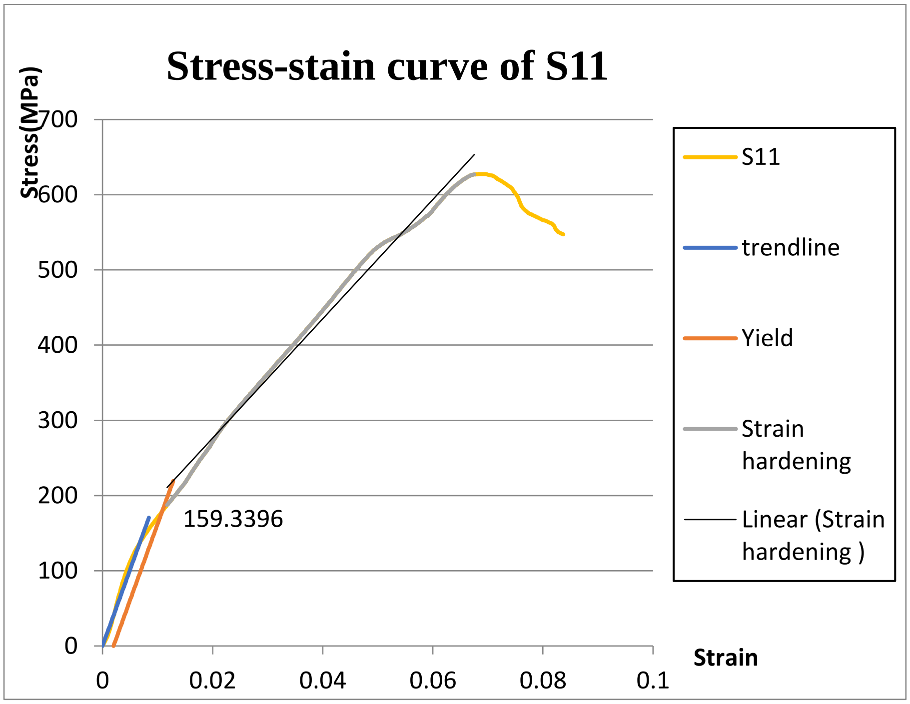

Figure A10: POR bending stress-strain of S11

Table A12: POR bending properties of S12

Sample Ref.	Thickness(mm)	Flexural modulus (GPa)	Flexural yield strength (MPa)	Strain Hardening Modulus (GPa)	Flexural Strength (MPa)
S12	3.8	72.4223	204.0	51.6518	621.9

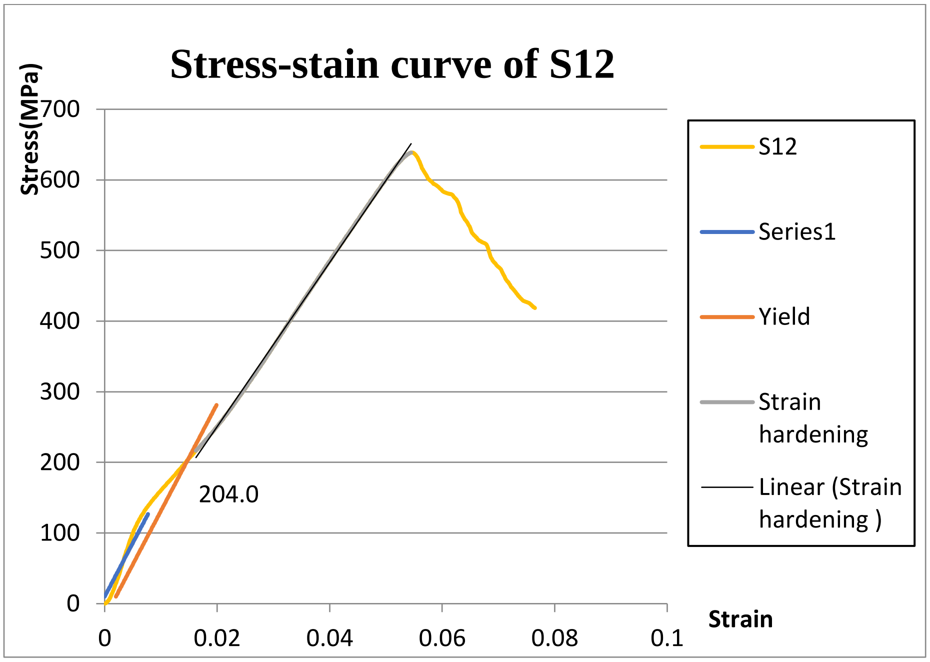

Figure A11: POR bending stress-strain of S12

Table A13: POR bending properties of S13

Sample Ref.	Thickness(mm)	Flexural modulus (GPa)	Flexural yield strength (MPa)	Strain Hardening Modulus (GPa)	Flexural Strength (MPa)
S13	3.80	68.009	87.60	19.64318	253.6

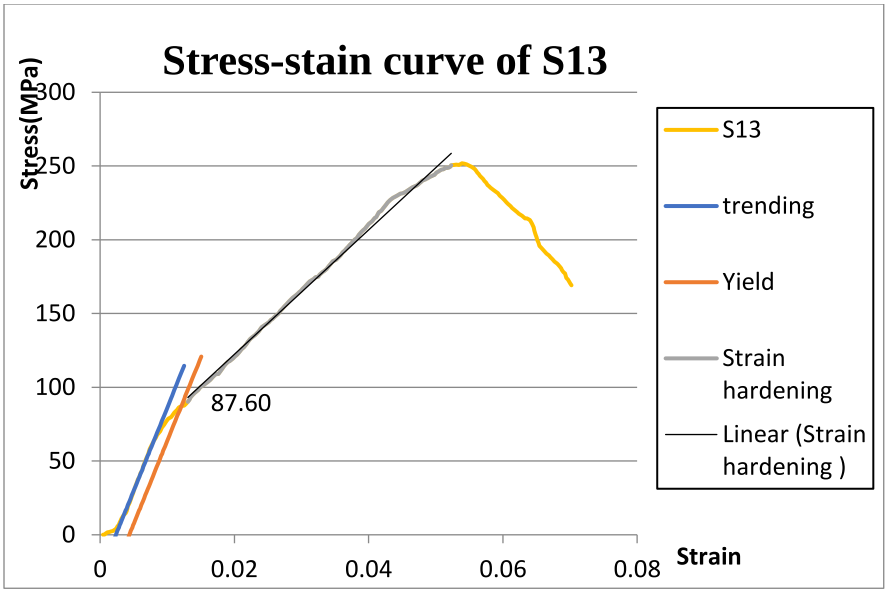

Figure A12: POR bending stress-strain of S13

Table A14: POR bending properties of S14

Sample Ref.	Thickness(mm)	Flexural modulus (GPa)	Flexural yield strength (MPa)	Strain Hardening Modulus (GPa)	Flexural Strength (MPa)
S14	4.20	69.09	125.9	24.28819	284.2

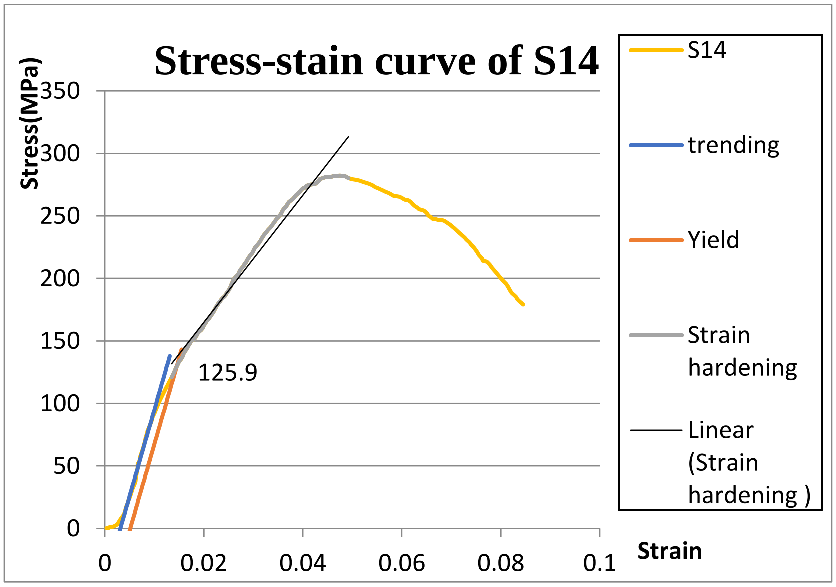

Figure A13: POR bending stress-strain of S14

Table A15: POR bending properties of S15

Sample Ref.	Thickness(mm)	Flexural modulus (GPa)	Flexural yield strength (MPa)	Strain Hardening Modulus (GPa)	Flexural Strength (MPa)
S15	4.28	78.537	166.8	13.44106	205.0

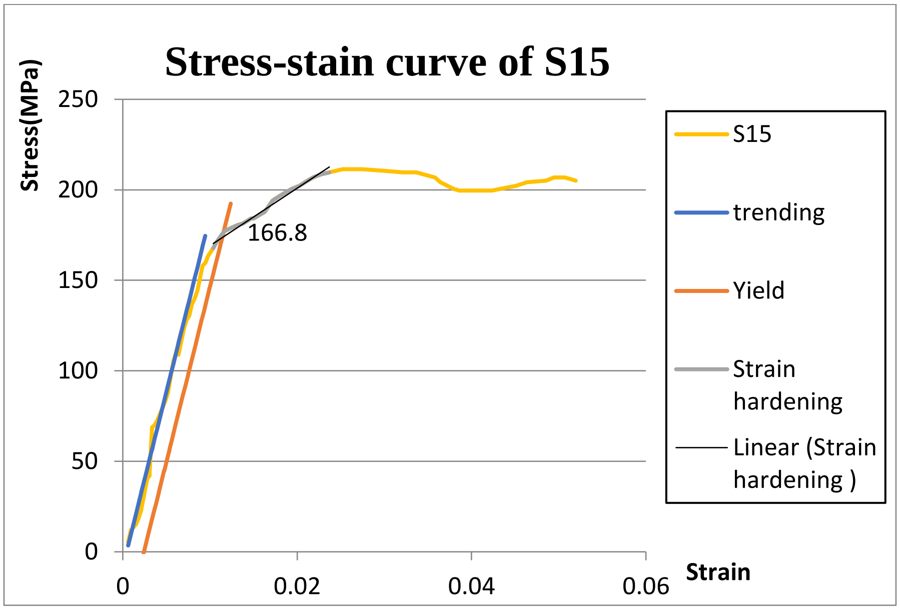

Figure A14: POR bending stress-strain of S15

Table A16: POR bending properties of A1,A2 and A3

Sample Ref.	Thickness(mm)	Flexural modulus (GPa)	Flexural yield strength (MPa)	Strain Hardening Modulus (GPa)	Flexural Strength (MPa)
A1	3.60	70.3449	91.1954	20.45299	264.78
A2	4.80	67.1912	130.9599	9.95648	311.64
A3	6.60	69.4707	99.86978	14.07885	284.3

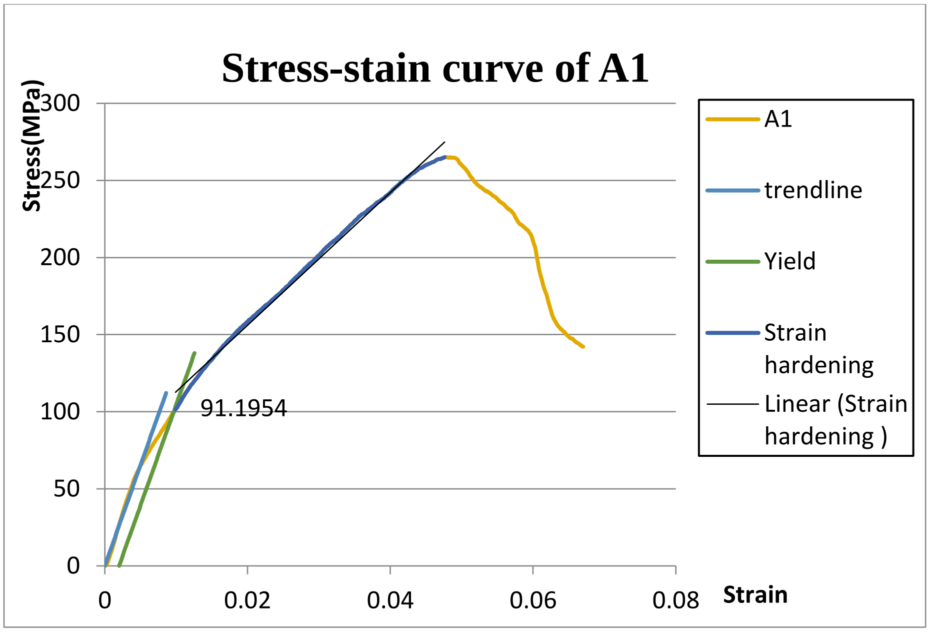

Figure A15: POR bending stress-strain of A1

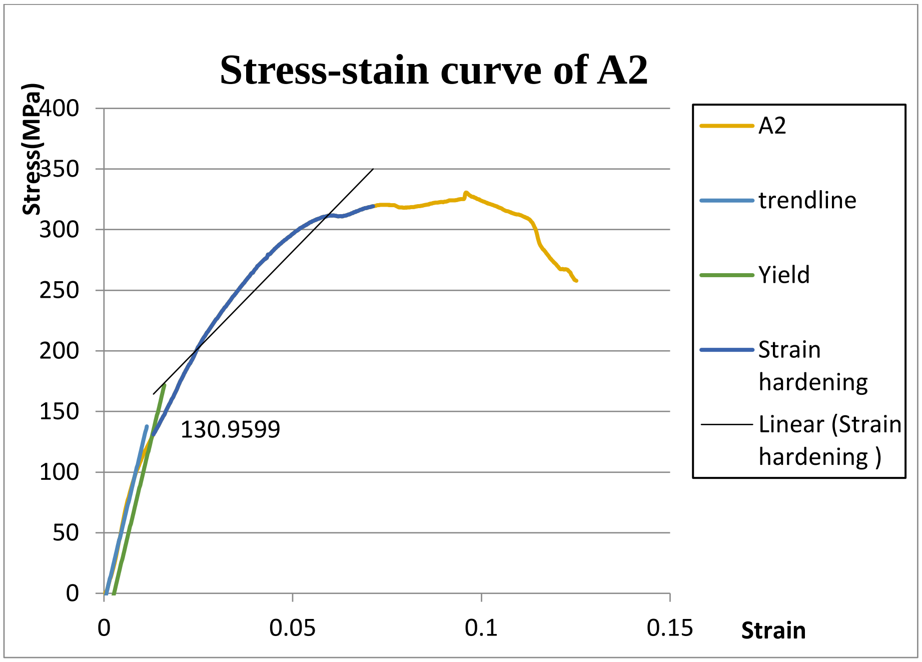

Figure A16: POR bending stress-strain of A2

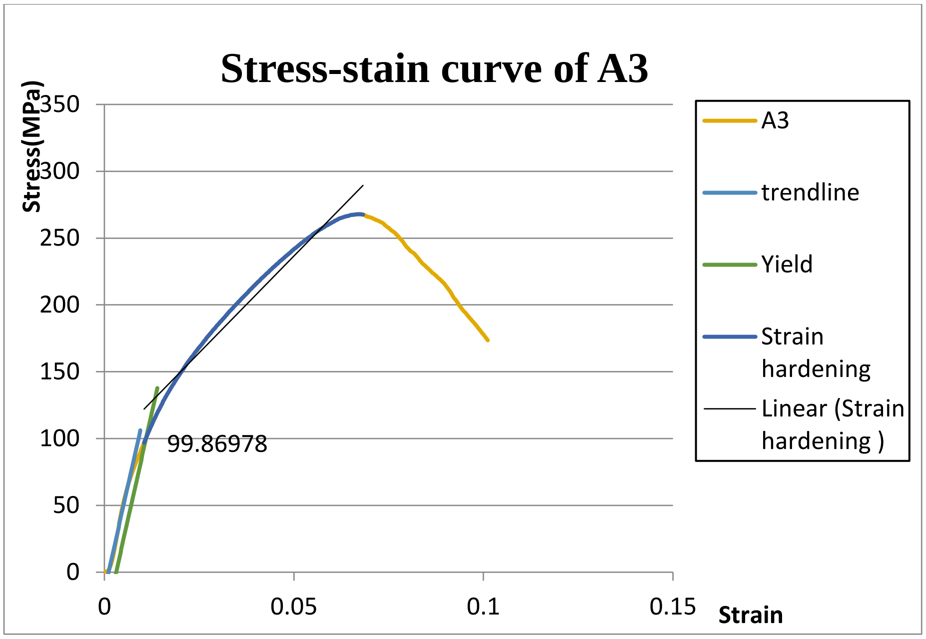

Figure A17: POR bending stress-strain of A3

Appendix II: POR Bending stress theoretical analysis

Matlab code:

```
%% input fiber volume fraction and loading
function [W] = POR (V_f,P)
E_m=69*10^9;
E_r=231*10^9;
E_rt=40*10^9;
v_m=0.33;
v_r=0.2;
G_r=20*10^9;
E_t=E_m*(1-V_f)+V_f*E_r;
E_p=E_m*(1-sqrt(V_f)+sqrt(V_f)/(1-(1-E_m/E_rt)*sqrt(V_f)));
v_tp=v_m*(1-V_f)+V_f*v_r;
v_pt=(E_p/E_t)*v_tp;
G_p=E_m /(2*(1+v_m));
G_t=G_p*(1-sqrt(V_f)+sqrt(V_f)/(1-(1-G_p/G_r)*sqrt(V_f)));
E_t=E_m*(1-V_f)+V_f*E_r;
C=[1/E_t,-v_pt/E_p,0;
   -v_tp/E_t,1/E_p,0;
   0,0,1/(G_t)];
D=inv(C);
%% effective modulus
for i=0:900
   a=i*pi/1800;
T1=[(cos(a))^2,(sin(a))^2,sin(2*a);
      (sin(a))^2,(cos(a))^2,-sin(2*a);
      -(1/2)*(sin(2*a)),(1/2)*(sin(2*a)),cos(2*a)];
T2=[(cos(a))^2 ,(sin(a))^2,-(1/2)*sin(2*a);
      (sin(a))^2 ,(cos(a))^2 ,(1/2)*sin(2*a);
```

```
        (sin(2*a)), -(sin(2*a)), cos(2*a)];
D_off=T1*D*T2;
G_11(1,1+i)=D_off(3,3);
C_off=inv(T2)*C*inv(T1);
v_12(1,1+i)=-C_off(1,2)/C_off(1,1);
v_21(1,1+i)=-C_off(1,2)/C_off(2,2);
E_C11(1,1+i)=1/C_off(1,1);
G_C11(1,1+i)=1/C_off(3,3);
E_11(1,1+i)=D_off(1,1)*(1-v_12(1,1+i)*v_21(1,1+i));
end
a_11=0:900;
D_inv22=E_11(end:-1:1);
E_c=E_11*0.5+D_inv22*(1-0.5);
E_eff=sum(E_c)/901;
v_eff=sum((v_12+v_21)/2)/901;
for i=1:5
    if i==1
        E_i(i)=E_m;
        v_i(i)=v_m;
    else if i==2
        E_i(i)=E_eff;
        v_i(i)=v_eff;
        else if i==3
        E_i(i)=E_m;
        v_i(i)=v_m;
        else if i==4
        E_i(i)=E_eff;
        v_i(i)=v_eff;
        else if i==5
        E_i(i)=E_m;
        v_i(i)=v_m;
            end
            end
            end
        end
    end
end
%% layer thickness
t_n=4*10^(-3);%total thickness
n=5;
t_cf=0.36*10^(-3);
t_al=((t_n-2*t_cf)/4);
for i=1:n
    if i==1
    t_i(i)=t_al;
    else if i==2
    t_i(i)=t_cf;
    else if i==3
    t_i(i)=t_al*2;
    else if i==4
    t_i(i)=t_cf;
    else if i==5
    t_i(i)=t_al;
        end
        end
        end
        end
    end
end
for i=1:n
h_i(1)=0;
h_i(i+1)=h_i(i)+t_i(i);
```

```
end
%%mean value
h_i1=h_i(1:n);
z_s=0.002;
D_s=sum((((E_i.*t_i)./(1-v_i.^2)).*((h_i1.^2)+h_i1.*t_i+(t_i.^2)/3-(h_i1+t_i/2).*z_s)));
v_s=(1/h_i(n+1))*sum(v_i.*t_i);
%% stress
a=0.0635/2;
c=0.0157/2;
R=0.0762/2;
M=(-P/(8*pi))*((1+v_s)*(1+2*log(a/c))+(1-v_s)*(1-((c^2)/(2*a^2)))*((a^2)/(R^2)));
syms z
stress=E_i.*(z-z_s).*M./((1-v_i)*(1+v_s)*D_s);
%% plot function
z0=0:1*10^(-5):t_n;
test1=(z0<h_i(2));
test2=(z0>=h_i(2)&z0<h_i(3));
test3=(z0>=h_i(3)&z0<h_i(4));
test4=(z0>h_i(4)&z0<=h_i(5));
test5=(z0>h_i(5)&z0<h_i(6));
f1(z)=stress(1);
f2(z)=stress(2);
f3(z)=stress(3);
f4(z)=stress(4);
f5(z)=stress(5);
y=@(z)(test1).*(f1(z))+(test2).*(f2(z))+(test3).*(f3(z))+(test4).*(f4(z))+(test5).*(f5(z));
plot(y(z0),z0)
W=y(z0);
C=double(W);
c=C';
E_com=D_s*12*(1-v_s^2)/(t_n^3)
end
```